



저작자표시-비영리-변경금지 2.0 대한민국

이용자는 아래의 조건을 따르는 경우에 한하여 자유롭게

- 이 저작물을 복제, 배포, 전송, 전시, 공연 및 방송할 수 있습니다.

다음과 같은 조건을 따라야 합니다:



저작자표시. 귀하는 원저작자를 표시하여야 합니다.



비영리. 귀하는 이 저작물을 영리 목적으로 이용할 수 없습니다.



변경금지. 귀하는 이 저작물을 개작, 변형 또는 가공할 수 없습니다.

- 귀하는, 이 저작물의 재이용이나 배포의 경우, 이 저작물에 적용된 이용허락조건을 명확하게 나타내어야 합니다.
- 저작권자로부터 별도의 허가를 받으면 이러한 조건들은 적용되지 않습니다.

저작권법에 따른 이용자의 권리는 위의 내용에 의하여 영향을 받지 않습니다.

이것은 [이용허락규약\(Legal Code\)](#)을 이해하기 쉽게 요약한 것입니다.

[Disclaimer](#)

**Master's Thesis of Engineering**

**Factors Influencing Seismic  
Demands of Secondary Systems in  
Nuclear Power Plants: A Case Study**

원자력 발전소 내 부구조물 지진요구에  
영향을 끼치는 요소: 사례연구

**January 2022**

**Graduate School of Engineering  
Seoul National University  
Architecture and Architectural Engineering**

**Yousang Lee**



# **Factors Influencing Seismic Demands of Secondary Systems in Nuclear Power Plants: A Case Study**

**Advisor: Hong-Gun Park**

**Submitting a Master's thesis of  
Architecture and Architectural Engineering**

**January 2022**

**Graduate School of Engineering  
Seoul National University  
Architecture and Architectural Engineering**

**Yousang Lee**

**Confirming the Master's thesis written by  
Yousang Lee**

**February 2022**

**Chair                    Sung-Gul Hong                    (Seal)**

**Vice-Chair           Hong-Gun Park                    (Seal)**

**Examiner              Cheol-Ho Lee                    (Seal)**



**Abstract**

**Factors Influencing Seismic  
Demands of Secondary Systems in  
Nuclear Power Plants: A Case Study**

Lee, Yousang

Department of Architecture and Architectural Engineering

College of Engineering

Seoul National University

After the Fukushima nuclear power plant accident in 2011, the U.S. Nuclear Regulatory Commission requested a nationwide re-evaluation of operating nuclear power plants. In Korea, the necessity of evaluating the safety of nuclear power plants has drawn attention due to the recent Gyeongju and Pohang earthquakes, the two largest earthquake events observed up to date.

In nuclear power plants, not only structures but also equipment and systems are subject to safety evaluation, as their importance is no less than structures. Unlike ordinary buildings, nuclear power plants can cause problems in sound operation due to malfunction of equipment, even if there is no damage to the structure. Therefore, in this paper, the seismic demand of the equipment, which is the secondary systems installed in the nuclear power plant, was determined

## Abstract

---

as the research scope.

Accurate estimation of seismic demand is required for seismic fragility analysis, which is part of seismic risk assessment. Current practice uses floor response spectrum method to estimate seismic demand, where conservatism or unconservatism is included. Therefore, this study examined the effects of the following four factors on the floor response spectrum through finite element analysis of the operating nuclear power plant structure: 1) dynamic coupling effect; 2) strong motion duration; 3) spatial variation; 4) treatment of uncertainty.

The dynamic coupling effect reduced the response, near the frequency of the structure, of the secondary system as its mass increased. The strong motion duration was correlated with the amplification of the secondary system response during resonance. On the other hand, even within the same floor, the deviation of the floor response spectra occurred greatly depending on the location. In particular, the magnitude of variance was notable for the vertical response, which was maintained even when the floor was divided into quadrants. Finally, considering uncertainty and randomness in numbers of variables, the floor response spectrum confirmed the reduction in amplitude, especially when probabilistic seismic response analysis was conducted.

Seismic fragility analysis of equipment was performed as an example, based on the calculated floor response spectrum. Probabilistic seismic response analysis along with the Latin hypercube simulation technique was introduced. In order to verify the effect of the seismic demand of the equipment on the fragility curve. The effect of the spatial variation factor was examined. As a

result of the analysis, it was confirmed that not only the median capacity but also the difference in variability showed a significant deviation in the HCLPF capacity. Accordingly, it was suggested that it was necessary to calculate the location-specific floor response spectrum to evaluate the realistic median capacity.

Keywords : Seismic fragility analysis, Floor response spectrum, Finite element analysis, Nuclear power plants

Student Number : 2020-28248

## Contents

<b>Abstract</b> .....	<b>i</b>
<b>Contents</b> .....	<b>iv</b>
<b>List of Acronyms</b> .....	<b>vii</b>
<b>List of Tables</b> .....	<b>viii</b>
<b>List of Figures</b> .....	<b>ix</b>
<b>Chapter 1. Introduction</b> .....	<b>1</b>
1.1 Background.....	1
1.2 Scope and Objectives.....	5
1.3 Outline of the Master’s Thesis.....	6
<b>Chapter 2. Literature Review</b> .....	<b>7</b>
2.1 Dynamic coupling effect .....	8
2.2 Influence of strong-motion duration.....	20
2.3 Spatial Variation .....	22
2.4 Treatment of uncertainty.....	29
<b>Chapter 3. Preliminary Study with Simplified Model....</b>	<b>33</b>
3.1 Introduction .....	33
3.2 Dynamic coupling effect .....	36
3.3 Influence of strong-motion duration.....	39
3.3.1 Ground motion selections.....	39

3.3.2 Duration dependency .....	41
3.4 Treatment of uncertainty .....	47
3.4.1 Input ground motions .....	47
3.4.2 Site response analysis .....	49
3.4.3 Deterministic seismic response analysis.....	51
3.4.4 Probabilistic seismic response analysis .....	56
3.4.5 Comparison.....	60
3.5 Summary.....	63

**Chapter 4. Numerical Analysis of Nuclear Power Plant Structures ..... 64**

4.1 Introduction .....	64
4.2 Modeling of the auxiliary building.....	65
4.2.1 General .....	66
4.2.2 Mesh size for finite element model .....	69
4.2.3 Other Assumptions .....	73
4.3 Dynamic coupling effect .....	74
4.4 Influence of strong-motion duration.....	83
4.5 Spatial variation.....	91
4.6 Treatment of uncertainty.....	104
4.7 Summary.....	111

**Chapter 5. Seismic Fragility Analysis of Equipment.....113**

5.1 Introduction .....	113
5.2 Seismic fragility analysis.....	114
5.3 Equipment seismic response analysis.....	118
5.4 Equipment seismic fragility curve.....	124
5.5 Summary.....	130

<b>Chapter 6. Conclusions .....</b>	<b>131</b>
<b>References .....</b>	<b>133</b>
<b>Appendix A: Spectrally Equivalent Earthquake Triads.....</b>	<b>142</b>
<b>초 록 .....</b>	<b>147</b>

## List of Acronyms

AB	auxiliary building
COV	coefficient of variance
EDG	emergency diesel generator
EPRI	Electric Power Research Institute
ESI	equipment-structure interaction
FIRS	foundation input response spectrum
FRS	floor response spectrum
HCLPF	high-confidence of low-probability of failure
KEPCO	Korea Electric Power Corporation
KHNP	Korea Hydro & Nuclear Power
LHS	Latin hypercube simulation
LMSM	lumped-mass stick model
MCS	Monte Carlo simulation
MDOF	multi-degree-of-freedom
NEP	non-exceedance probability
NPP	nuclear power plant
NRC	U.S. Nuclear Regulatory Commission
OBE	operating-basis earthquake
PGA	peak ground acceleration
RCB	reactor containment building
SDOF	single-degree-of-freedom
SPRA	Seismic Probabilistic Risk Assessment
SRP	Standard Review Plan
SRSS	square root of the sum of the squares
SSC	structure, system, and component
SSE	safe-shutdown earthquake

## List of Tables

Table 3-1 Factors covered in Chapter 3 .....	33
Table 3-2 Dynamic Properties of the Model .....	37
Table 3-3 Peak amplitude reduction due to dynamic coupling effect ..	38
Table 3-4 List of earthquake records .....	48
Table 3-5 Deterministic case designations .....	51
Table 3-6 Properties of the simplified model .....	52
Table 3-7 Thirty $f_s, \delta_s, \delta_e$ by Latin hypercube simulation.....	58
Table 4-1 Properties of the numerical modeling .....	66
Table 4-2 Summary of models with different mesh sizes.....	69
Table 4-3 Amplification decrease estimation for Gyeongju earthquake.....	88
Table 4-4 Amplification ratio and decrement estimation .....	89
Table 4-5 Statistics of spectral accelerations for two cases: total floor and four quadrants .....	103
Table 5-1 Summary of the variables considered in the thesis .....	121
Table 5-2 Summary of capacities and variability .....	129

## List of Figures

Figure 1-1 Damage of secondary systems (Fujita et al., 2012) .....	1
Figure 1-2 Outline of the master's thesis .....	6
Figure 2-1 FRS generation procedure .....	8
Figure 2-2 Decoupling criteria for secondary systems with single-point attachment to a primary system (ASCE/SEI 4-16, 2017).....	10
Figure 2-3 Acceleration response quantities for three different mass ratio cases (Der Kiureghian et al., 1983) .....	13
Figure 2-4 Floor response spectra: (a) for different mass ratios; (b) compared with time history analyses (Suarez and Singh, 1987).....	16
Figure 2-5 SDOF model: (a) without ESI (b) substructured model with ESI (Ostadan F., 2017) .....	17
Figure 2-6 Dynamic amplification ratios estimation (Kaneko, 2019)..	21
Figure 2-7 Auxiliary Control Building Models: (a) LMSM; (b) FEM (Damolini, El-Bahey, and Oikonomou, 2019).....	24
Figure 2-8 Contour plot of peak spectral accelerations (Damolini, El-Bahey, and Oikonomou, 2019).....	25
Figure 2-9 Sensor Location (TEPCO, 2011) .....	26
Figure 2-10 Spatial Variation of FRS (Ha, Kim, and Kim, 2021).....	26
Figure 2-11 Sensor location and tri-directional FRS (Jung et al., 2021).....	28
Figure 2-12 Comparison of Deterministic and Probabilistic FRS (Eggers, Bolourchi, and Ostadan, 2011) .....	30
Figure 2-13 Comparison of Deterministic and Probabilistic FRS (Zinn et al., 2015).....	31
Figure 2-14 Comparison of Deterministic and Probabilistic FRS (Cappa, Appelbaum, and Grant, 2019) .....	32
Figure 3-1 Simplified SDOF-SDOF Shear Building Model .....	34
Figure 3-2 El centro (1940) acceleration time history.....	37

## List of Figures

---

Figure 3-3 Uncoupled and coupled FRSs.....	38
Figure 3-4 5 % response spectra of spectrally equivalent ground motions .....	40
Figure 3-5 An example of spectrally equivalent records: (a) FRS; (b) amplification spectra; (c),(d),(e) time histories .....	41
Figure 3-6 Mean amplification spectra.....	43
Figure 3-7 Amplification vs. $D_{5-75}/T$ plots at the tuning frequency .....	44
Figure 3-8 Amplification ratio vs. $D_{5-75}$ ratio plot at the tuning frequency .....	45
Figure 3-9 Input response spectra (H1 direction): (a) NUREG/CR-0098 compatible inputs; (b) FIRS post site response analysis .....	50
Figure 3-10 FRS from deterministic seismic response analyses - (a) structure stiffness, (b) structure damping, (c) equipment damping, (d) three parameters considered .....	53
Figure 3-11 Logarithmic standard deviations from deterministic seismic response analyses.....	54
Figure 3-12 Thirty scale factors for equipment frequency sampled from LHS.....	57
Figure 3-13 FRSs from probabilistic seismic response analysis .....	59
Figure 3-14 Seismic response analyses comparison - (a) Median FRSs; (b) 84% NEP FRSs; (c) Logarithmic standard deviations.....	62
Figure 4-1 Operating nuclear power plant: (a) aeroview; (b) arrangement (source: KEPCO E&C co.).....	65
Figure 4-2 Models with different mesh sizes: (a) 3 m; (b) 2.5 m; (c) 2 m; (d) 1.5 m; (e) 1 m.....	70
Figure 4-3 Cumulative mass ratios comparison between different mesh sizes: (a) X (EW) direction; (b) Y (NS) direction; (c) Z (Vertical) direction .....	72
Figure 4-4 Process of frequency domain analysis .....	74
Figure 4-5 Node locations and IDs at EL. 137.5 ft floor.....	75
Figure 4-6 Impedance functions of Node 9168: X dir. (top); Y dir. (middle); Z dir. (bottom).....	77

Figure 4-7 Comparison of FRS at Node 9168 for different mass ratios: X dir. (top); Y dir. (middle); Z dir. (bottom).....	80
Figure 4-8 Peak reduction vs. mass ratio.....	81
Figure 4-9 Node locations and IDs: (a) seven nodes at 156 ft floor; (b) four additional nodes at different elevations .....	84
Figure 4-10 Mean amplification spectra at eleven nodes .....	85
Figure 4-11 Amplification vs. $D_{5-75}/T$ plots at eleven nodes .....	86
Figure 4-12 Amplification ratio vs. $D_{5-75}$ ratio plot for eleven node ....	90
Figure 4-13 EL. 137.5 ft floor plan and nodes .....	92
Figure 4-14 FRS of EL. 137.5 ft floor: (a) X direction; (b) Y direction; (c) Z direction .....	93
Figure 4-15 Spatial distributions of spectral accelerations: (a) X direction; (b) Y direction; (c) Z direction .....	96
Figure 4-16 Vertical spectral acceleration distributions at: (a) 10.14 Hz; (b) 14.75 Hz.....	97
Figure 4-17 Auxiliary building separation: (a) Quadrants; (b) Corresponding LMSMs (KEPCO E&C, 2020, 2010).....	98
Figure 4-18 X direction FRS at four quadrants .....	99
Figure 4-19 Y direction FRS at four quadrants .....	100
Figure 4-20 Z direction FRS at four quadrants .....	100
Figure 4-21 Input response spectra: (a) Horizontal 1; (b) Horizontal 2; (c) Vertical.....	106
Figure 4-22 Node locations and IDs: (a) plan; (b) elevation.....	107
Figure 4-23 Median FRS of Node 10135(left), Node 22546(right) ...	108
Figure 4-24 Median FRS of Node 22526(left), Node 10137(right) ...	109
Figure 5-1 Fragility curves example (EPRI, 2018) .....	116
Figure 5-2 Node locations and IDs.....	118
Figure 5-3 Horizontal $S_a$ distributions .....	122
Figure 5-4 Mean fragility curves .....	127



## Chapter 1. Introduction

### 1.1 Background

#### *Secondary systems*

Secondary systems often referred to as non-structural elements are components in a building that are not load-resisting but subjected to seismic force. They include architectural components, equipment, and building contents (Villaverde, 1997). Despite their name, the importance of secondary systems is significant. The cost of mechanical and electrical systems may exceed that of the structure that holds them. More importantly secondary systems maintain the sound operation of the building.



Figure 1-1 Damage of secondary systems (Fujita et al., 2012)

Secondary systems, repeatedly reported, are vulnerable during earthquake events (Jiang, 2015). Shown in Figure 1-1 are examples of damage found in secondary systems during the 2011 Tohoku earthquake that occurred in Japan. Such failure not only cause prodigious economical losses but may also threaten public safety if it occurs in important facilities including hospitals, fire stations, nuclear power plants, and others.

Especially for nuclear power plants (NPP), the survivability of the equipment is crucial. Unlike ordinary buildings, equipment functionality failure is a governing failure mode in NPPs. Even though structural walls are intact, malfunction of electrical equipment could lead to radiation release or other catastrophic results. Therefore, seismic analysis of secondary systems should be thoroughly performed.

### *A necessity for seismic re-evaluation of operating nuclear power plants*

Due to the aforementioned importances of secondary systems, it has been researched as a part of NPPs safety issues for the past decades. Since the 1970's U.S. Nuclear Regulatory Commission (NRC) has been requesting a seismic re-evaluation of old nuclear power plants in the U.S. This trend further expanded nationwide and required rigorous criteria, as more seismological data was updated. Driven by Fukushima Daiichi nuclear disaster in 2011, NRC established Near-Term Task Force (NTTF) to request extensive re-evaluation for seismic hazards.

Along with these requests, related documents have been developed by

## Chapter 1 Introduction

---

national laboratories, and also a nonprofit organization Electric Power Research Institute (EPRI). Seismic design and analysis of NPP structures have advanced and methodologies for evaluating operating NPPs have been developed. One of two methods is Seismic Probabilistic Risk Assessment (SPRA) which is becoming common practice in the field and extensive researches are currently underway. Recent earthquake events in Pohang (2017) and Gyeongju (2016), South Korea, have fueled the need to implement SPRA in line with the trend.

Seismic Fragility Analysis is an integral part of SPRA, where seismic capacities of individual structures and equipment are estimated (Choi, 2017). The goal of seismic fragility analysis is to estimate the conditional probability of failure, which is by definition fragility, at a given magnitude of seismic motion parameter.

### Motivation

Before evaluating the equipment fragility, demand should be estimated. The current practice of estimating seismic demand may include both conservatism and unconservatism. Conservative demand consequently leads to lesser fragility and vice versa. However, when such conservatism, hopefully, is removed by more realistic approaches, larger fragility is expected to be achieved, promising greater seismic capacity. For this purpose, the following four candidates were selected to be investigated in this thesis:

[1] Dynamic coupling effect is known to reduce seismic demand of secondary systems when they are in resonance with primary structure and their

mass is high (Villaverde and Newmark, 1980; Der Kiureghian et al. 1983; Gupta and Jaw, 1986; Suarez and Singh, 1987). However, these studies were limited to simplified models.

[2] Standard Review Plan (SRP) 3.7.1, part of NUREG-0800 (2014), states that the design ground time history should satisfy the minimum acceptable strong motion duration,  $D_{5-75}$  of 6 s. The strong-motion duration is defined as the required time for the cumulative Arias intensity to rise from 5 percent to 75 percent. This could be a severe criterion for South Korea, where  $D_{5-75}$  of Gyeongju earthquake is only 1.3 s.

[3] Conventionally lumped-mass stick models (LMSM) were used for seismic analysis of NPP structures. LMSM is advantageous in that it reduces computational cost while reasonably representing the dynamic properties of the actual structure. However, as one master node represents the entire floor, its result is considered as a simplified representative. It is expected to show spatial variance within the same floor if analyzed with a finite element model(FEM). Hereinafter this factor will be referred to as spatial variation.

[4] Considering seismic fragility analysis, uncertainty and randomness should be accounted for in the seismic analysis. There are two approaches to presented in EPRI guidance (Grant, Hardy, and Short, 2018), namely deterministic seismic response analysis and probabilistic seismic response analysis. Structure responses of the two methods were compared by several authors, but they did not further propagate the difference to fragility curve (Zinn et al. 2015; Cappa et al. 2019). In the thesis, this factor will be referred to as the treatment of uncertainty.

### 1.2 Scope and Objectives

The objective of this study is to estimate the realistic seismic demand on the secondary system and investigate factors participating in it. The four factors aforementioned in the previous section are separately studied by a simple analytical model. The purpose of this step is to reproduce results reported in previous literature and to gauge the effect of the factors.

These findings are then applied to an NPP structure. It is best to conduct a shake-table test to assess the most accurate seismic response of the NPP structure. Considering the size of the structure, a more feasible numerical analysis with a finite element model is performed. In pursuit of precision, the most appropriate conditions are applied with the following assumptions. Since NPPs are designed to remain elastic during the seismic event, the nonlinearity of the building is intentionally neglected in the study. In addition, soil-structure interaction (SSI) is justifiably out of scope, which will be discussed later.

The important feature included in the thesis is the concept of variability. Typical structural analysis neglects uncertainty and randomness. In fragility analysis, uncertainty and randomness of every component are considered statistically or probabilistically, which is a more realistic representation. This procedure is thoroughly presented along with the background introduction.

### 1.3 Outline of the Master’s Thesis

The thesis is mainly comprised of three parts, literature review, numerical analyses, and application, respectively.

<b>Chapter 2. Literature review</b>	<b>Chapter 3. Preliminary study with simplified model</b>	<b>Chapter 4. Numerical analysis of nuclear power plant structures</b>	<b>Chapter 5. Seismic fragility analysis of equipment</b>
<ul style="list-style-type: none"> <li>• Dynamic coupling effect</li> <li>• Strong-motion duration</li> <li>• Spatial distribution</li> <li>• Treatment of uncertainty</li> </ul>	<ul style="list-style-type: none"> <li>• Simplified numerical model</li> <li>• Investigate influences of each factor</li> </ul>	<ul style="list-style-type: none"> <li>• Finite element analysis</li> <li>• Quantify conservatisms</li> </ul>	<ul style="list-style-type: none"> <li>• Introduce the process of seismic fragility analysis</li> <li>• Effect of spatial distribution on the fragility curve</li> </ul>

Figure 1-2 Outline of the master's thesis

Chapter 2 reviews code provisions regarding input for the secondary system. Literature reviews follow covering important factors not mentioned in the code or noteworthy to examine.

Those factors are explored, in Chapter 3, with a simplified two-degree-of-freedom model as a preliminary study. Reported effects of the factors are verified. In Chapter 4, findings in the previous chapter are applied to a finite element model of an operating nuclear power plant. As the model is three-dimensional, planar response variability is additionally considered.

In Chapter 5, seismic fragility analysis of equipment is presented as an example, to show its procedure and to stress the significance of the seismic demand on the fragility curve.

## Chapter 2. Literature Review

In this chapter, previous studies and code provisions related to the following four topics are presented:

- Dynamic Coupling Effect
- Influence of Strong-Motion Duration
- Spatial Variation
- Treatment of Uncertainty

## 2.1 Dynamic coupling effect

The dynamic coupling effect is neglected in the FRS method. The general procedure for generating FRS is graphically explained in Figure 2-1. First, dynamic analysis for separated primary structure is performed. Resultant response acceleration at the location where the secondary system is installed can be used as input for a series of single-degree-of-freedom (SDOF) oscillators which represent the secondary system of frequency unknown. The frequency of the massless oscillator is varied and its corresponding maximum response is recorded. Finally, FRS is generated where abscissa is frequency and ordinate is spectral response of oscillator. In short separate dynamic analyses are performed consecutively, the reason why this method is also called “system-in-cascade”.

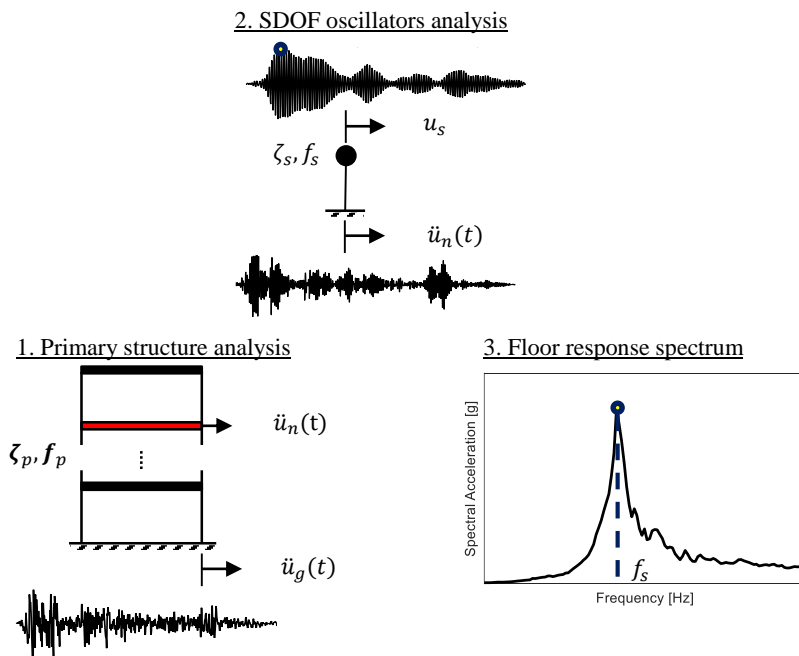


Figure 2-1 FRS generation procedure

## Chapter 2 Literature Review

---

However, the conventional FRS method is accurate when the secondary system is very light and its natural frequency is not close to that of the primary system. When it is not the case, conservative results were reported due to the so-called dynamic coupling effect. This, also known as, equipment-structure interaction (ESI) occurs as the secondary structure response alters the primary structure response. The modified response further shifts the secondary system response, back and forth.

### ASCE/SEI 4-16 (2017)

In ASCE/SEI 4-16 (2017) Chapter 3.7 dynamic coupling criteria are suggested. Figure 2-2 shows the criteria for a single-point attachment case. The threshold line is defined as frequency error between uncoupled model and coupled model of 10%. However, it is stated in commentary that response error could be greater always on the conservative side. This criteria constraints a very limited range requiring coupling, i.e. uncoupling allowed for most cases. This may lead to large conservatism, for instance, a mass ratio of 1% tuned case could reduce response quite amount yet coupling is not mandatory. The state-of-art techniques regarding the dynamic coupling effect follow.

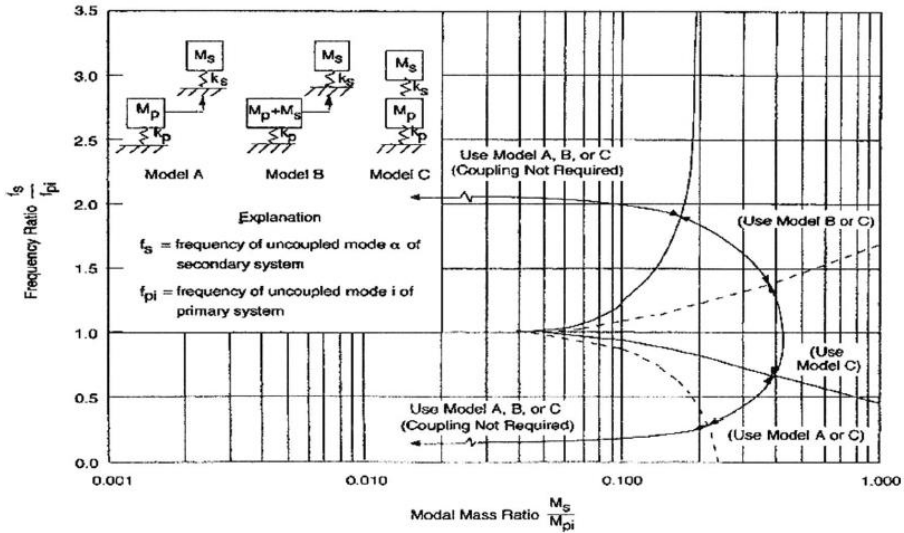


Figure 2-2 Decoupling criteria for secondary systems with single-point attachment to a primary system (ASCE/SEI 4-16, 2017)

Villaverde and Newmark (1980)

Pioneers have studied this phenomenon since the 1970s. One branch was to generate FRS with uncoupled modal properties of primary and secondary systems. Villaverde and Newmark (1980) proposed an approximate method to derive the maximum response of secondary systems attached to buildings. The modal analysis result of the building is modified to incorporate the mode of secondary systems then the modal superposition method proceeds.

Der Kiureghian et al. (1983)

Der Kiureghian et al. (1983) introduced a perturbation method to include secondary system mode. The perturbation method, in short, assumes small variations in the eigenvalues and eigenvectors of the primary structure after

## Chapter 2 Literature Review

---

coupling. Instead of the time history method, random vibration theory was used to determine the peak response of the secondary system. This method, therefore, is inherently limited to the stochastic input.

Sackman et al. (1983)

A companion paper by Sackman et al. (1983) similarly derived the modal properties via perturbation methods and proposed closed-form expressions for the natural frequencies. The resultant properties can be used in the time-domain analysis, where any excitation is acceptable.

The authors approximated the modal properties of the combined system, which is composed of an n-degree-of-freedom structure and SDOF equipment attached at the kth degree of freedom of the structure.

$$\omega_i^* = \left\{ \frac{1 + \frac{\beta_i + \gamma_i}{2} \pm \left[ \left( 1 + \frac{\beta_i + \gamma_i}{2} \right)^2 - (1 + \beta_i) \right]^{\frac{1}{2}}}{1 + \beta_i} \right\}^{\frac{1}{2}} \omega_i, \quad (2.1)$$

$\beta_i \geq 0$

$$\zeta_i^* = \frac{\sqrt{1 + \beta_i} \zeta_i + (1 - \alpha_i)^2 \gamma_i \zeta_e}{\sqrt{1 + \beta_i} (1 + \alpha_i^2 \gamma_i)} \frac{\omega_i}{\omega_i^*} \quad (2.2)$$

The superscript asterisk is used to distinguish the properties of the combined system. The ith mode modal frequency,  $\omega_i^*$  and damping coefficient,  $\zeta_i^*$  are defined in terms of the uncoupled structure and equipment properties. Then the influences of resonance and mass are reasonably accounted for with the quantities namely, the modal amplification factor,  $\alpha_i$ , the detuning parameter,

$\beta_i$  and the effective mass ratio,  $\gamma_i$ .

$$\alpha_i = - \frac{1}{\frac{\beta_i + \gamma_i}{2} \pm \left[ \left( 1 + \frac{\beta_i + \gamma_i}{2} \right)^2 - (1 + \beta_i) \right]^{\frac{1}{2}}}, \quad (2.3)$$

$$\beta_i \geq 0$$

$$\beta_i = \frac{\omega_1^2 - \omega_e^2}{\omega_e^2} \quad (2.4)$$

$$\gamma_i = \frac{m_e}{M_i / \phi_{ki}^2} \quad (2.5)$$

With a similar approach, the modal properties of a new mode due to the additional degree of freedom are defined. The following process of estimating the response of the secondary system is omitted in the thesis, for more details refer to the literature. The authors illustrate the influence of the dynamic interaction with a numerical example as shown in Figure 2-3.

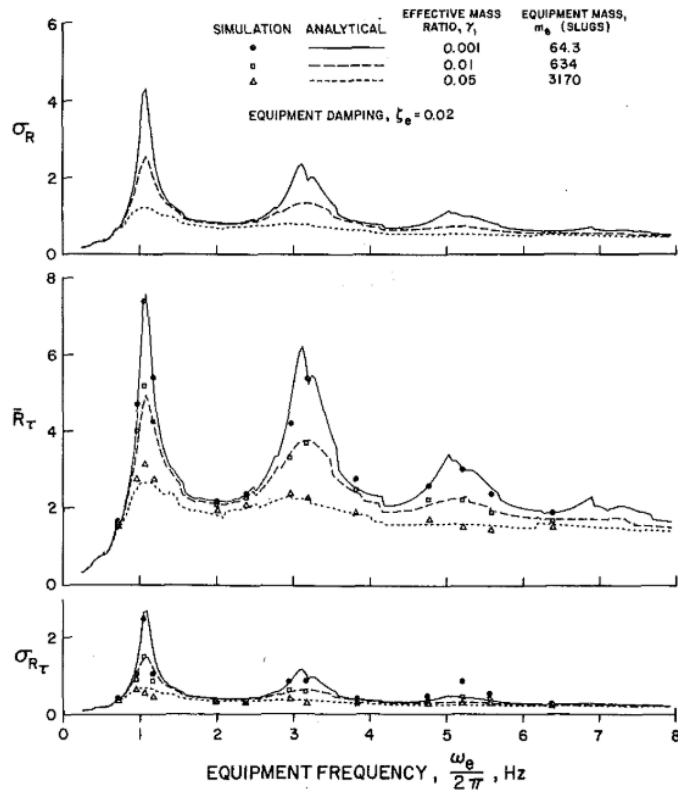


Figure 2-3 Acceleration response quantities for three different mass ratio cases  
(Der Kiureghian et al., 1983)

Gupta (1984)

Gupta (1984) further developed the perturbation technique to account for multi-degree-of-freedom (MDOF) primary and secondary systems cases. Instead of the stochastic approach, the author adopted the direct generation method, which utilizes the response spectrum of the primary structure. The resultant FRS exhibited better agreement with the time-history analysis for the entire frequency range than that of Der Kiureghian et al. (1983).

Igusa and Der Kiureghian (1985a, 1985b, 1985c)

Igusa and Der Kiureghian (1985a) based on Der Kiureghian et al. (1983), derived the modal properties of the coupled system that include not only tuning and mass effect but also nonclassical damping. After a preliminary study with the special case of a 2-DOF coupled system, Igusa and Der Kiureghian (1985b) extended to more generalized multiply supported, MDOF secondary systems. Finally, Igusa and Der Kiureghian (1985c) suggested the FRS generation method with the previously approximated modal properties. The authors applied the proposed method to a numerical sample that resembles a typical nuclear power plant LMSM. Again it was compared to the results of the direct integration method via the Newmark method. Excellently capturing all dynamic interaction effects, the results were within 90% confidence intervals of the time history solutions.

### Gupta and Jaw (1986a, 1986b)

Gupta and Jaw (1986a, 1986b) extended to a nonclassically damped coupled system. In many real cases, the primary and the secondary systems differ in damping characteristics. As the nonclassical damping matrix is insoluble with modal analysis, the authors calculated complex eigenvalues via state-space formulation. 9 coupled systems subjected to 12 ground motions were then analyzed with the response spectrum method, showing less than 1% error compared to the time history analyses.

### Suarez and Singh (1987)

Suarez and Singh (1987) developed a mode synthesis method to obtain the modal properties including ESI. Instead of formulating coupled modal properties based on those of the uncoupled components, the authors first

derived transformed matrices of the coupled system as in equation (2.6).

$$\mathbf{M}^* \ddot{\mathbf{q}} + \mathbf{C}^* \dot{\mathbf{q}} + \mathbf{K}^* \mathbf{q} = -\boldsymbol{\gamma}^* \ddot{x}_g(t) \quad (2.6)$$

where

$$\mathbf{M}^* = \mathbf{I} \quad (2.7)$$

$$\mathbf{C}^* = \begin{bmatrix} 2\beta_p \omega_p & \cdots & 0 \\ \vdots & \ddots & \vdots \\ 0 & \cdots & 0 \end{bmatrix} + \mathbf{U}^T \mathbf{C}_c \mathbf{U} \quad (2.8)$$

$$\mathbf{K}^* = \begin{bmatrix} \omega_p^2 & \cdots & 0 \\ \vdots & \ddots & \vdots \\ 0 & \cdots & 0 \end{bmatrix} + \mathbf{U}^T \mathbf{K}_c \mathbf{U} \quad (2.9)$$

$$\mathbf{U} = \begin{bmatrix} \boldsymbol{\Phi}'_p & \mathbf{0} \\ \mathbf{0} & \boldsymbol{\phi}'_e \end{bmatrix} \quad (2.10)$$

$\mathbf{M}^*$ ,  $\mathbf{C}^*$ ,  $\mathbf{K}^*$ ,  $\mathbf{q}$  are the transformed mass, damping, stiffness matrices, and displacement vector.  $\mathbf{C}_c$ ,  $\mathbf{K}_c$  are the coupling matrices and  $\boldsymbol{\Phi}'_p$ ,  $\boldsymbol{\phi}'_e$  are eigenvectors of the primary and secondary system, respectively.

The limitation of the perturbation approach, the assumption of very light equipment, was overcome. Second modal analysis, though, is required to obtain the modal properties of the coupled system. The authors ease this computational cost by reducing the number of modes. Yet by relating the neglected modes and the kept modes, accuracy was ensured. Shown in Figure 2-4 are FRS of numerical examples that cover heavy equipment and comparison with time history analyses which is in good agreement.

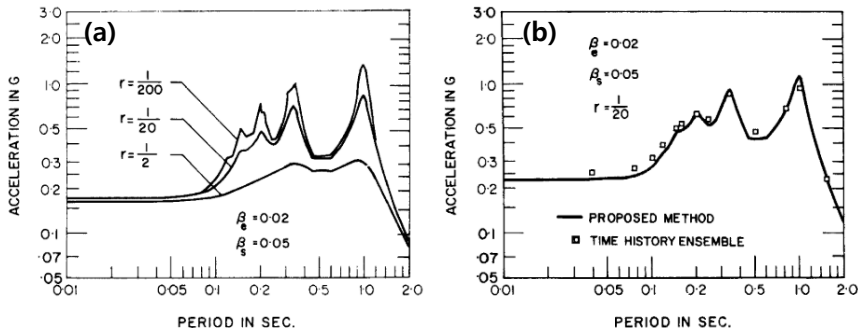


Figure 2-4 Floor response spectra: (a) for different mass ratios; (b) compared with time history analyses (Suarez and Singh, 1987)

Tseng (1989)

Previously discussed methods are all time-domain analysis. Tseng (1989), contrarily suggested a substructuring method in the frequency domain. This method is analogous to a process used in SSI analysis, which accounts for the ESI by incorporating equipment support impedance functions. Figure 2-5 shows the concept of this method. (a) is a conventional approach assuming structure floor as fixed-base, consequently, ESI is neglected and dynamic properties of equipment system are solely considered. (b), on the other hand, includes the support impedance connected to the equipment properties in series.

The impedance function, or interchangeably dynamic stiffness or compliance, at the support is obtainable by applying unit harmonic force. It is also often referred to as transfer function, in this specific case force input is transferred to displacement output. The impedance function can be expressed as below,

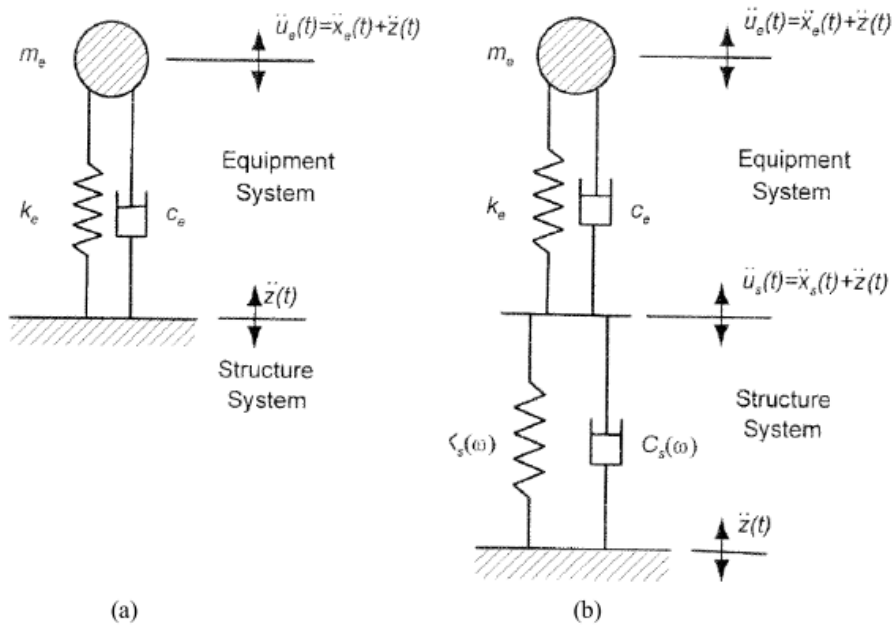


Figure 2-5 SDOF model: (a) without ESI (b) substructured model with ESI

(Ostadan F., 2017)

$$D_s(\omega) = K_s(\omega) + i\omega C_s(\omega) \quad (2.11)$$

where  $K_s(\omega)$  is the stiffness term and  $C_s(\omega)$  is the damping term as shown in Figure 2-5 (b). In the frequency domain, the equation of motion for this system consisting of a series of springs and viscous dampers can be expressed as,

$$\left\{ -\omega^2 m_e + \frac{i\omega c_e + k_e}{1 + \alpha_e} \right\} \ddot{X}_e(\omega) = -m_e \ddot{Z}(\omega) \quad (2.12)$$

$$\alpha_e(\omega) = \frac{k_e + i\omega c_e}{D_s(\omega)} \quad (2.13)$$

$\alpha_e(\omega)$  is an equipment impedance to support impedance ratio. This term reflects the dynamic coupling effect.  $m_e$ ,  $k_e$ ,  $c_e$  are mass, stiffness, and damping coefficient of the equipment.  $\ddot{Z}(\omega)$  and  $\ddot{X}_e(\omega)$  are Fourier transforms of absolute floor acceleration and relative equipment acceleration time histories.

Rearranging (2.12) gives the absolute floor acceleration to the absolute equipment acceleration transfer function expressed as,

$$\tilde{H}_e(\omega) = \frac{1 + 2i\beta_e\Omega}{\{1 - (1 + \alpha_e)\Omega^2\} + 2i\beta_e\Omega} \quad (2.14)$$

where  $\Omega = \frac{\omega}{\omega_e}$  is frequency ratio and  $\beta_e$  is damping ratio of the equipment.  $\tilde{H}_e(\omega)$  is the typical transfer function expression except for the newly introduced term  $\alpha_e(\omega)$ .

This method effectively generates dynamic coupling considered FRS. However, it is important to note its drawback which is an assumption of SDOF equipment and SDOF slab. This means that only a single mode of each component is accounted for and higher modes are neglected for FRS generation. According to EPRI technical report (Ostadan, 2017) higher modes contribute to the increased equipment response, about ten percent at maximum. Hence it may be necessary to increase FRS by ten percent if this method is used.

### Xu et al. (2004)

Xu et al. (2004) performed benchmark evaluation of state-of-the-art seismic analysis methods for four coupled system cases representing NPP structures: 1) singly-supported; 2), 3), 4) multiply-supported. Total 10 load cases were considered varying three parameters: secondary-to-primary system frequency ratio, mass ratio, and modal damping ratios. Four methods by Chen, Gupta, Igusa and Der Kiureghian, and Stevenson and Associates were compared to the direct integration method, all yielding sufficiently small errors. The authors concluded that the goal of the study, evaluating the acceptability of the analytical methods, was achieved as the methods provided results sufficiently close to that of the time history analysis.

## 2.2 Influence of strong-motion duration

### Hancock and Bommer (2006)

According to a review paper by Hancock and Bommer (2006), many researchers have studied the effect of strong-motion duration on structural responses in terms of damage. Non-linear time history analyses were mostly adopted to investigate damage indices such as peak rotation, hysteresis energy, fatigue damage, and others. Few studies documented the influence of the strong-motion duration on elastic models, though not related to secondary systems.

### Kaneko (2019)

Kaneko (2019) proposed a method to predict a dynamic amplification ratio or DAR. It is a FRS normalized by the peak floor acceleration (PFA). The author theoretically derived equations that depend on the damping ratios of the primary and secondary structures, the modal frequency of the supporting structure, and the strong-motion duration. As depicted in Figure 2-6, the proposed expressions are in good agreement with the time history analysis results. It can be inferred from this paper that for typical damping ratio ranges of the structure and equipment, the correlation between the strong-motion duration and FRS, albeit slightly, is positive.

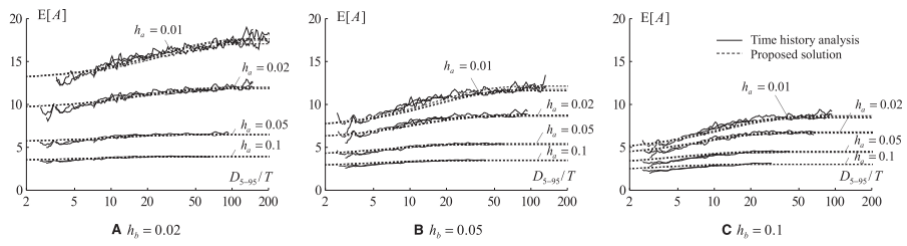


Figure 2-6 Dynamic amplification ratios estimation (Kaneko, 2019)

## 2.3 Spatial Variation

ASCE/SEI 7-16 (2017)

Floor responses vary depending on the location. The influence of elevation has been widely studied and already reflected in the code. ASCE/SEI 4-16 (2017) allows equivalent static analysis under certain circumstances and introduces industry-accepted procedures in ASCE/SEI 7-16 (2016). The equivalent static lateral force, according to the code provision is expressed as

$$F_p = \frac{0.4a_p S_{DS} W_p}{\left(\frac{R_p}{I_p}\right)} \left(1 + \frac{2z}{h}\right) \quad (2.15)$$

$$0.3S_{DS}I_pW_p \leq F_p \leq 1.6S_{DS}I_pW_p \quad (2.16)$$

where,  $F_p$  is a seismic design force;  $a_p$  is an amplification factor listed in Table 13.5-1 or 13.6-1 of ASCE/SEI 7-16 (2016);  $W_p$  is an operating weight of the secondary system;  $I_p$  is an importance factor of the secondary system varying from 1.0 to 1.5;  $R_p$  is a response modification factor varying from 1.0 to 12;  $S_{DS}$  is a spectral acceleration defined in Section 11.4.5 of ASCE/SEI 7-16 (2016).

The next two terms represent an inverse triangular profile assumption of the lateral force distribution.  $z$  is the height of the attachment point with respect to the base, and  $h$  is the average roof height of the building. This linear distribution, proposed by Drake and Bachman (1996), was based on recorded

## Chapter 2 Literature Review

---

floor acceleration data of earthquakes in California, USA. The amplification for the roof height was assumed to be three times the effective peak ground acceleration (PGA).

However, it is stated in ASCE/SEI 4-16 (2017) Section 4.5.2 that the equivalent static method applies to structure, system, and component (SSC) with regular framing. One reason behind this is that equation (2.15) does not account for co-planar spatial variation. NPP buildings are composed of complex geometrical structures where identical rooms are rarely repeated. Also, NPP structures, including the one discussed in this thesis, may wrap around reactor containment buildings (RCB) leaving a seismic gap in between. This means auxiliary buildings have large openings at the center. Considering those circumstances, it may be inaccurate to estimate structural responses with rigid diaphragm assumptions.

### Damolini, El-Bahey, and Oikonomou (2019)

Damolini, El-Bahey, and Oikonomou (2019) compared tri-directional FRS between a simple LMSM and a FEM of an NPP auxiliary control building. As shown in Figure 2-7 (a), the LMSM is a simplified model which is composed of lumped floor masses, and stick elements representing floor stiffnesses. The authors additionally modeled vertical LMSM with beam elements to capture local slab modes.

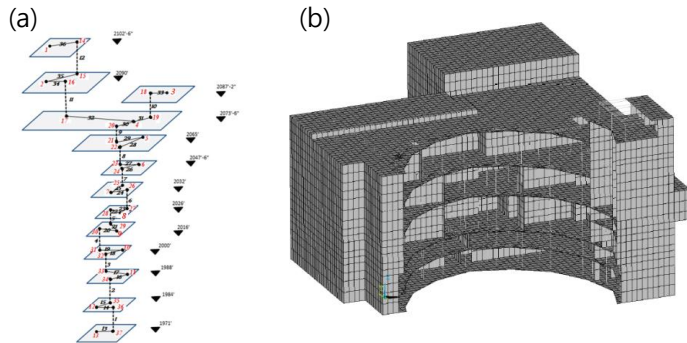


Figure 2-7 Auxiliary Control Building Models: (a) LMSM; (b) FEM  
(Damolini, El-Bahey, and Oikonomou, 2019)

The authors then compared the average FRS of four different elevations. For two horizontal directions, overall amplitudes were similar between the two models. The results of FEM were in smoother shape due to averaging. On the other hand, vertical response varied greatly, as much as 300%. As depicted in Figure 2-8, the range of deviation on the same floor is wide, due to the flexibility of the slab. The authors noted that an average acceleration from the LMSM may lead to unrealistic results.

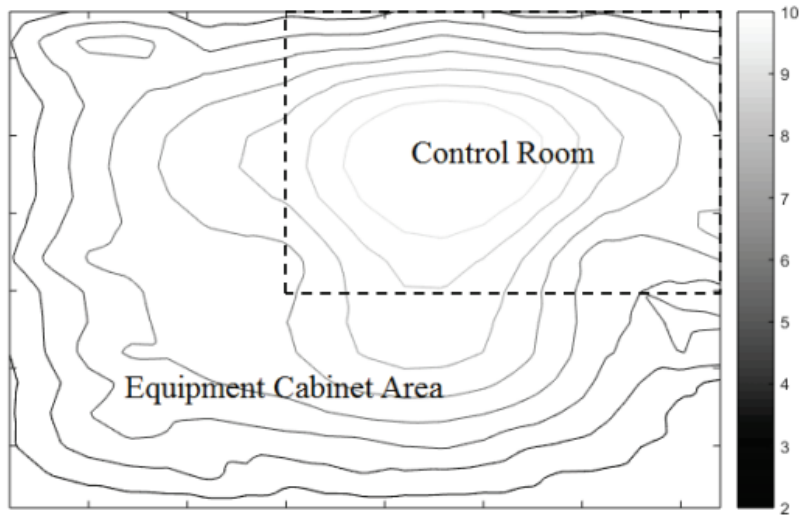


Figure 2-8 Contour plot of peak spectral accelerations (Damolini, El-Bahey, and Oikonomou, 2019)

### Ha, Kim, and Kim (2021)

Ha, Kim, and Kim (2021) compared acceleration time histories recorded in Fukushima Daini nuclear power plant. Three directional FRS based on two couples of accelerometers were compared. The records at the turbine building showed almost identical spectral shapes. On the other hand, significant disparity near the natural frequency of the building appeared at turbine building records.

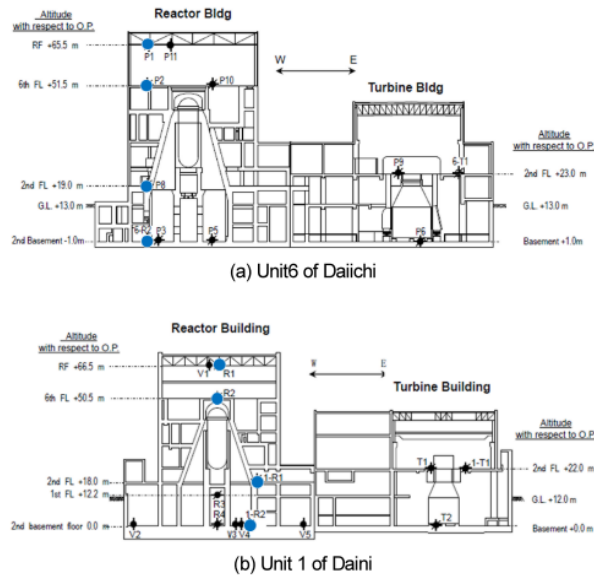


Figure 2-9 Sensor Location (TEPCO, 2011)

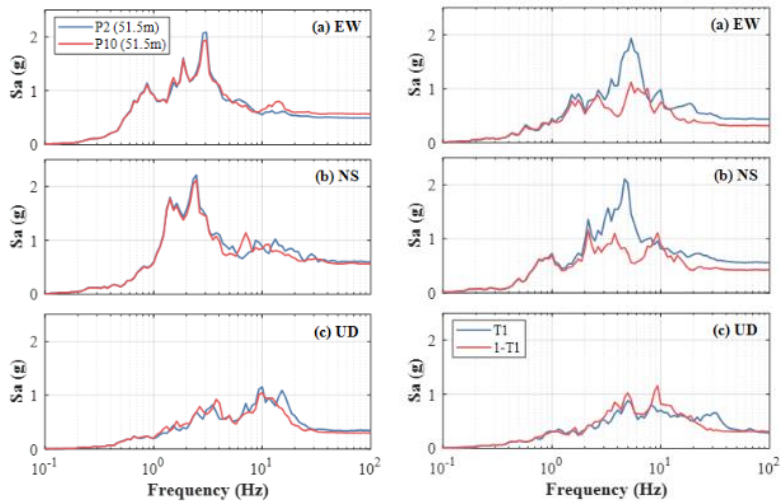


Figure 2-10 Spatial Variation of FRS (Ha, Kim, and Kim, 2021)

Figure 2-10 shows two comparisons of co-planar FRS recorded in the reactor building of Unit 6 of Daiichi (Figure 2-9 (a)) and the turbine building of Unit 1

## Chapter 2 Literature Review

---

of Daini (Figure 2-9 (b)). The latter of the two exhibited that horizontal FRS could greatly vary, as much as 100 %, despite the same elevation. However, for both cases, no significant difference was observed in the vertical direction.

### Jung et al. (2021)

Recently Jung et al. (2021) conducted shaking table tests to investigate FRS variances in a shear wall structure, which is the main structural system of NPP buildings. For input motion, the Gyeongju earthquake (Korea, 2016) was used and three accelerometers were installed as in Figure 2-11. FRS plots in the same figure show spatial variation trends in each direction. For X-direction, the peak of P1 was the greatest due to the torsional effect of the open end. In the case of Y-direction, co-planar FRS were identical as the structure is symmetrical with respect to the Y-axis. The amplitudes of FRS were mainly proportionate to the height of measurement points. Lastly, for the vertical direction, the amplitude of P2 located at the center of the floor was the greater of the three. This was due to the local slab mode corresponding to a higher frequency.

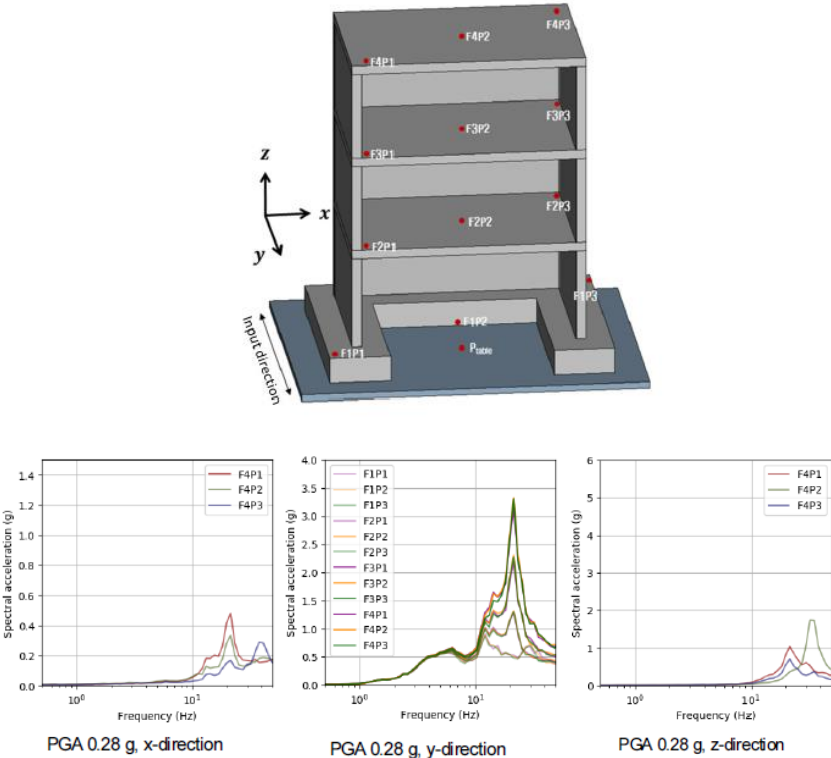


Figure 2-11 Sensor location and tri-directional FRS (Jung et al., 2021)

### 2.4 Treatment of uncertainty

EPRI 3002012994 (Grant, Hardy, and Short, 2018)

As briefly introduced in Chapter 1, EPRI 3002012994 (Grant, Hardy, and Short, 2018) presents two methods to consider variability for seismic fragility analysis. They are deterministic seismic response analysis and probabilistic seismic response analysis, respectively. The former is more engineer-friendly as it follows an orthodox structural analysis process and is advantageous in being able to confirm the influence of each variable. Nonetheless, the latter is a more rigorous ‘probabilistic’ method and is computationally efficient as more variables are incorporated. Detailed procedures will be explained in the later chapters.

To avoid confusion, it is important to note that the deterministic seismic response analysis does account for the variability with probability distributions of the parameters. It is named ‘deterministic’ as the parameter variations are set to selected values, unlike the probabilistic seismic response analysis where they are randomly selected. Hereafter, any process or result, such as FRS, corresponding to two methods will be shortly distinguished by adjectives ‘deterministic’ and ‘probabilistic’ for convenience.

Eggers, Bolourchi, and Ostadan (2011)

Eggers, Bolourchi, and Ostadan (2011) compared probabilistic and deterministic FRS with a quarter-scale containment building SSI model. The

uncertainties of the following parameters were considered: concrete elastic modulus, concrete damping, steel elastic modulus, steel damping, shear-wave velocity, soil shear modulus, and soil damping. At the base, two methods provided close match, yet at the higher elevation, the envelope deterministic FRS were more conservative (Figure 2-12).

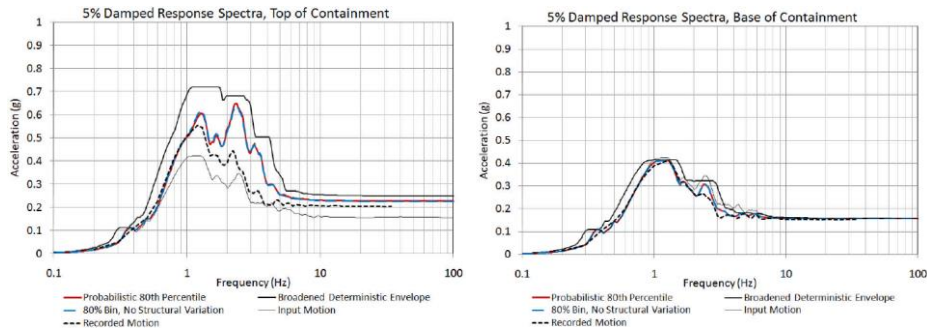


Figure 2-12 Comparison of Deterministic and Probabilistic FRS (Eggers, Bolourchi, and Ostadan, 2011)

### Zinn et al. (2015)

Zinn et al. (2015) performed SSI analyses for two reactor buildings in Switzerland. As in the previous literature, the uncertainties of soil and structure parameters were considered to compare the FRS of the two approaches. The authors concluded that the probabilistic 84% percentile FRS could be the rigorous method for the deterministic envelope FRS, yet at the same time mentioned discrepancies occur between two FRS (Figure 2-13).

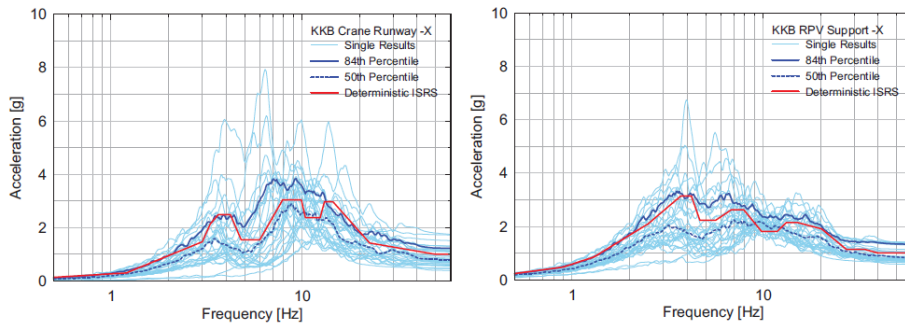


Figure 2-13 Comparison of Deterministic and Probabilistic FRS (Zinn et al, 2015)

### Cappa, Grant, and Nakaki (2017)

Cappa, Grant, and Nakaki (2017) conducted a case study with a simple steel structure with a fixed base. The deterministic FRS showed slight overestimation near peaks. To handle this, the authors present a correction methodology by incorporating variabilities that were neglected in the deterministic response analysis. Despite the use of the corrective measure, the deterministic FRS, especially 84% percentile FRS, overestimated the probabilistic FRS. The authors concluded such conservatism would be acceptable for a less rigorous method and limited range of frequency.

However, this study not only used a simple model but also omitted several variables. SSI analysis was neglected and site response analysis was not performed as well. For the uncertainties, only structure frequency was included. A more complete case study was conducted in the following paper.

Cappa, Appelbaum, and Grant (2019)

Cappa, Appelbaum, and Grant (2019) expanding from Cappa, Grant, and Nakaki (2017), analyzed a reactor building including the SSI effect. Also sources of response variability, besides structure frequency, were included namely soil properties, horizontal direction peak response, structure damping, and others. A similar trend where the deterministic FRS is larger at the natural frequencies of the structure was observed repeatedly (Figure 2-14 (a)). With additional sensitivity study, an analysis without damping variability, and horizontal direction peak response variability, the authors theorized that the effects of two variabilities in the deterministic and probabilistic approaches are different. As in Figure 2-14 (b), when two variabilities are excluded, FRS show comparatively good agreement.

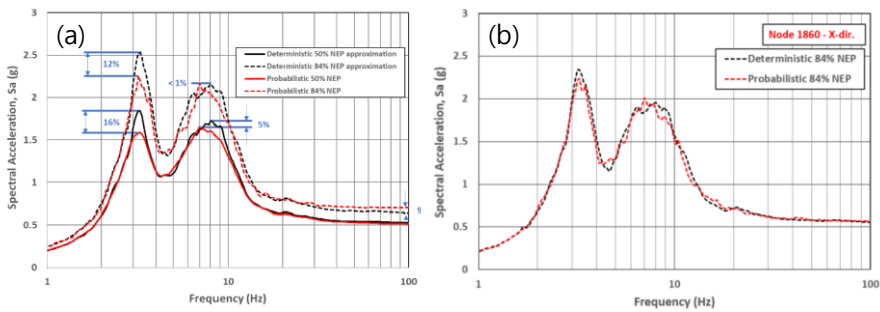


Figure 2-14 Comparison of Deterministic and Probabilistic FRS (Cappa, Appelbaum, and Grant, 2019)

## Chapter 3. Preliminary Study with Simplified Model

### 3.1 Introduction

As a preliminary study, in this chapter factors listed in Table 3-1 are studied with a simple SDOF-SDOF model (Figure 3-1). For Section 3.2 both coupled and uncoupled models were used, whereas only an uncoupled model was used for the other sections. Note that the spatial variation discussed in Section 2.3 is excluded as the simple model is analyzed in 1-D space.

Table 3-1 Factors covered in Chapter 3

Factors	Variables
1. Dynamic coupling effect	Mass ratio
2. Strong motion duration	$D_{5-75}$
3. Treatment of Uncertainty	
3.1. Deterministic	(method itself)
3.2. Probabilistic	

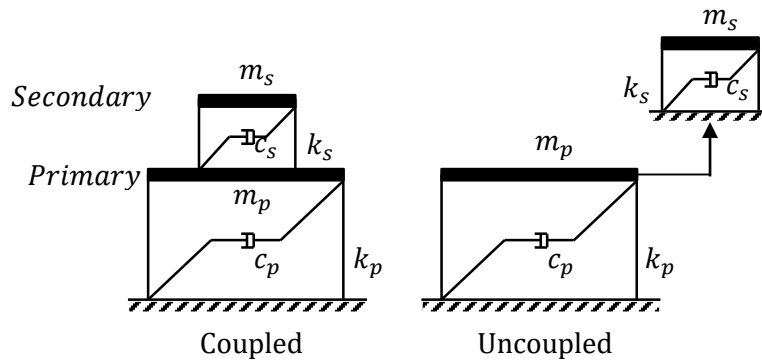


Figure 3-1 Simplified SDOF-SDOF Shear Building Model

Dynamic coupling effect

Many researchers have shown that considering the dynamic coupling effect reduces excessive conservatism in the resonant case where the mass ratio is high. A direct integration method was used. This is because the computational cost for analyzing coupled 2DOF model as in Figure 3-1 is low and it represents closest to the reality. The mass ratio was varied to examine its effect on the response of the secondary system.

Strong motion duration

SRP 3.7.1 (NRC, 2014) writes that for design time history strong motion duration should be longer than 6 s. The strong motion duration is defined as the Arias intensity from 5% to 75%. However, this may not be appropriate for Korean Peninsula where earthquake satisfying such criterion is very rare.

In this section total of 44 sets of spectrally equivalent ground motions were prepared. Each set comprised of short, medium, and long duration earthquakes divided by 6 s and 20 s.

## Chapter 3 Preliminary Study with Simplified Model

---

### *Treatment of Uncertainty*

The most structural analysis assumes deterministic values, however in reality they exist as stochastic distribution. Young's modulus of concrete, for instance, cannot be identical for every component. Incorporating these uncertainties was performed via two approaches, deterministic and probabilistic.

### 3.2 Dynamic coupling effect

Two models of Figure 3-1 were numerically solved via Newmark's beta method (Chopra, 2014). Dynamic properties used in the analysis are summarized in Table 3-2. The natural frequency of the primary structure was set to 5 Hz, representing the high frequency of the NPP structures. Damping ratios were decided based on EPRI report (Grant, Hardy, and Short, 2018) where 4 % is for reinforced concrete structures and 3 % is for massive components or instrument racks. For the uncoupled model, a typical FRS generating procedure was performed. Coupled model on the other hand was considered as a combined single unit. Therefore, the equation of motion was solved in matrix form.

$$\mathbf{M}_c \ddot{\mathbf{u}} + \mathbf{C}_c \dot{\mathbf{u}} + \mathbf{K}_c \mathbf{u} = -\mathbf{M}_c \mathbf{U}_b \ddot{\mathbf{u}}_g \quad (3.1)$$

Where,

$$\mathbf{M}_c = \begin{bmatrix} m_p & \\ & m_s \end{bmatrix} \quad (3.2)$$

$$\mathbf{C}_c = \begin{bmatrix} c_p + c_s & -c_s \\ -c_s & c_s \end{bmatrix} \quad (3.3)$$

$$\mathbf{K}_c = \begin{bmatrix} k_p + k_s & -k_s \\ -k_s & k_s \end{bmatrix} \quad (3.4)$$

where, symbols m, c, k stand for mass, damping coefficient, stiffness, and subscripts p, s, c indicate primary structure, secondary structure, and coupled structure.  $\mathbf{U}_b$  is a unit displacement vector.  $\ddot{\mathbf{u}}_g$  is ground motion acceleration time history. For ground input motion, El centro (1940) acceleration time history shown in Figure 3-2 was used.

## Chapter 3 Preliminary Study with Simplified Model

---

Table 3-2 Dynamic Properties of the Model

	Primary	Secondary
Mass	10,000 kg	10, 50, 100, 500 kg
Frequency	5 Hz	1 - 50 Hz
Damping ratio	0.04	0.03

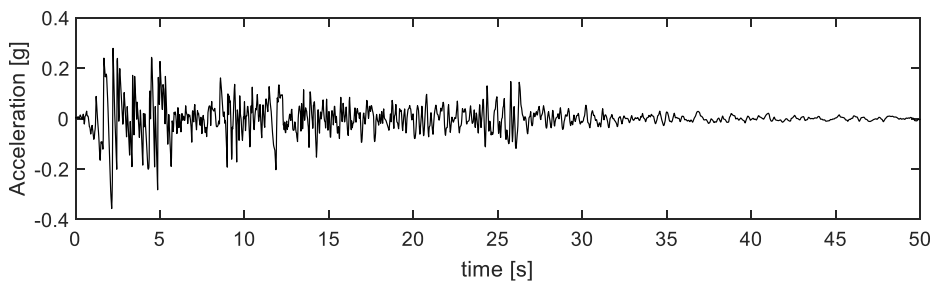


Figure 3-2 El centro (1940) acceleration time history

Figure 3-3 shows the FRS of the uncoupled and coupled model of four different mass ratios. Clearly depicted with a solid grey line, when the frequency of the secondary system tunes to that of the primary system, its response – in this case, spectral acceleration – is greatly amplified due to resonance. PGA of the input motion was 0.36 g and the amplitude of uncoupled model FRS is 6.53 g, which is nearly 18 times greater. On the other hand, coupled model FRS plotted in black lines showed a trend of decreasing peak values as the mass ratio increased. Peak amplitude reduction rates were summarized in Table 3-3.

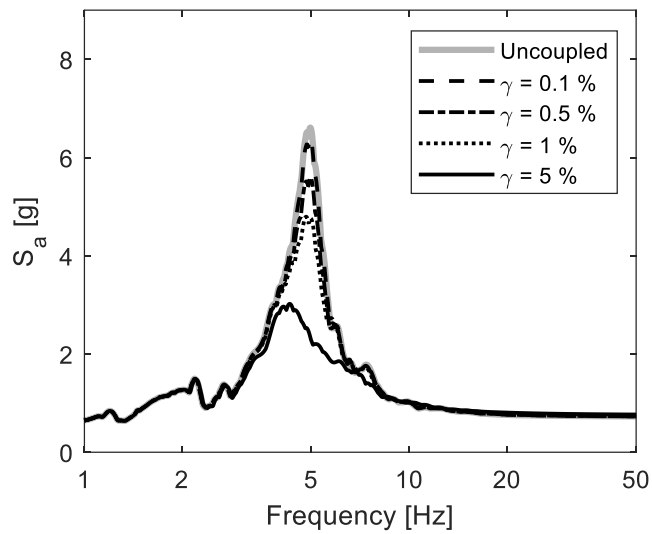


Figure 3-3 Uncoupled and coupled FRSSs

Table 3-3 Peak amplitude reduction due to dynamic coupling effect

Mass ratio	Uncoupled Peak Response	Coupled Peak Response	Reduction
0.1 %	6.53 g	6.07 g	7.04 %
0.5 %		5.34 g	18.22 %
1.0 %		4.67 g	28.48 %
5.0 %		2.91 g	55.43 %

### 3.3 Influence of strong-motion duration

#### 3.3.1 Ground motion selections

Nearly six hundred earthquake records were gathered from PEER Ground Motion Database ([peer.berkeley.edu/peer-strong-ground-motion-databases](http://peer.berkeley.edu/peer-strong-ground-motion-databases)), Center for Engineering Strong Motion Data ([www.strongmotioncenter.org](http://www.strongmotioncenter.org)), and National Research Institute for Earthquake Science and Disaster Prevention ([www.kyoshin.bosai.go.jp](http://www.kyoshin.bosai.go.jp)). Record collections satisfied two requirements: minimum magnitude of 5.0 and minimum PGA of 0.1 g.

In the thesis, strong-motion duration was defined as a duration equivalent of 5 % to 75 % cumulative Arias intensity. This measure written as  $D_{5-75}$  is thought to be suitable for structural analysis (Foschaar et al., 2012). Initially, strong motion duration was calculated for all records and categorized into three groups based on two thresholds 6 s and 20 s. The former was based on SRP 3.7.1 (USNRC, 2014) criterion which enforces a minimum of 6 s of strong-motion duration of design ground motion used in seismic fragility analysis. The latter, on the other hand, was chosen for the even distribution of short records and long records. With two thresholds set, the motions were divided into three groups: 1)  $D_{5-75}$  shorter than 6 s; 2)  $D_{5-75}$  between 6 s and 20 s; 3)  $D_{5-75}$  longer than 20 s. The second group was the reference spectrum, the ones with the least-squares were selected from two other groups. Scale factor between 0.2 to 5.0 was applied in this process while the spectral shape was left intact. Due to the scale factor constraints, few sets inequivalent were sifted out with the naked eye. Total 44 triads were selected and the list with detailed information is attached in Appendix A.

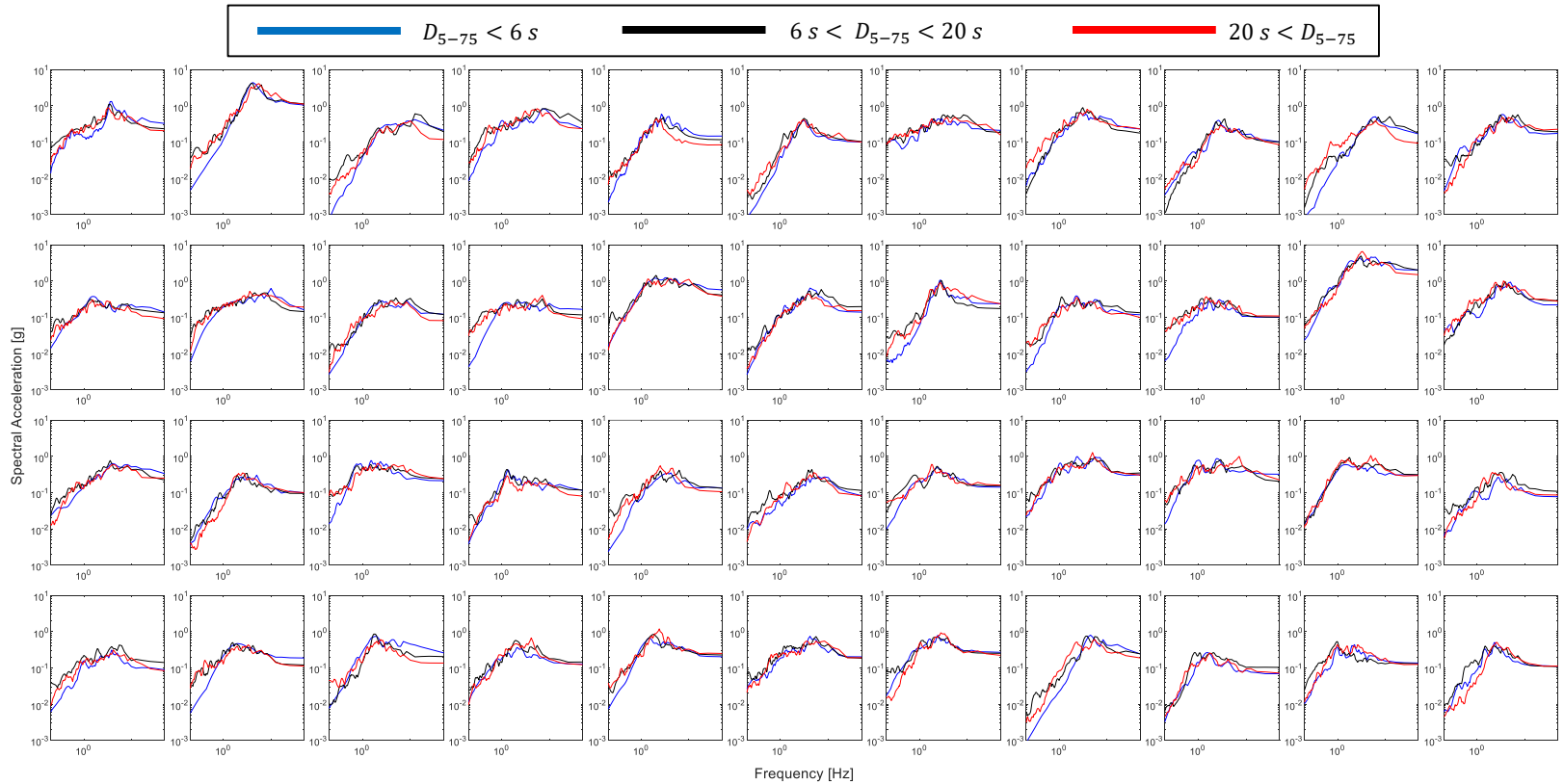


Figure 3-4 5 % response spectra of spectrally equivalent ground motions

### 3.3.2 Duration dependency

With 44 sets as shown in Figure 3-4, dynamic analyses were performed. The uncoupled model was used to yield forty-four sets of FRS. As the scale factor was limited between 0.2 and 5.0, PGAs varied within each set. FRSs, therefore, were normalized by peak floor acceleration. Hereafter these normalized spectra are referred to as amplification spectra.

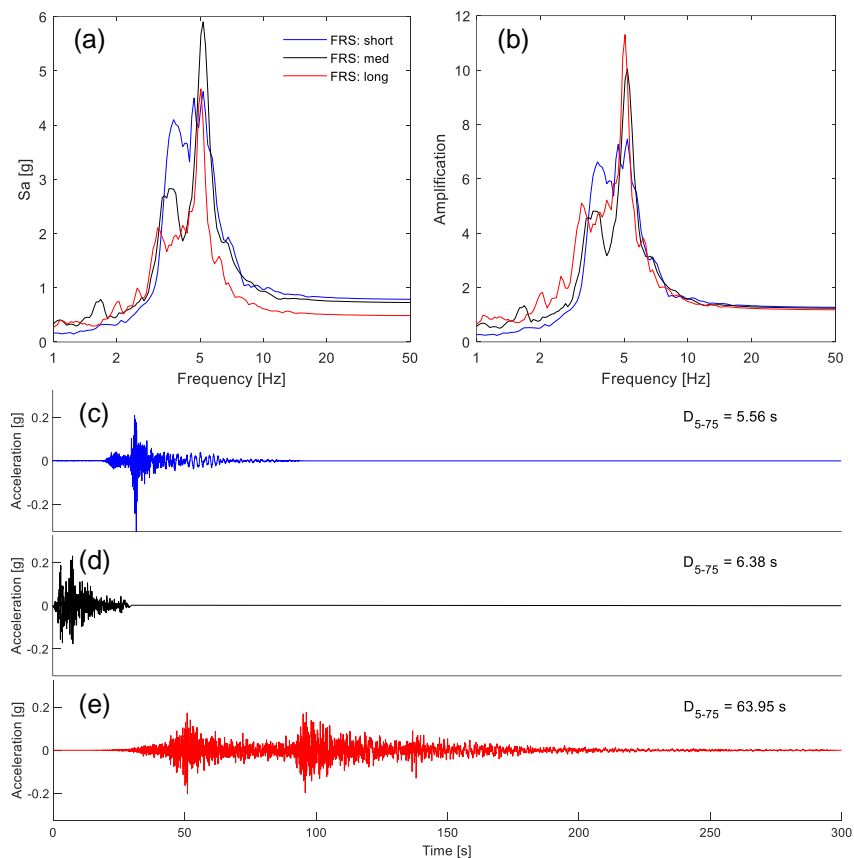


Figure 3-5 An example of spectrally equivalent records: (a) FRS; (b) amplification spectra; (c),(d),(e) time histories

Figure 3-5 illustrates the aforementioned process with the first set. The time

histories are from the Kocaeli earthquake (Turkey, 1999), the Chi-Chi earthquake (Taiwan, 1999), and the Tohoku earthquake (Japan, 2011). The Kocaeli and the Tohoku earthquake records were scaled by a factor of 1.39 and 1.05. In the case of the FRS (a), the peak value of the medium record was greater than the other two records. However, the amplification values at the resonant frequency were proportionate to the strong-motion duration of the records.

To avoid the biased impression this example gives, it is important to stress two shortcomings. One is obviously that this is one of the sets where contradictory cases do exist. Moreover, the high-frequency range, where the natural frequency of equipment falls into, is that of interest. Though in this chapter, the SDOF structure model has a single mode at 5 Hz where the ground motion is amplified. So the scope is focused on that tuning frequency.

Forty-four sets of the amplification spectra were then averaged in each group as a result, three mean amplification spectra were generated as in Figure 3-6. Unlike the previous example, tuned amplification values were large in the order of the medium records, the long records, and the short records. Disparities between the spectra in the untuned frequency range were trivial.

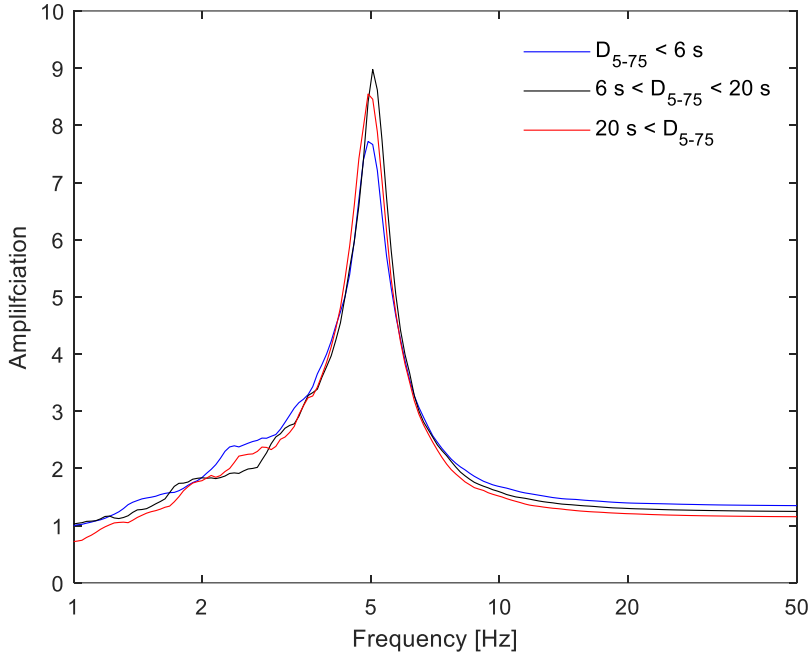


Figure 3-6 Mean amplification spectra

In form of mean spectra,  $D_{5-75}$  information of each record is lumped as a group. To investigate the correlation between amplification and  $D_{5-75}$ , individual records were plotted in Figure 3-7, where abscissa is  $D_{5-75}/T$  and ordinate is amplification. Each solid circle represents each record and the color scheme used in Figure 3-4 - Figure 3-6 was maintained. The abscissa term is from Kaneko (2019),  $T$  standing for tuning period in this case 0.2 s. Consequently, the records at the tuning frequency were plotted, which is reasonable as the influence of strong-motion duration is most dominant.

$$\text{Amplification} = \left(1 - \exp\left(-\alpha \frac{D_{5-75}}{T}\right)\right) \beta + \gamma \quad (3.5)$$

### Chapter 3. Preliminary Study with Simplified Model

Additionally, a non-linear regression line fitted to the records was added. Its mathematical form (3.5) is adopted from Kaneko (2019). The fitted line, closely resembling Figure 2-6, shows that the overall correlation between the amplification and  $D_{5-75}$  is subtle. Though up to fifty, a weak positive slope is noticeable, the line plateaus afterward, converging to a certain bound.

On the regression line,  $D_{5-75}$  corresponding to the Gyeongju earthquake (1.3 s) was marked as a yellow circle. Considering the minimum  $D_{5-75}$  requirement of 6 s, the regression line estimates amplification as 8.45. Compared to this value, that of Gyeongju is 7.18 which is 15 % lesser.

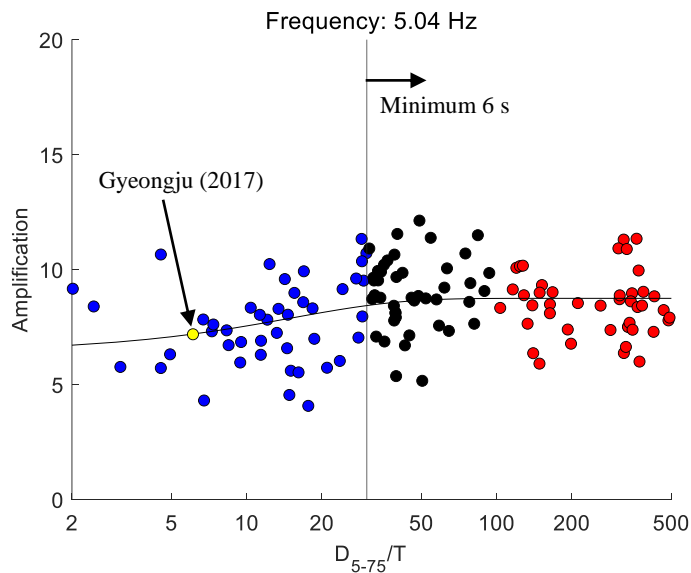


Figure 3-7 Amplification vs.  $D_{5-75}/T$  plots at the tuning frequency

The above investigation showed a relation between amplification and  $D_{5-75}$ . Yet, the information of spectral equivalence was not considered. The purpose of preparing spectral equivalent records was to separate frequency contents

### Chapter 3 Preliminary Study with Simplified Model

---

from strong-motion duration. So within each triad, the ratios of amplification were calculated for the short and long records pairs and the short and medium records pairs. Chandramohan et al. (2016) calculated the  $D_{5-75}$  ratio and showed a negative correlation between the collapse capacity ratio and the  $D_{5-75}$  ratio. Following the authors' procedure, the  $D_{5-75}$  ratio was prepared plotted against the amplification ratio as in Figure 3-8. Unlike the authors who used two groups, short and long, this thesis divided the records into three groups. Consequently, two groups, 1) the short records to the long records ratio; 2) the short records to the medium records ratio, were prepared.

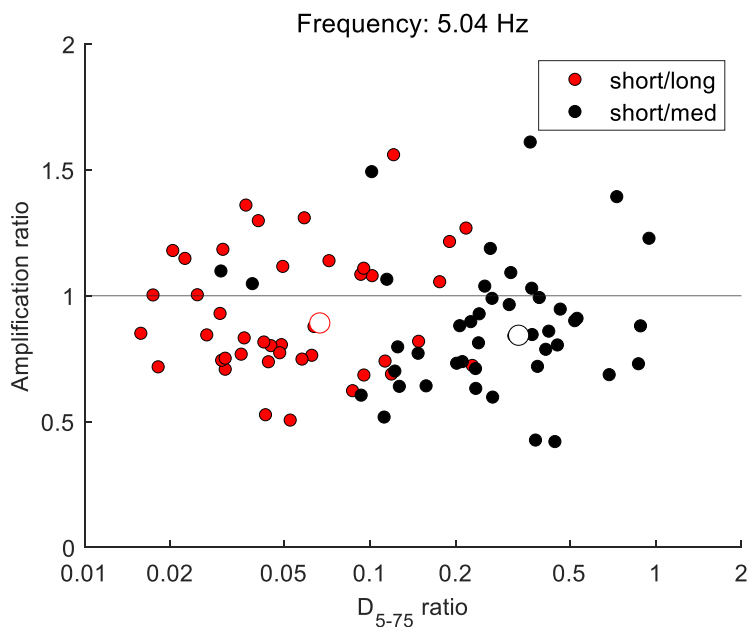


Figure 3-8 Amplification ratio vs.  $D_{5-75}$  ratio plot at the tuning frequency

No correlation between the amplification ratio and the  $D_{5-75}$  ratio was clear. Regression lines were omitted for this reason. Instead horizontal lines

### Chapter 3. Preliminary Study with Simplified Model

---

representing the amplification ratio of unity were plotted. If a data point is below this line, the amplification of the shorter record is lesser. As representative values arithmetic means were added, again indicated by larger empty circles, along with individual data points. Pairs in which the amplification ratio exceeds the unity exist, yet on average the amplifications of the short records are 89 % and 84 % level of the long and the medium records.

### 3.4 Treatment of uncertainty

In this section, two seismic response analysis methods by EPRI technical report (Grant, Hardy, and Short, 2018) were compared. As for the background of the fragility concept, which is the basis of the two methods, it is discussed in Section 5.2.

#### 3.4.1 Input ground motions

For dynamic analysis, linear time history analysis was used. As will be explained later, the probabilistic seismic response analysis calls for at least 30 analyses. Hence a minimum of thirty sets of ground motion accelerograms were required. Thirty sets of time history were acquired by courtesy of professor J.H. Park through personal contact, and the following procedure was applied. From the ground motion list in NUREG/CR-6728 (NRC, 2001), more than fifty records of which magnitudes are between 6 to 7 and hypocenter distances up to 200 km, were selected. These seed motions were then matched to the median response spectrum of NUREG/CR-0098 (NRC, 1978). Response spectrum matched ground motions were then scaled to satisfy the criteria of SRP 3.7.1 in NUREG/CR-0800 (NRC, 2014). Summarized in Table 3-4 are the seed motions of final criteria-satisfying ground motions. For more specific information refer to the references.

### Chapter 3. Preliminary Study with Simplified Model

Table 3-4 List of earthquake records

No.	Earthquake Name	Year	Station Name	M	R (km)	Vs30 (m/s)
1	Helena Montana-01	1935	Carroll College	6.00	2.1	593
2	Parkfield	1966	Cholame-Shandon Array #8	6.19	12.9	257
3	Parkfield	1966	Temblor pre-1969	6.19	16.0	528
4	Borrego Mtn	1968	San Onofre-So Cal Edison	6.63	129.1	443
5	San Fernando	1971	Pacoima Dam (upper left abut)	6.61	0.0	2016
6	San Fernando	1971	San Onofre-So Cal Edison	6.61	124.8	443
7	San Fernando	1971	Santa Felita Dam (Outlet)	6.61	24.7	389
8	San Fernando	1971	Upland-San Antonio Dam	6.61	61.7	487
9	Imperial Valley-06	1979	Superstition Mtn Camera	6.53	24.6	362
10	Mammoth Lakes-03	1980	Long Valley Dam (L abut)	5.91	10.3	537
11	Mammoth Lakes-06	1980	Bishop-Paradise Lodge	5.94	18.9	585
12	Victoria Mexico	1980	Cerro Prieto	6.33	13.8	472
13	Coalinga-01	1983	Parkfield-Cholame 2E	6.36	42.0	523
14	Coalinga-01	1983	Parkfield-Gold Hill 3W	6.36	38.1	511
15	Coalinga-01	1983	Parkfield-Vineyard Cany 4W	6.36	33.3	386
16	Morgan Hill	1984	Corralitos	6.19	23.2	462
17	Morgan Hill	1984	Coyote Lake Dam-Southwest Abutment	6.19	0.2	561
18	Morgan Hill	1984	Gilroy Array #6	6.19	9.9	663
19	Whittier Narrows-01	1987	Calabasas-N Las Virg	5.99	52.8	404
20	Whittier Narrows-01	1987	Castaic-Hasley Canyon	5.99	62.6	421
21	Whittier Narrows-01	1987	Castaic-Old Ridge Route	5.99	70.0	450
22	Whittier Narrows-01	1987	Malibu-Point Dume Sch	5.99	61.5	350
23	Whittier Narrows-01	1987	San Gabriel-E Grand Ave	5.99	0.0	401
24	Loma Prieta	1989	LGPC	6.93	0.0	595
25	Georgia USSR	1991	Ambralauri	6.20	63.5	400
26	Northridge-01	1994	Duarte-Mel Canyon Rd	6.69	48.4	459
27	Northridge-01	1994	Rancho Cucamonga- Deer Can	6.69	79.8	509
28	Northridge-01	1994	Villa Park-Serrano Ave	6.69	76.4	417
29	Northridge-01	1994	West Covina-S Orange Ave	6.69	51.5	335
30	Northridge-01	1994	Wrightwood-Jackson Flat	6.69	64.5	663

### 3.4.2 Site response analysis

In the thesis, SSI analysis is neglected. However, to incorporate the variabilities inherent in soil properties, site response analysis was performed by Strata software (Kottke and Rathje, 2008).

Out of 9 generic soil profiles of an operating NPP, the stiffest soil condition was selected (KEPCO, 2012). The selected soil profile consists of two layers: 1) a rock layer, where average shear wave velocity is 1,829 m/sec (6,000 ft/sec) and unit weight is 2,323 kg/m<sup>3</sup> (145 lb/ft<sup>3</sup>), up to 30 m (100 ft) below ground surface; 2) a harder rock layer of 2,804 m/sec (9,200 ft/sec) shear wave velocity and 2,483 kg/m<sup>3</sup> (155 lb/ft<sup>3</sup>) unit weight, ranging from 30 m (100 ft) down to the bedrock which is thought to be below 300 m (1,000 ft) in depth. For the selected soil profile, variabilities of the shear wave velocity, normalized shear stiffness, and damping ratio were sampled. Two models included in the software were adopted. The first model describes the statistical distribution of shear-wave velocity, developed by Toro (1995). The other model, by Darendeli (2001) describes the distribution of the normalized shear stiffness and damping ratio.

Thirty sets of soil properties corresponded to the thirty input time histories one-to-one. This means one of thirty soil properties sets is randomly selected and likewise, one of the thirty inputs was arbitrarily picked, non-restoring. Repeating this until exhaustion of the samples gives thirty pairs of the soil properties and the input.

In this chapter, out of three directional (two orthogonal horizontal and vertical) ground motions only one horizontal, the H1 direction was used. For

each case, the site response analysis was then performed to render thirty acceleration time histories that will excite the fixed-base of the model. Response spectra of these accelerograms so-called, foundation input response spectra or FIRS, are shown in Figure 3-9. Before the site response analysis, input response spectra resemble the target response spectrum almost identical (Figure 3-9 (a)). On the other hand, dispersion of individual spectrum, due to the variabilities of the soil properties is visible in the FIRS. The spectral shape of the median spectrum, though, is well maintained implying that thirty FIRS are averagely complying with the target response spectrum while variabilities of the soil properties are fully included.

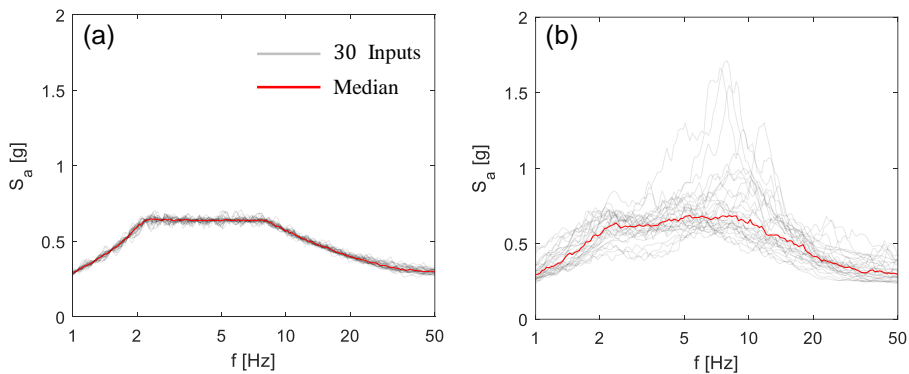


Figure 3-9 Input response spectra (H1 direction): (a) NUREG/CR-0098 compatible inputs; (b) FIRS post site response analysis

### 3.4.3 Deterministic seismic response analysis

For deterministic seismic response analysis, the variabilities of soil properties are considered by analyzing three varying cases of soil properties. However, it is difficult to distinguish them from input motion time histories. Therefore, from 30 H1 direction accelerograms results of site response analysis, five were chosen, which is the minimum number to account for random phasing (Grant, Hardy, and Short, 2018). They were selected based on the least-squares of logarithmic standard deviations between five and thirty sets. In this way, variabilities of phasing and soil properties were simultaneously considered at a similar level to that of the probabilistic seismic response analysis.

Next, three cases for each variable were prepared as in Table 3-5. For instance to estimate the variability of structure stiffness cases 1,2,3 are analyzed. Likewise, case 1,6,7 are analyzed to calculate the variability of equipment damping. Then case 1 would be reasonably included three times or weighted three.

Table 3-5 Deterministic case designations

No.	$k_s$	$\delta_s$	$\delta_e$
1	BE	BE	BE
2	UB	BE	BE
3	LB	BE	BE
4	BE	UB	BE
5	BE	LB	BE
6	BE	BE	UB

### Chapter 3. Preliminary Study with Simplified Model

---

7	BE	BE	LB
$k_s$ : structure stiffness $\delta_s$ : structure damping ratio $\delta_e$ : equipment damping ratio			

A typical method for selecting LB and UB stiffnesses is taking  $\pm 1$  standard deviation from BE stiffness. An identical approach was applied to select LB and UB for structure and equipment damping ratios. Best estimate values and coefficients of variance (COV) are summarized in Table 3-6. COVs of structure damping ratio and structure stiffness were chosen according to EPRI (Grant, Hardy, and Short, 2018). COV of equipment damping ratio was assumed.

Table 3-6 Properties of the simplified model

Variable	Best Estimate	COV
Soil	Included in the results of SRA	-
Damping ratio		
Primary	5 %	0.34
Secondary	2 %	0.30
Frequency	5.00 Hz	-
Stiffness	-	0.30

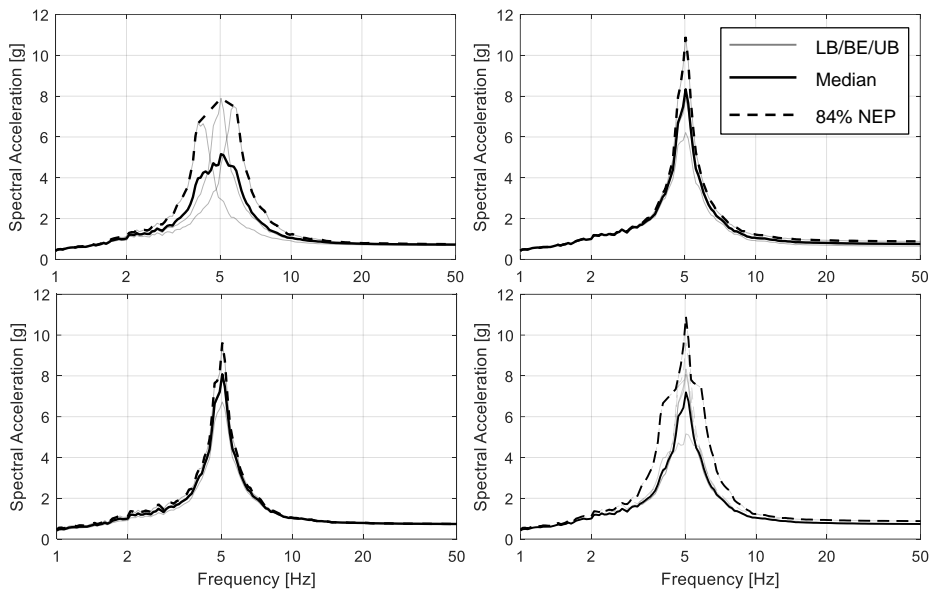


Figure 3-10 FRS from deterministic seismic response analyses - (a) structure stiffness, (b) structure damping, (c) equipment damping, (d) three parameters considered

Figure 3-10 shows the median and 84% non-exceedance probability (NEP) FRS. (a) through (c) shows the variability of each parameter. For example in Figure 3-10 (a) grey lines depict FRS corresponding to LB, BE, and UB. Since the LB case used one standard deviation lesser stiffness value, the FRS peak occurs at a lower frequency and vice versa for the UB case. For each case, five input motions were used and the grey lines are the average of five FRS. Then median FRS was estimated as the average of the three, and 84% NEP FRS defined as an envelope curve of them was obtained. The same procedure was repeated for structure damping and equipment damping. Figure 3-10 (d) shows FRS where variabilities of three parameters are considered. Median FRS was obtained by averaging median FRSs and 84% NEP FRS by enveloping three

84% NEP FRSs (Grant, Hardy, and Short, 2018).

The influences of each variable can be implied from Figure 3-10. It is most notable for the structure frequency parameter. As the peaks of LB and UB occur at different frequencies, the averaged spectral accelerations near the resonance frequency are significantly reduced. On the other hand, the two damping ratios are less influential. The BE FRSs are almost identical to the averaged FRSs, which means considering the variabilities of the damping parameters insignificantly affect the structural responses.

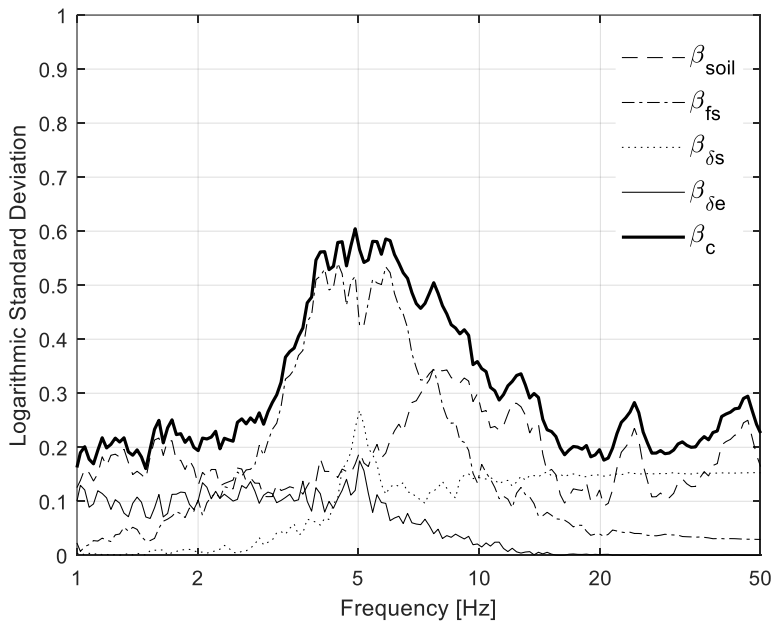


Figure 3-11 Logarithmic standard deviations from deterministic seismic response analyses

Given the median and 84% NEP FRSs, logarithmic standard deviations for

### Chapter 3 Preliminary Study with Simplified Model

---

parameters were obtained by the following equation.

$$\beta_i = \ln\left(\frac{S_{a,84\%}}{S_{a,M}}\right) \quad (3.6)$$

As spectral accelerations are in the form of a spectrum, the logarithmic standard deviations also varied depending on frequency. Figure 3-11 shows spectra of variabilities and  $\beta_c$ , calculated by the square root of the sum of the squares (SRSS). Within the low-frequency range (1-10 Hz), the variability of structure stiffness contributed the most to the overall variability of seismic response. At the high-frequency range, past 10 Hz, variabilities of soil properties, ground motions, and structure damping comprised the majority of the total variability.

The logarithmic standard deviation representing the variability is a foreign concept in conventional structural analysis. Though as will be explained in Section 5.2, it is an important parameter in the context of seismic fragility analysis. Accordingly, its estimation method was briefly mentioned here.

### 3.4.4 Probabilistic seismic response analysis

#### Latin hypercube simulation

Probabilistic seismic response analysis performs multiple analyses to obtain a median response for seismic fragility analysis. Sampling techniques are used to account for variabilities and EPRI 3002012994 (Grant, Hardy, and Short, 2018) allows Monte Carlo simulation (MCS) or Latin hypercube simulation (LHS). LHS is used in the thesis as it is advantageous in lower cost and sufficient accuracy. According to ASCE/SEI 4-16 (2017), at least 30 simulations are required for LHS, hence accommodated in the thesis.

To extract  $N$  samples, a probability distribution is divided into  $N$  regions where each bin has a probability of  $1/N$ . This process is illustrated in Figure 3-12 below. For example, a parameter is assumed to follow the lognormal probability distribution of  $LN(1.0, 0.30)$  which means the median value of 1 and variability of 0.30. The solid line in Figure 3-12 (a) is a cumulative distribution function and sampled values are marked with the '×' symbol. Gridlines equally divide regions with  $1/30$  probability and each region has exactly one sample.

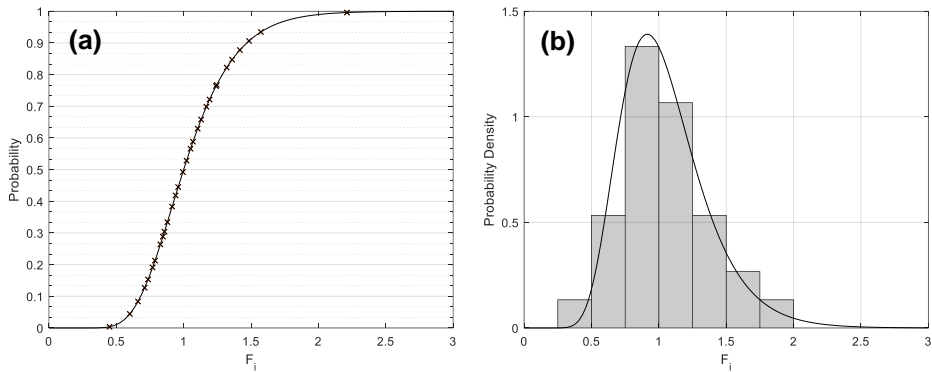


Figure 3-12 Thirty scale factors for equipment frequency sampled from LHS

For sampling following equation was used.

$$x_i = x_m \exp\left(\beta \Phi^{-1}\left(\frac{i-1+rnd_i}{N}\right)\right) \quad (3.7)$$

$x_i$ : sample

$x_m$ : median value

$\beta$ : logarithmic standard deviation

$rnd_i$ : a random number between 0 and 1

$N$ : number of samples

Figure 3-12 (b) shows a histogram of samples and the probability density function of the assumed distribution. Samples fit well with the distribution, guaranteeing a median-centered model.

For three parameters  $k_s, \delta_s, \delta_e$  LHS was performed to obtain thirty sets of samples with variabilities. COVs in Table 3-6 were used to calculate logarithmic standard deviations with the following equation (3.8). Frequencies

---

### Chapter 3. Preliminary Study with Simplified Model

---

corresponding to sampled stiffnesses and sampled damping ratios are summarized in Table 3-7.

$$\beta = \sqrt{\ln(1 + COV^2)} \quad (3.8)$$

Table 3-7 Thirty  $f_s, \delta_s, \delta_e$  by Latin hypercube simulation

No.	$f_s$ [Hz]	$\delta_s$ [%]	$\delta_e$ [%]
1	5.30	5.49	1.90
2	5.67	5.17	2.45
3	4.71	7.16	1.44
4	4.90	3.63	1.30
5	5.29	6.35	2.00
6	5.90	2.93	1.86
7	3.81	7.73	2.30
8	5.02	4.77	2.35
9	4.35	7.93	2.72
10	4.27	5.83	2.12
11	6.49	6.09	3.11
12	4.18	5.12	1.54
13	3.39	5.95	1.66
14	5.61	4.35	1.07
15	4.50	8.65	2.55
16	4.50	5.66	1.59
17	6.38	3.78	3.28
18	5.22	4.57	1.26
19	4.08	4.73	2.00
20	5.84	4.47	1.37
21	5.09	3.96	2.07
22	4.79	2.69	2.22
23	6.12	3.39	1.81
24	4.63	6.41	2.83
25	5.51	4.99	2.67
26	5.39	4.19	1.66
27	4.73	3.50	2.26
28	3.99	6.92	1.77
29	4.95	5.26	3.82
30	7.29	4.14	1.73

## Chapter 3 Preliminary Study with Simplified Model

---

Each sample from three parameters randomly constitutes one bin representing a structural model. Then one of thirty ground motion records from section 3.4.3 was randomly assigned to the model. For the other 29 sets, three sampled parameters and the ground motion were matched consecutively.

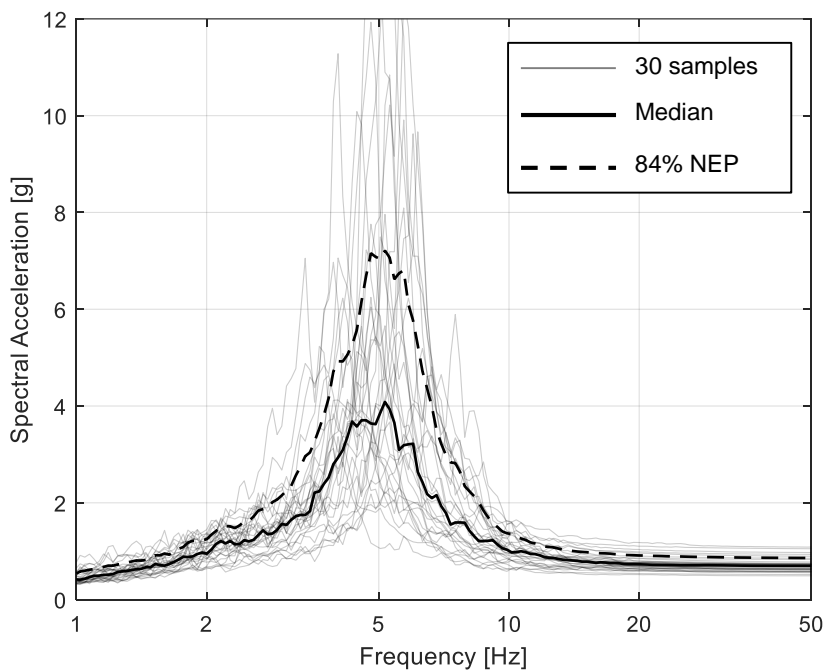


Figure 3-13 FRSs from probabilistic seismic response analysis

Figure 3-13 shows thirty probabilistic FRSs as a result of thirty simulations. Depicted as grey lines, exhibit a wide range of variabilities. For some extreme cases, spectral accelerations near the natural frequency of structure exceeded 12 g, 40 times the input PGA. Despite those outliers, median FRS plotted in solid black line was lowered as the sampled parameters are median-centered.

### 3.4.5 Comparison

The results of deterministic seismic response analysis and those of probabilistic seismic response analysis were compared. Median and 84 % NEP FRSs and logarithmic standard deviations were drawn in Figure 3-14 to compare. Solid lines represent deterministic seismic response analysis and broken lines for probabilistic seismic response analysis. Figure 3-14 (a), (b) show that probabilistic FRSs have lesser amplitudes near the tuning frequency. Peak values of probabilistic median and 84% NEP FRSs are 43%, 34% smaller than those of deterministic FRSs. This reduction is mainly due to structure frequency variability. It can be inferred from Figure 3-14 that for probabilistic seismic response analysis, governing parameter contributing to the overall variability would be structure frequency. Recall Figure 3-10 (a) where averaging three cases of structure frequencies greatly reduced the amplitude of the FRS. Likewise, in probabilistic seismic response analysis more cases or thirty samples were used and their weights were not diluted. Though median FRS considering only structure frequency is small, because of the other two greater FRSs (Figure 3-10 (b), (c)), the averaged final FRS is closer to them.

The best estimate median FRS is also plotted in Figure 3-14 (a) to show the effectiveness of the deterministic approach. For the BE FRS, median values of structure and equipment properties and five records used for deterministic analysis were applied. This is considered to be a true ‘deterministic’ FRS, where no variabilities, except the random phasing, are accounted for. Two spectra closely overlap except at the tuning frequency where the amplitudes of acceleration are 9 % apart.

Composite logarithmic standard deviations are plotted in Figure 3-14 (c). A

### Chapter 3 Preliminary Study with Simplified Model

---

similar tendency was observed throughout the entire frequency range, and values were close to identical. One observation is that variation of deterministic analysis exhibits sporadic peaks, especially near the tuning frequency. This arises from the 84% NEP FRS definition. By filling valleys between spectra, an abrupt change in amplitude was made, propagating into the variability. This result contradicts EPRI (Grant, Hardy, and Short, 2018) where it is stated that lower overall variability is expected for probabilistic seismic response analysis, compared to deterministic analysis. One possible explanation would be the number of simulations. Though the minimum number of samples is thirty, this may be insufficient for lesser variabilities. Eggers and Ostadan (2011) compared FRS with thirty-two samples and sixty samples with the baseline set with MCS with 2,000 samples. The authors reported that for a narrow frequency range, 80% NEP FRS varied as much as 9%. This result suggests less variability is available with larger sample sizes.

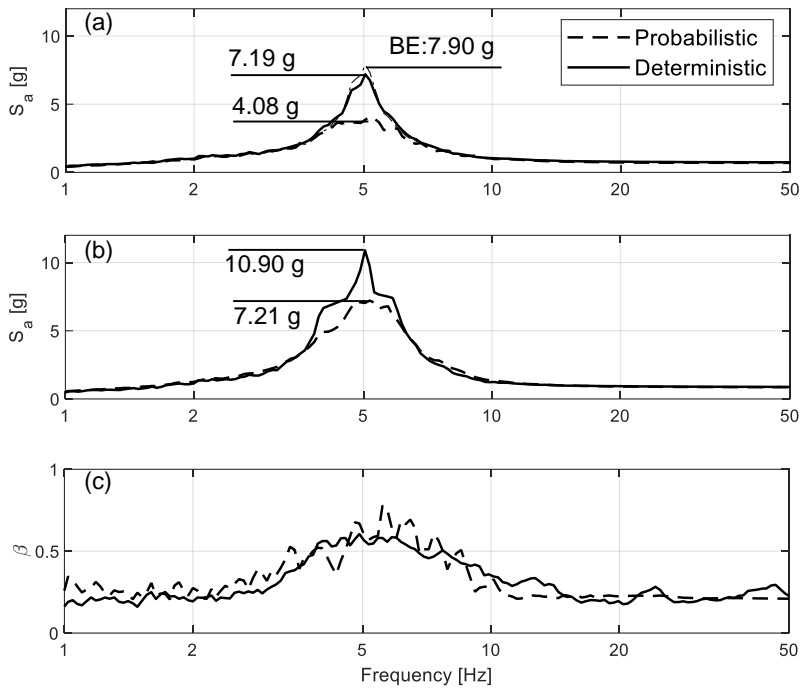


Figure 3-14 Seismic response analyses comparison - (a) Median FRFs; (b) 84% NEP FRFs; (c) Logarithmic standard deviations

### 3.5 Summary

In chapter 3, three factors were investigated to observe their effect on the seismic demand of the secondary system. The SDOF-SDOF model was numerically analyzed.

- 1) **Dynamic coupling effect:** By performing coupled analysis, FRSs of four mass ratio cases were compared to conventional uncoupled FRS. Up to 55 % reduction, at 5 % mass ratio, in terms of peak spectral acceleration was observed at the tuning frequency.
- 2) **Influence of strong-motion duration:** Total forty-four spectrally equivalent ground motion record triads with different strong-motion durations were used as input. Although the linear-elastic analysis was conducted, duration dependency of the amplification was apparent. Approximately 11 % to 16 % reduction in amplification was expected for the short duration records compared to the longer records.
- 3) **Uncertainty treatment methods:** Two methods used for seismic fragility analysis were applied, following procedures in EPRI guidance (Grant, Hardy and Short, 2018) and ASCE 4-16 (2017). In general, median FRSs of the best estimate, deterministic seismic response analysis, and probabilistic seismic response analysis were alike in spectral shape. However relevant disparities were observed near the tuning frequency. Compared to the best estimate case, which is the result of ‘deterministic’ analysis, peak accelerations of the others were 9 % and 48 % lesser.

## **Chapter 4. Numerical Analysis of Nuclear Power Plant Structures**

### **4.1 Introduction**

In Chapter 4, finite element analysis of an operating nuclear power plant is presented as a case study. Based on the results of Chapter 3, three factors are thoroughly considered in the analysis process. Additionally, spatial variation due to 3-D modeling is carefully incorporated in Section 4.5.

Unlike the previous chapter where the simple SDOF-SDOF model was used, this chapter deals with a more detailed FEM. Modeling is an integral part of the analysis, as it should closely resemble the realistic behavior of the actual building. Hence, the following section begins with modeling the target building.

### 4.2 Modeling of the auxiliary building

Target nuclear power plant is shown in Figure 4-1 (a). In this chapter, an auxiliary building (Aux. Bldg. in Figure 4-1 (b)) is analyzed. The auxiliary building wraps around an RCB. Two buildings share an identical basemat often referred to as a nuclear island, whereas a minimum of 2 in seismic gap separates them above the base. As two buildings are structurally independent, the RCB was reasonably omitted in the following process of modeling.

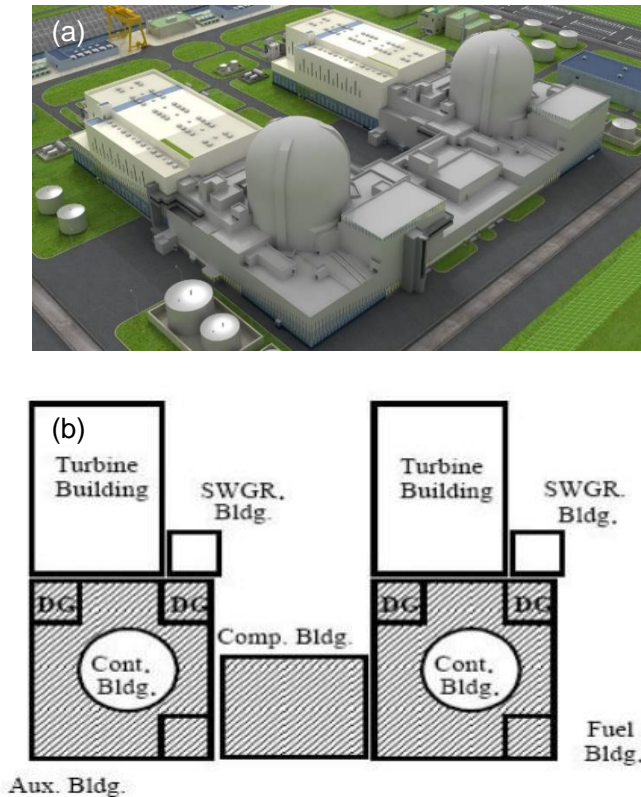


Figure 4-1 Operating nuclear power plant: (a) aeroview; (b) arrangement

(source: KEPCO E&C co.)

### 4.2.1 General

Initially, the geometry of the safety-related AB was rendered via Rhinoceros 3D (2010). At this point, the model merely visualized general geometric data, such as floor elevation, width, and depth of walls. It was imported to Ansys® (2020), where more details were implemented. Cross-sections of columns were included and structural elements were rigidly connected. Then following default model information was prepared. Based on this model, properties such as Young’s modulus and damping ratio were altered for purposes that will be explained later. Most of the building properties are determined based on ASCE/SEI 4-16 (2017) and summarized in Table 4-1.

Table 4-1 Properties of the numerical modeling

Property	Value
Element type	Structural wall: 4-node shell element (Shell181) Column: 3D 2-node beam element (Beam188) Slab: 4-node shell element (Shell181)
Element size	Structural wall: 3 m x 3 m Column: 2 m Slab: 3 m x 3 m
Young’s modulus	29.73 GPa
Boundary condition	Fixed support at the base
Response Level	2
Effective Stiffness	Flexural Rigidity: $0.5 E_c I_g$ Shear Rigidity: $0.5 G_c A_w$ Axial Rigidity: $E_c A_g$
Damping ratio	7%

As the linear elastic time history analysis is performed in the thesis, no

reinforcement bars were considered in the modeling, except for their weight. Young's modulus was calculated based on the 40 MPa compressive strength of concrete, which was applied for the entire model. Equation (4.2) from ACI 318-19 (2019) was used.

$$E_c = 57,000\sqrt{f'_c} \text{ (in psi)} \quad (4.1)$$

$$E_c = 4,700\sqrt{f'_c} \text{ (in MPa)} \quad (4.2)$$

Response level was determined prior to modeling damping and stiffness. Defined in ASCE/SEI 4-16 (2017), concrete walls, beams, and columns have not cracked severely at response level 1. At response level 2, significant cracks propagate through those structural members. In the thesis, response level 2 is chosen, assuming degradation in the stiffness.

ASCE/SEI 4-16 (2017) specifies the effective stiffness of RC structure depending on the element types. For the in-plane response of the cracked shear walls, 50 % of flexural rigidity, shear rigidity, and 100 % axial rigidity are suggested. For the out-of-plane response, 50 % of flexural rigidity and 100 % of shear rigidity; for the columns in compression 70 % of flexural rigidity and 100 % of the shear rigidity and axial rigidity are proposed respectively. In the thesis, these criteria were achieved by adjusting the thickness of elements and two moduli of concrete, based on modeling technique used by Isbiliroglu et al. (2019). The thickness of shell was divided by  $\sqrt{2}$  whereas elasticity modulus was multiplied by  $\sqrt{2}$  for the 100 % axial rigidity and the 50 % out-of-plane flexural rigidity. As the shear rigidities of in-plane and out-of-plane direction differ, orthotropic material was used ( $G_c/\sqrt{2}$  for in-plane direction and  $\sqrt{2} G_c$  for out-of-plane direction).

## Chapter 4. Numerical Analysis of Nuclear Power Plant Structures

---

ASCE/SEI 4-16 (2017) suggests damping value depending on the response level. For reinforced concrete structures, 7 % corresponds to the response level 2. In Regulatory Guide 1.61 (NRC, 2007), damping values are given based on the level of earthquake. 7 % and 4 % of critical damping are assigned for the reinforced concrete members under the safe-shutdown earthquake (SSE) and the operating-basis earthquake (OBE). PGA levels of the SSE and the OBE are 0.3 g and 0.2 g for the auxiliary building. In the following sections, the ground motions of PGA exceeding 0.3 g will be used therefore damping ratio was modeled as 7%. Both guidances also allow, specifically for generating FRS, 4% damping ratio instead of complying with the response level. Though throughout this chapter, otherwise specified, 7 % damping ratio was used.

Generally, SSI analysis is required for safety-related nuclear structures. In Chapter 3, the SSI effect was neglected merely for simplicity. Yet, a fixed-base support assumption still can be made for the FEM when certain conditions are satisfied. Rock foundation, where the SSI effect is minimal, is one condition suggested in ASCE/SEI 4-16 (2017). Previously selected soil profile consists of two layers of soils exceeding shear wave velocity of 1,067 m/s (3,500 ft/s), a criterion defining rock foundation. Therefore, the fixed-base support is a boundary condition.

### 4.2.2 Mesh size for finite element model

A sensitivity test was performed to determine reasonable mesh or element size. Fine mesh does yield results closer to reality yet the number of nodes and consequential computation time increases exponentially. Element size parameter was varied from 1.0 m to 3.0 m. Figure 4-2 presents five models with different sizes of mesh. Corresponding numbers of nodes and elements are summarized in Table 4-2.

Table 4-2 Summary of models with different mesh sizes

No.	1	2	3	4	5
Mesh Size	3.0 m	2.5 m	2.0 m	1.5 m	1.0 m
Number of nodes	22,506	27,397	38,052	60,973	124,322
Number of elements	26,567	31,426	42,496	66,304	131,363

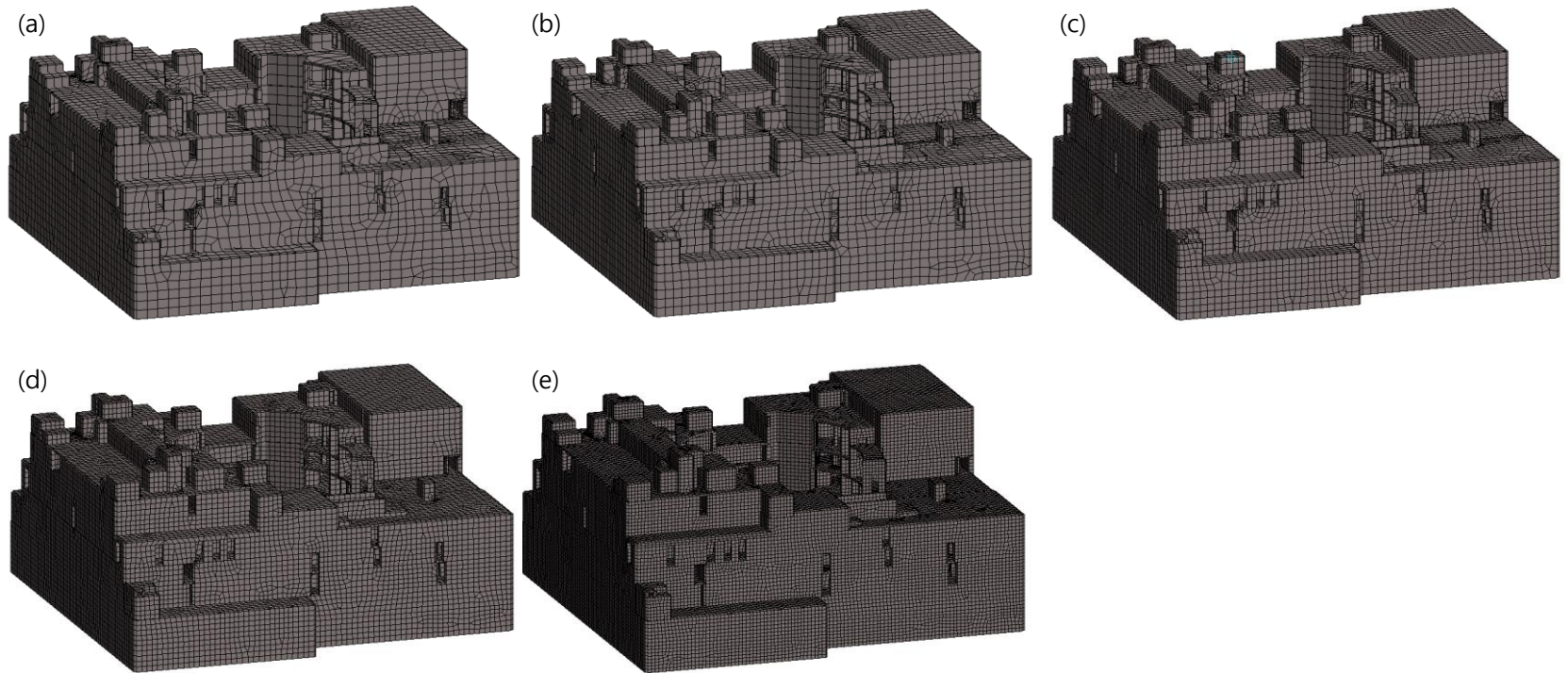


Figure 4-2 Models with different mesh sizes: (a) 3 m; (b) 2.5 m; (c) 2 m; (d) 1.5 m; (e) 1 m

Modal analyses were performed subsequently to compare natural frequencies. In total 1,000 modes were obtained by the Block Lanczos method in Ansys®. Plotted in Figure 4-3 represent cumulative mass ratios for the five models. For two horizontal directions, the difference between the five lines is hardly noticeable, whereas a slight disparity is apparent in the vertical direction. It is subtle yet noticeable that the finer models tend to shift left downward. This is expected because as the geometries are finely divided stiffness decreases eventually yielding greater modal frequencies. By the same logic, more mass is lumped into the larger element. This is especially prominent in the vertical direction where local out-of-plane floor modes contribute a large fraction.

The above results matched well with a technical report by KEPCO & KHNP (2013). In the report, models with two different mesh sizes, namely fine and coarse were compared. Each model used mesh sizes of 1.52 m (5 ft) and 3.66 m (12 ft) then modal analysis results, static displacements, and FRS were compared. In conclusion, the dynamic properties of the two models were adequately close. Two models also agreed well for comparisons of statics displacements and FRS, successfully validating that the coarse model yields sufficiently accurate results.

Hereafter, the mesh size of 3.0 m was chosen for generating the finite element model (FEM) of the AB. Based on the sensitivity analysis, the dynamic properties of the 3.0 m mesh model were not remote from those of the 1.0 m mesh model. According to KEPCO & KHNP (2013), the coarse model is accurate in not only the dynamic properties but also in static displacements and FRS. Therefore, it can be inferred that 3.0 m mesh size would be accurate enough while computational cost is economical.

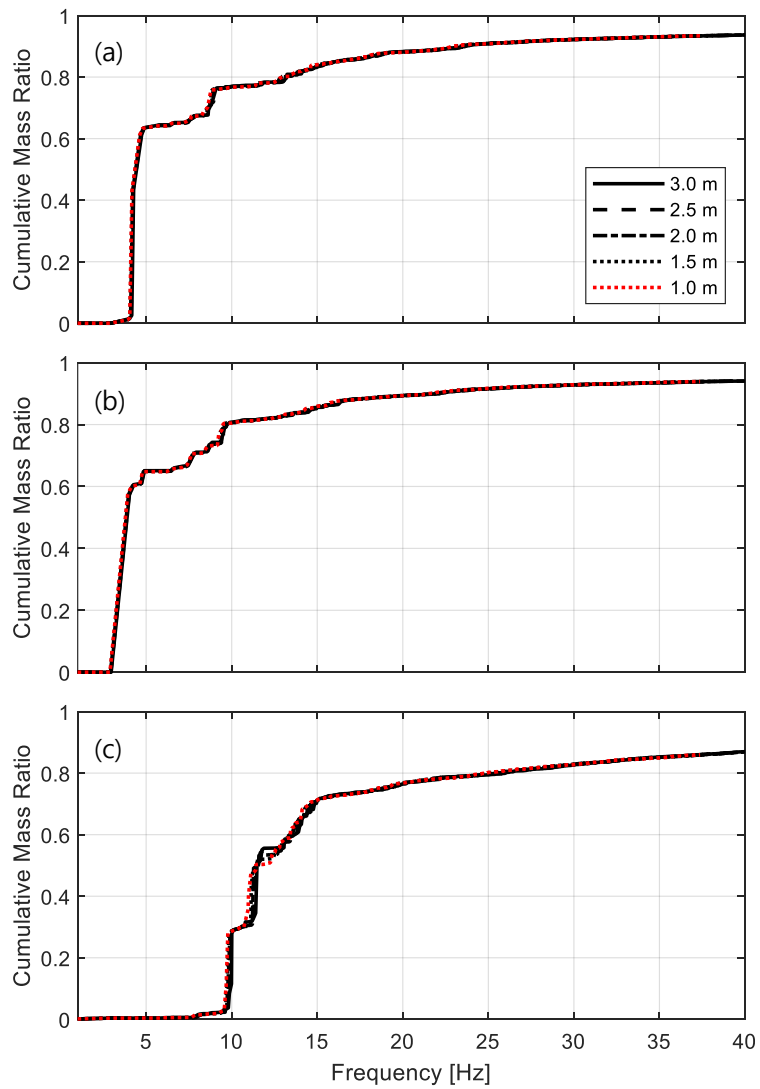


Figure 4-3 Cumulative mass ratios comparison between different mesh sizes:

(a) X (EW) direction; (b) Y (NS) direction; (c) Z (Vertical) direction

### 4.2.3 Other Assumptions

#### Opening dimensions

Architectural drawings with specific dimensions were unavailable. The widths of doors and openings were estimated from equipment arrangement drawings. Distances between walls were measured and scaled. However, this method is inapplicable for height, because elevation drawings show limited numbers of the openings at the same elevation. Therefore, opening heights were assumed to be the same as wall heights. Due to the deficit section, the overall stiffness of the structure may decrease, yet its magnitude was expected to be trivial.

### 4.3 Dynamic coupling effect

In this section, the dynamic coupling effect was investigated for the AB model. Direct time history analysis of the coupled system as in Section 3.2 would be exact, yet the process is computationally demanding for the FEM. Hence in this section frequency domain analysis reviewed in Section 2.1 was applied.

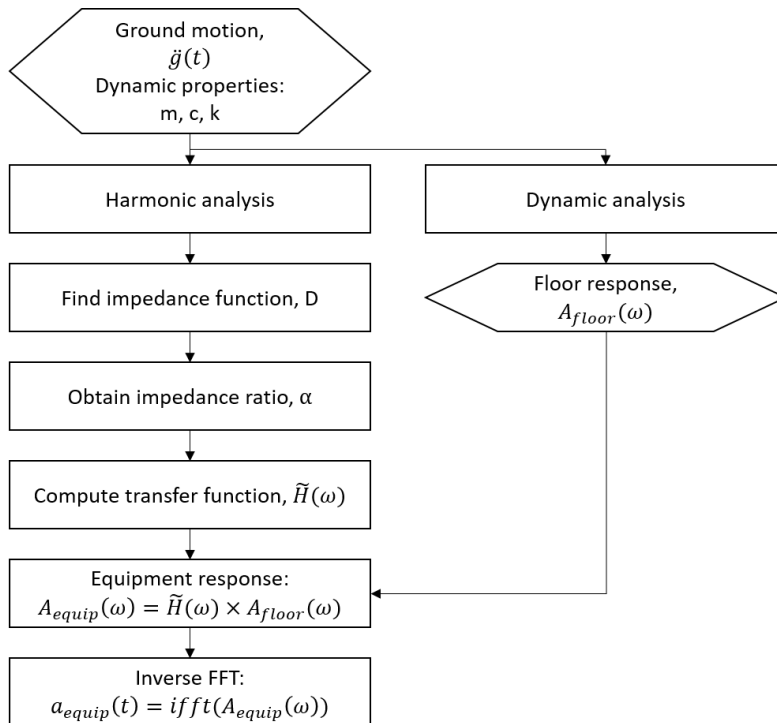


Figure 4-4 Process of frequency domain analysis

Though briefly covered in Chapter 2, the overall process is more specifically

## Chapter 4 Numerical Analysis of Nuclear Power Plant Structures

---

expressed in a flowchart shown above. Figure 4-4 is based on EPRI (Ostadan, 2017) and Choi and Lee (2005). Initially, dynamic analysis is performed to obtain the floor response of the equipment support. Then the harmonic analysis is proceeded to find the impedance function of the equipment support. Consecutively the impedance ratio and the transfer function are computed. Multiplying the transfer function and Fourier transform of the floor acceleration gives the Fourier transformed equipment acceleration. Finally, inverse Fourier transform yields the equipment acceleration time history. The harmonic analysis and the dynamic analysis were performed via Ansys<sup>®</sup> and the following steps were post-processed by MATLAB (2021).

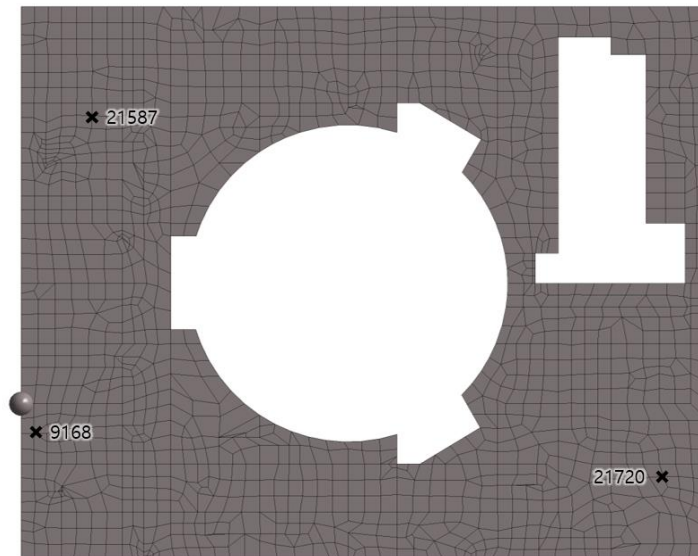


Figure 4-5 Node locations and IDs at EL. 137.5 ft floor

## **Chapter 4. Numerical Analysis of Nuclear Power Plant Structures**

---

The nodes shown in the Figure 4-5 were investigated in this section. Three locations on elevation 137.5 ft floor, where electrical equipment is installed, were selected.

FEM corresponding to response level 2 was analyzed. During the harmonic analysis, the nodal harmonic force was applied for the direction of interest and the complex displacement frequency response function for the respective direction was obtained. This was repeated for three directions.

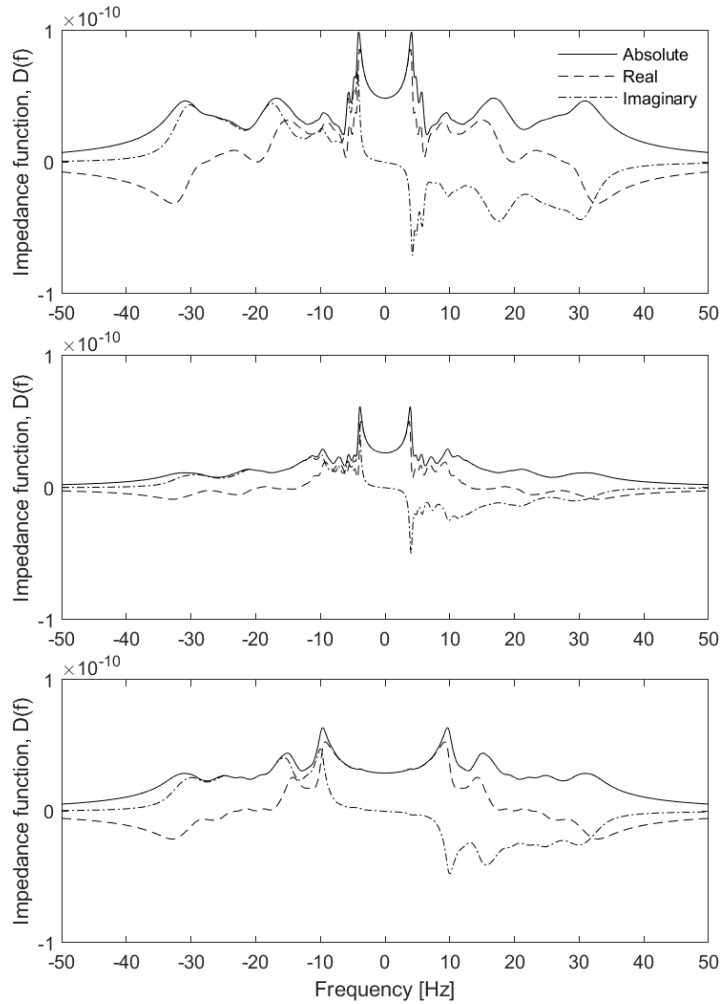


Figure 4-6 Impedance functions of Node 9168: X dir. (top); Y dir. (middle); Z dir. (bottom)

For illustration, Figure 4-6 shows impedance functions for X (top), Y (middle), Z (bottom) direction, at Node 9168. For each direction, both real and imaginary parts together with absolute function were plotted. For the given harmonic force, the largest displacement is expected at the tuning frequency. This is expressed as peaks at the impedance functions.

Calculated the impedance functions, the complex transfer functions were then computed. By varying the damping ratio and mass of the equipment, the impedance ratio  $\alpha_e(\omega)$  changes and successively the transfer functions. For the dynamic analysis of the structure, the first ground motion of Table 3-4 was used. At each node, tri-directional floor acceleration time histories were acquired then a fast Fourier transform (FFT) was used.

In Section 3.2 mass ratio was calculated as secondary system mass to primary system mass, because both systems were SDOF. As mentioned in Section 2.1, this procedure assumes SDOF equipment and slab. Therefore, the equipment was reasonably modeled as SDOF. The slab, on the other hand, is the MDOF system in the FEM. In order to follow the assumption made in the method, the mass ratio was defined as the secondary system mass to the first modal mass of the primary system, on the direction of interest.

Figure 4-7 shows the comparison of FRS for different mass ratios defined as above. For each direction, the mass of the first mode was designated as a denominator of the mass ratio. Mass of the equipment was then calculated accordingly to render the mass ratios of 0.1, 0.5, 1.0, and 5.0 percent. The top figure is similar to Figure 3-3. Compared to the uncoupled FRS (grey solid line), ESI considered FRS (red lines) exhibit lesser amplitude near the natural frequencies of the structure. When the mass ratio is five percent, as much as forty percent reduction was made for X-direction spectral acceleration.

This observation coincides with the expectation that can be made from (2.14). The absolute value of the complex transfer function in resonance can be written as,

$$|\tilde{H}(\omega = \omega_e)| = \frac{\sqrt{(\alpha_e - 4\beta_e^2)^2 + 4\beta_e^2(1 + \alpha_e^2)}}{\alpha_e^2 + 4\beta_e^2} \quad (4.3)$$

For small damping ratio, higher-order terms can be neglected and (4.3) reduces to,

$$|\tilde{H}(\omega = \omega_e)| \cong \frac{1}{\alpha_e} \quad (4.4)$$

Equation (4.4) in combination with (2.13) gives,

$$|\tilde{H}(\omega = \omega_e)| \cong \frac{D_s(\omega_e)}{m_e \omega_e^2 (1 + 2i\beta_e)} \quad (4.5)$$

The impedance function of the support in the numerator is a definite value. The denominator is composed of three dynamic properties of the equipment, mass, natural frequency, and damping ratio. As the mass increases, the absolute value of the transfer function decreases, eventually resulting in a lesser equipment response.

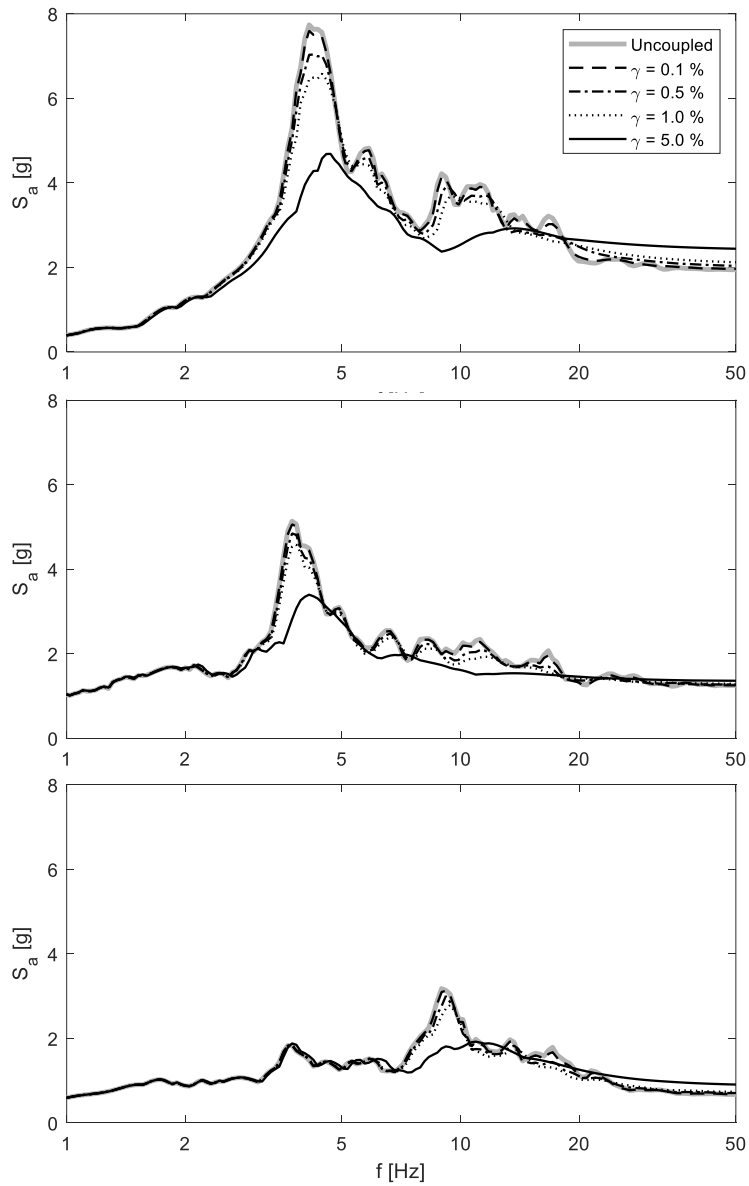


Figure 4-7 Comparison of FRS at Node 9168 for different mass ratios: X dir. (top); Y dir. (middle); Z dir. (bottom)

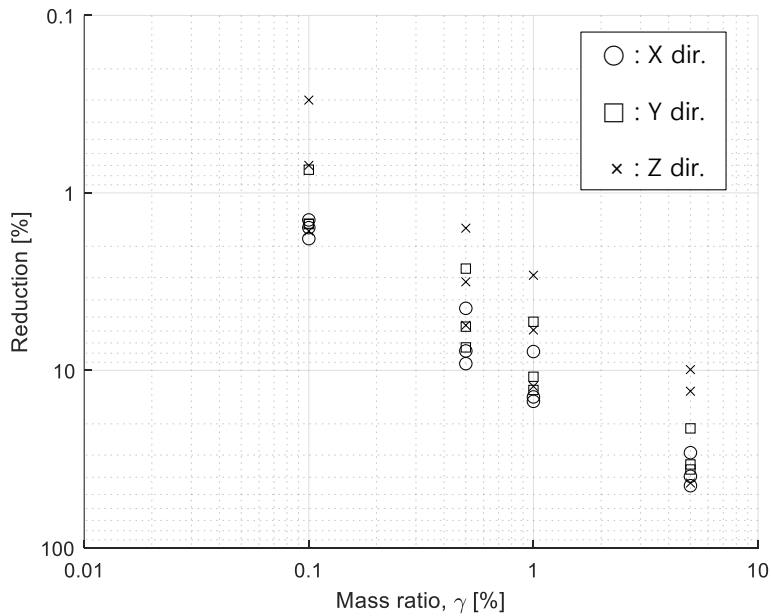


Figure 4-8 Peak reduction vs. mass ratio

For better visualization, peak reduction values of four mass ratios for three nodes can be plotted as Figure 4-8. Tri-directional values were plotted together on a log-log scale, where abscissa is the mass ratio and ordinate is the reduction relative to the uncoupled spectral acceleration. Noticeably the reduction increases proportionate to the mass ratio. Since a limited number of nodal results was studied, it is impossible to derive concrete tendencies between each direction. Though it was observed that the reduction values of Z-direction were lesser than values reported in EPRI technical report (Ostadan, 2017). At the mass ratio of 0.5 %, approximately 34 % peak reduction was presented in an example from the report. One possible reasoning, which is also mentioned in the report, is the interplay of the higher modes. In the FEM, over ten densely spaced modes participate for the given support location. Compared to the case

study in the report where a single vertical mode was considered, the modal mass is expected to be higher and the response may have been amplified.

However, a critical problem was found in the result. Such mass ratio is very rare as the first modal masses of the supporting structure are large. According to modal analysis, the first modal masses for each direction are 94,787 tons, 131,999 tons, and 40,511 tons. Compared to the floor mass, for example, 9,823 tons for the EL.137.5 ft floor, the horizontal modal masses are approximately ten times and the vertical modal masses are four times greater. This is because the first mode shapes are global and more than one floors participate. Consequently, one percent mass ratios are equivalent to 947 tons, 1319 tons, and 405 tons for each direction.

Equipment weighing around the aforementioned magnitudes is scarce in the AB. Heavy equipment such as polar crane, steam generator, turbine is installed in other buildings, the RCB and turbine building respectively. One of the most massive components in the AB, the emergency diesel generator (EDG) weighs approximately 140 tons. For the EDG the reductions in the horizontal seismic demands are expected to be minimal. The vertical demand may decrease, nonetheless, it should be noted that it depends on the support location.

In conclusion, the effect of dynamic coupling was studied via frequency domain analysis in this section. As previously discussed with the simple model, a similar trend where the peak amplitude reduces for heavier equipment was confirmed. Despite the guaranteed reduction, the absolute weight for the equipment to show a meaningful decrease is limited. In other words, the dynamic coupling effect for the majority of the equipment would be trivial.

### 4.4 Influence of strong-motion duration

In this section, the same procedure as in Section 3.3 was repeated. Total forty-four sets of earthquake records summarized in Appendix A were used. Uni-directional time histories were applied to the longitudinal direction of the model. Scaled PGAs of the records varied from 0.07 to 1.91 g and the majority were below SSE PGA which is 0.3 g for the target NPP. Response level 1 was specified for convenience and uniformity of the analysis. Therefore, a corresponding damping ratio of 4 % and full effective stiffness were applied to the model.

Eleven locations were investigated. As shown in Figure 4-9 five nodes sharing identical planar coordinates (X and Y coordinates) with different elevations – 100 ft, 120 ft, 137.5 ft, 156 ft, 172 ft – and six nodes at 156 ft elevation were additionally selected.

X directional acceleration time histories were acquired at each location and amplification spectra were generated. Figure 4-10 shows the mean amplification spectra at eleven nodes. Compared to Figure 3-6, FEM results were consistent in that the long duration records yield greater amplification than the medium and short duration records. Also at several nodes (1908, 10243, 10277, 21521), the same trend was observed near the second peak around 13 Hz. Out of that range, no significant difference was observed.

As spectra comparison coincided with the result drawn in Section 3.3, individual records were plotted at the tuning frequency, 6.00 Hz, to investigate correlation. Equation (3.6) based on regression lines were added in Figure 4-11.

## Chapter 4. Numerical Analysis of Nuclear Power Plant Structures

Regression lines derived at eleven nodes followed a similar tendency shown in the SDOF-SDOF model. There are two observations that differ from Section 3.3. One is that magnitude of the regression line was lesser. In other words, amplification values were smaller globally. For instance, intercept or amplification at  $D_{5-75}/T = 2$  is around 7 in Figure 3-7.

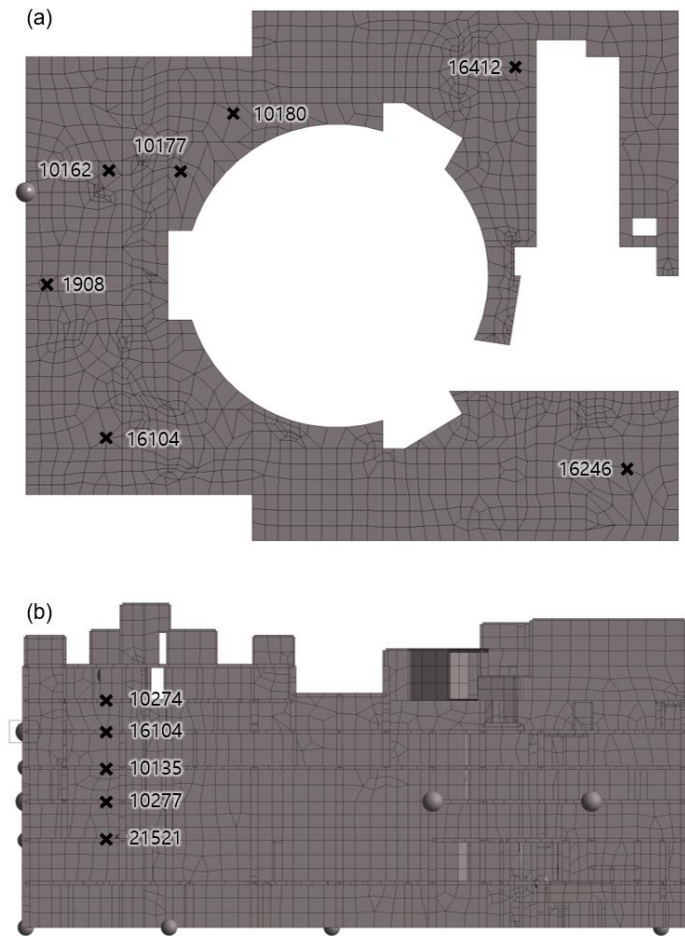


Figure 4-9 Node locations and IDs: (a) seven nodes at 156 ft floor; (b) four additional nodes at different elevations

## Chapter 4 Numerical Analysis of Nuclear Power Plant Structures

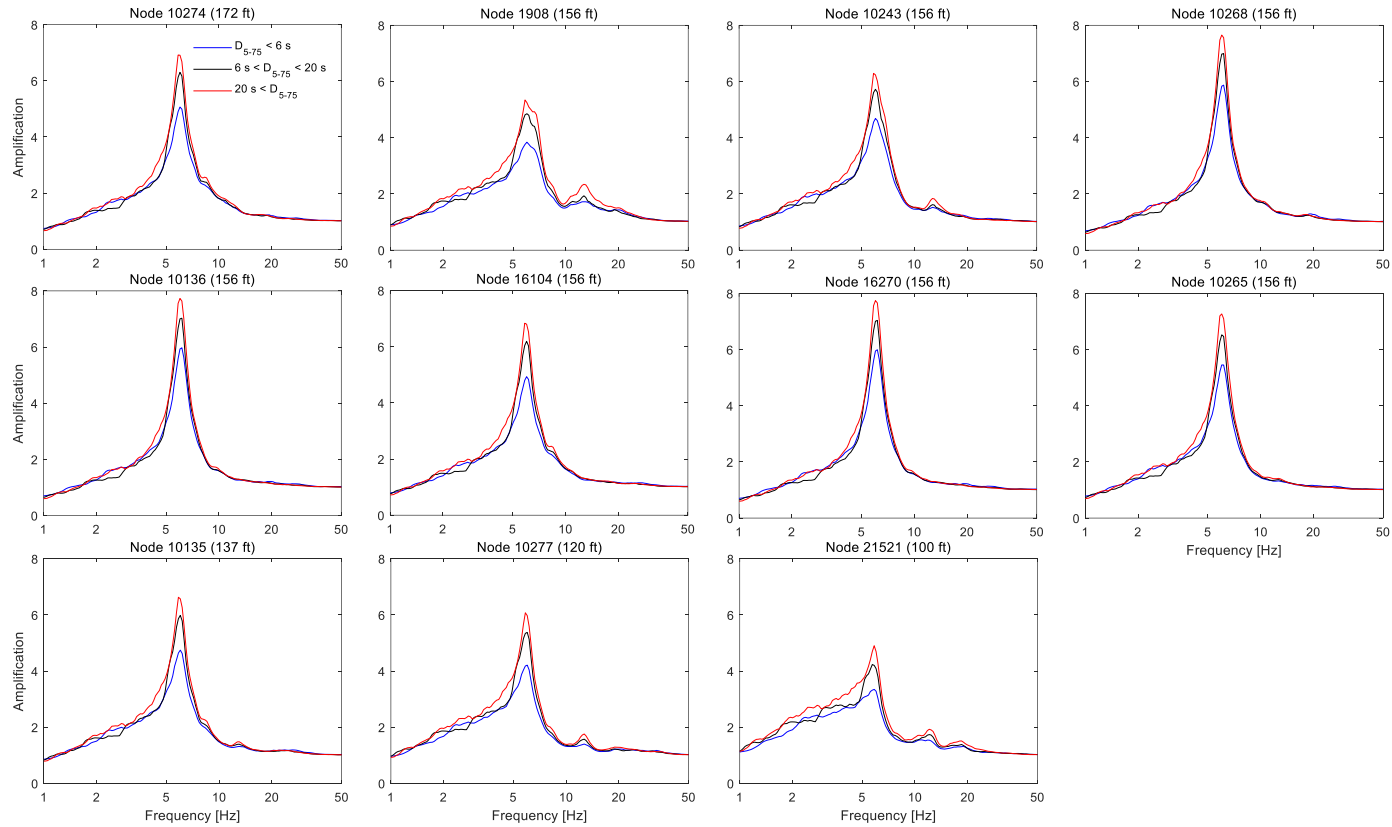


Figure 4-10 Mean amplification spectra at eleven nodes

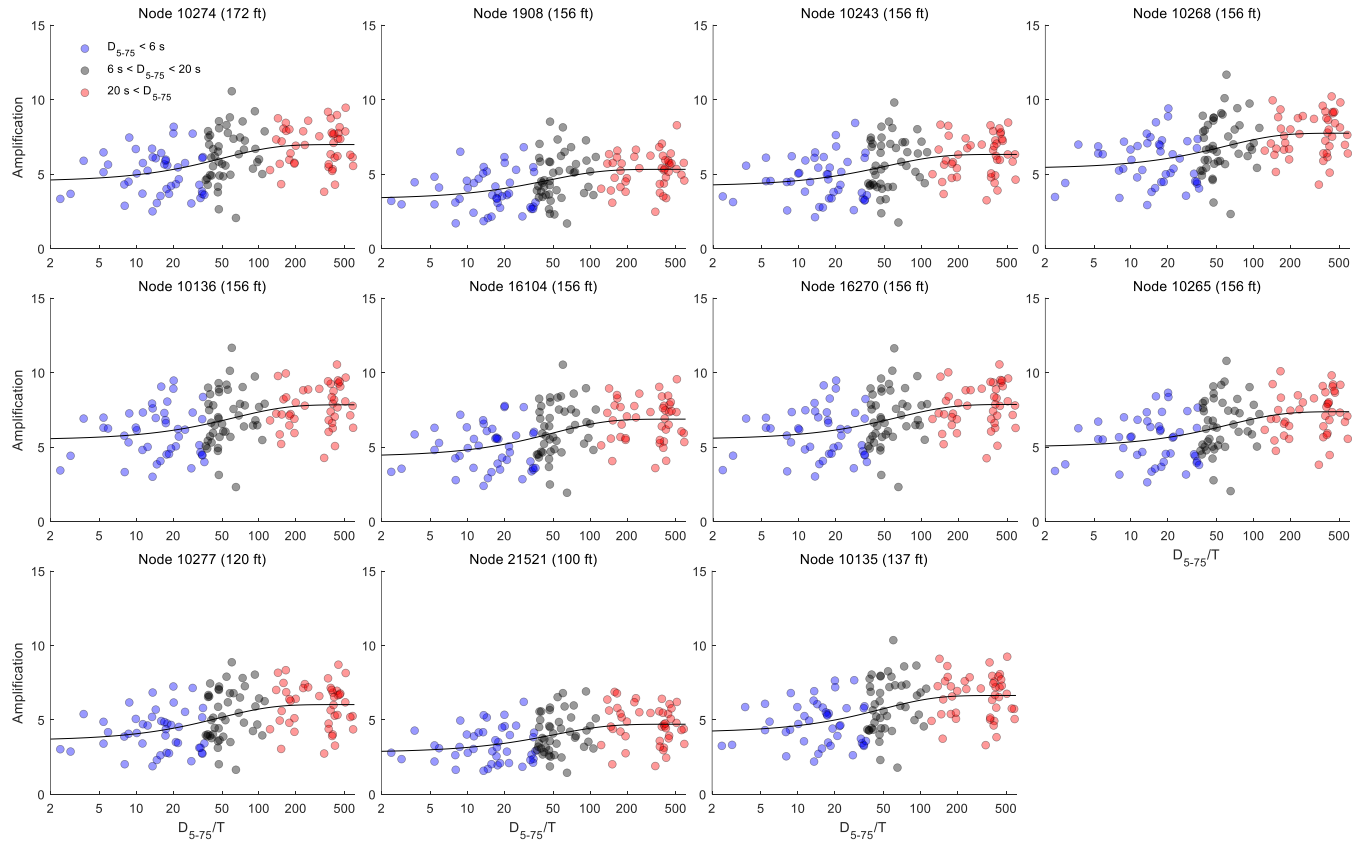


Figure 4-11 Amplification vs.  $D_{5-75}/T$  plots at eleven nodes

On the other hand, all regression lines from the FEA were below 7 at the same abscissa. Recalling that the previous results were obtained from the simple model, it can be inferred that the reduction in amplification may have resulted from higher modes participation.

Another inspection is a delayed plateau of the regression lines. It is apparent in Figure 3-7 plateau begins at the medium duration records, whereas in the case of FEA the regression lines continue to increase in the same range. This implies greater amplification expected beyond  $D_{5-75} = 20$  s which was also depicted in the mean amplification spectra.

Based on fitted regression line amplification reduction was estimated. As Figure 3-7, amplifications corresponding to the strong-motion duration of 6 s and the Gyeongju earthquake were compared. Table 4-3 shows a decrease rate ranging from 11.6 % to 19.4 %. Despite some extent of variance, the amount of decrease was close to that of the simple model. The average of eleven nodes was 16 % whereas the SDOF-SDOF case was 15 %.

To separate frequency content, short-duration records were normalized by medium duration records and long duration records within every triad. Both  $D_{5-75}$  and amplification parameters were normalized as shown in Figure 4-12. On log-log scale, linear regression lines were fitted to the records exhibiting a weak, yet the positive correlation between two normalized parameters.

Table 4-3 Amplification decrease estimation for Gyeongju earthquake

Node	Amplification		Reduction [%]
	SRP 3.7.1	Gyeongju EQ	
10274	4.83	5.76	16.21
1908	3.62	4.41	18.03
10243	4.47	5.26	15.08
10268	5.64	6.46	12.67
10136	5.74	6.51	11.88
16104	4.69	5.64	16.94
16270	5.76	6.52	11.57
10265	5.25	6.04	13.01
10277	3.94	4.89	19.41
21521	3.05	3.76	18.87
10135	4.48	5.45	17.75

For instance, the fitted line of Node 10274 gives an amplification ratio of 0.83 at a  $D_{5-75}$  ratio of 0.5, in other words, a ground motion with the strong-motion duration half of that of the another estimates a 17 percent less amplification on average. It should be noted that the amplification ratio at  $D_{5-75}$  ratio of one is not unity due to other factors besides strong-motion duration. Hence, the amplification ratio at the given  $D_{5-75}$  ratio was normalized by that of the unity  $D_{5-75}$  ratio and summarized in Table 4-4.

## Chapter 4 Numerical Analysis of Nuclear Power Plant Structures

Table 4-4 Amplification ratio and decrement estimation

Node	Amplification ratio				Reduction [%]		
	$D_{5-75}$ ratio	1.0	0.5	0.2	0.1	0.5	0.2
10274	0.87	0.83	0.78	0.74	4.75	10.69	14.93
1908	0.87	0.83	0.78	0.74	4.81	10.82	15.11
10243	0.90	0.86	0.81	0.77	4.42	9.96	13.94
10268	0.91	0.87	0.82	0.79	4.31	9.72	13.61
10136	0.92	0.88	0.83	0.79	4.63	10.42	14.57
16104	0.87	0.83	0.78	0.75	4.59	10.34	14.45
16270	0.93	0.88	0.83	0.79	4.60	10.37	14.49
10265	0.92	0.87	0.82	0.78	4.87	10.94	15.27
10277	0.87	0.82	0.77	0.73	5.25	11.76	16.39
21521	0.88	0.84	0.78	0.73	5.51	12.32	17.15
10135	0.87	0.83	0.78	0.74	4.75	10.69	14.93

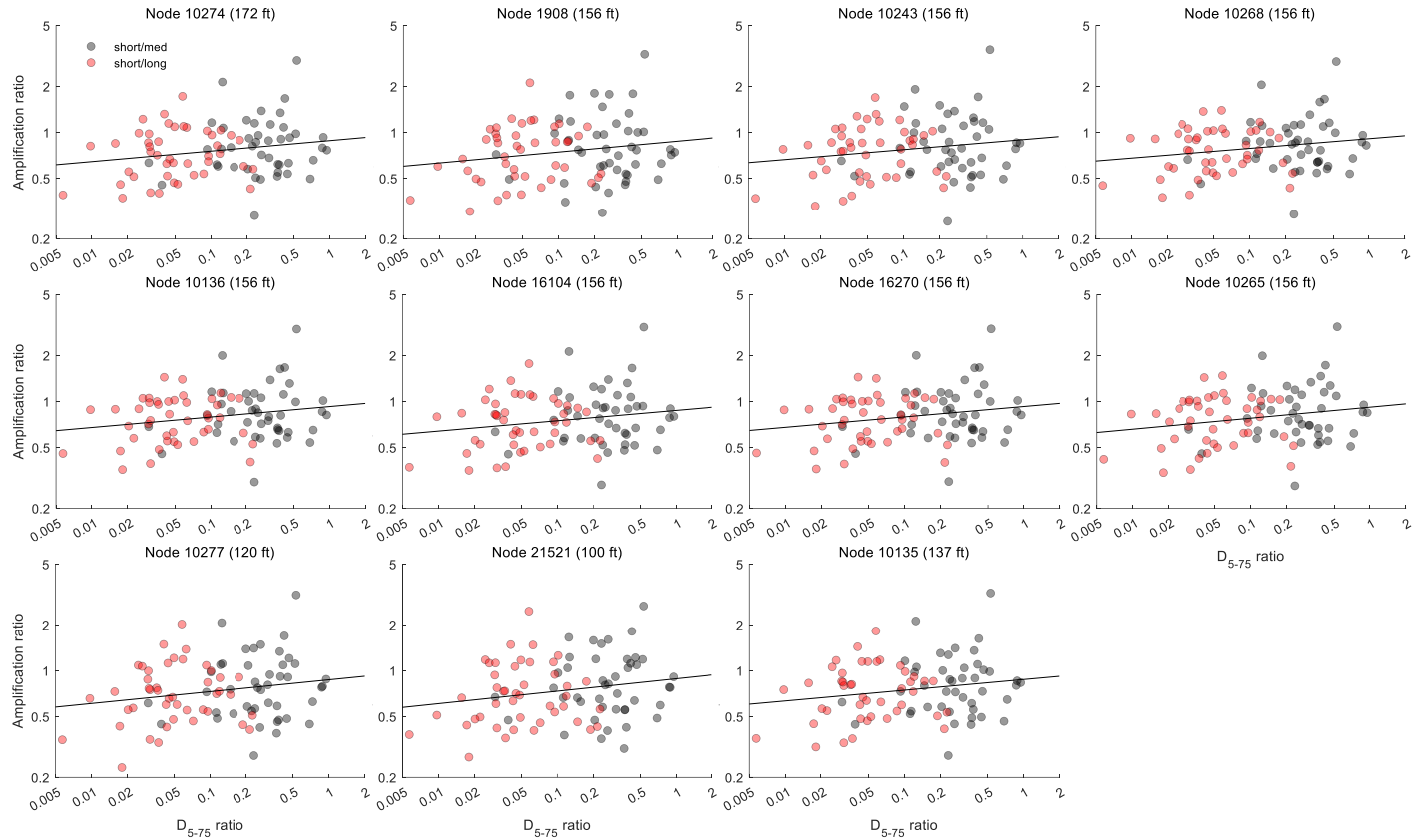


Figure 4-12 Amplification ratio vs.  $D_{5-75}$  ratio plot for eleven node

### 4.5 Spatial variation

In this section, a concern that arises from using 3-D FEM is discussed. It is the spatial variation as reviewed in Section 2.3. Damolini, El-Bahey, and Oikonomou (2019) reported that the average horizontal responses of FEM agree with those of LMSM. However, depending on the building geometry it will be investigated in this section that the horizontal peak spectral accelerations do vary and it would be inappropriate to replace them with the LMSM result.

EL. 137.5 ft floor was investigated as a representative floor. For the input, the first ground motion of Table 3-4 was used. Figure 4-13 shows the plan drawing of the floor and corresponding nodes. At each node, tri-directional FRS were generated for a damping ratio of five percent, which is the median damping ratio of electrical equipment (Grant, Hardy, and Short, 2018). Total 1,551 FRSs are presented in Figure 4-14 for each direction, and two statistics, arithmetic mean and mean plus one-standard deviation FRS are added. Grey lines indicating individual FRS show wide variances from the average FRS. For two horizontal directions (Figure 4-14 (a), (b)), variations were found near natural frequencies. For instance, at 4.23 Hz the maximum and minimum X-directional spectral accelerations are 169 % and 56 % of the mean acceleration. In the case of the vertical direction (Figure 4-14 (c)), the deviation is even greater. The grey lines are way above the mean FRS and using this for the seismic demand could lead to severe underestimation.

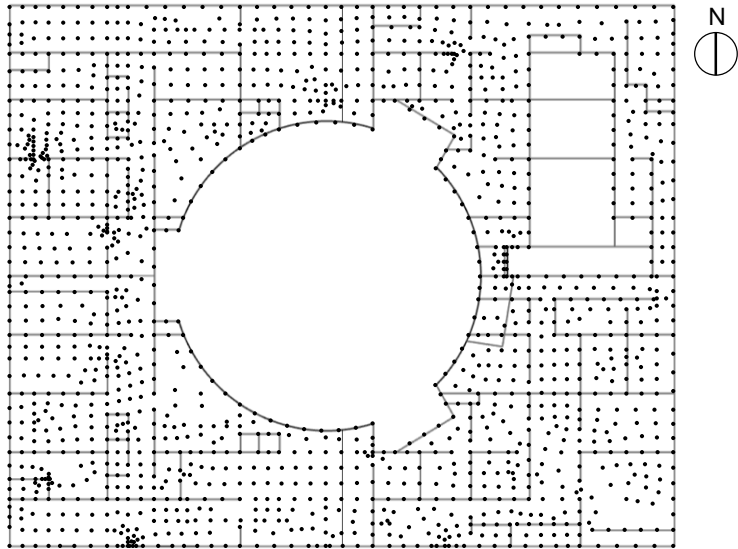


Figure 4-13 EL. 137.5 ft floor plan and nodes

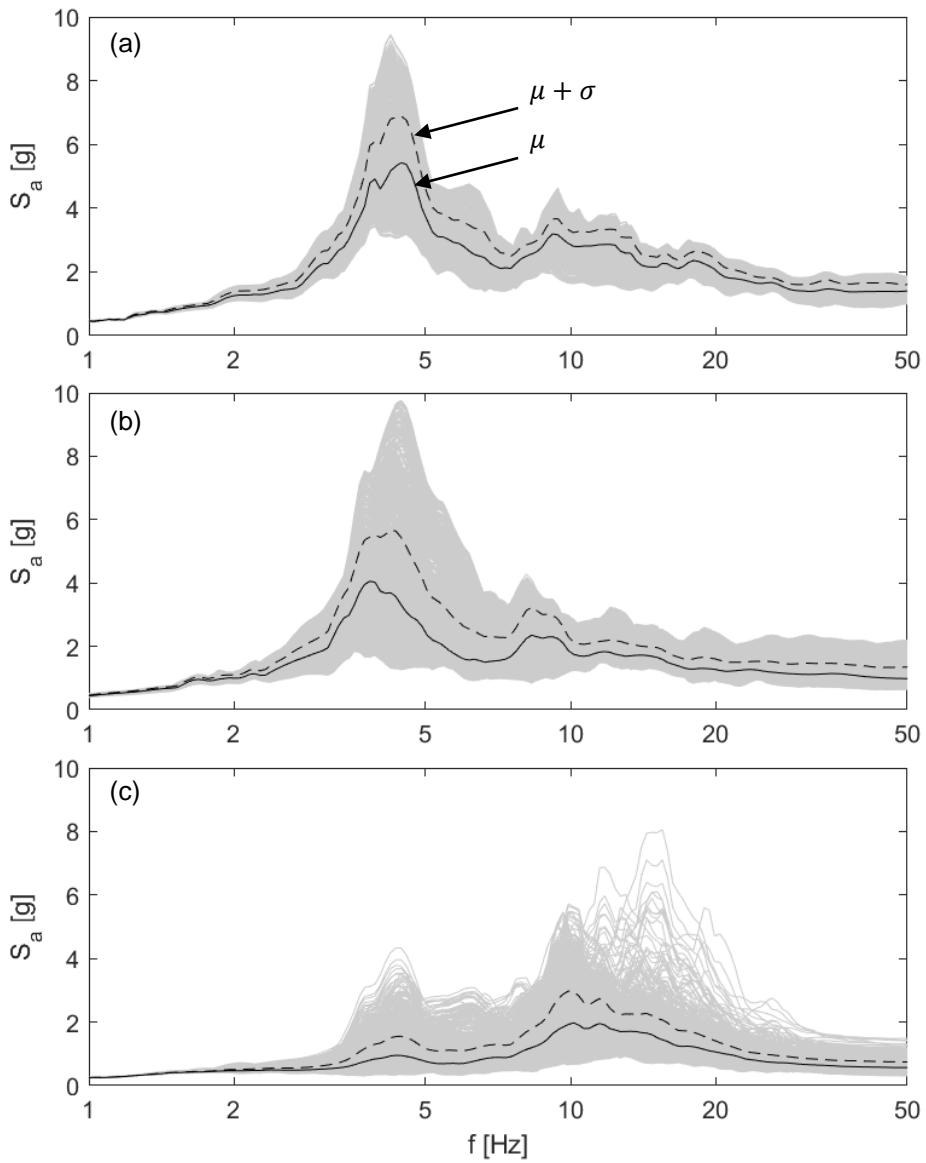


Figure 4-14 FRS of EL. 137.5 ft floor: (a) X direction; (b) Y direction; (c) Z direction

Figure 4-14 successfully shows that significant variations exist within a single floor, yet leaves out spatial information of each FRS. Plotted in Figure

4-15 are spectral accelerations at major mode frequencies, distributed along with nodal coordinates. A global trend of the two horizontal directions is apparent. The X directional spectral accelerations grow greater as Y coordinates of the corresponding nodes are closer to the center of the opening. The very same tendency was observed for the Y direction. The spectral accelerations of the nodes, where X coordinates were closer to the center of the opening, were larger. This may be primarily due to the existence of the opening. In ordinary buildings, the rigid diaphragm assumption is reasonable partially because the area of openings, such as elevator shaft and staircase, is insignificant. However, as shown in Figure 4-13, in the case of the auxiliary building the opening area is lumped at the center and it comprises nearly 19 % of the gross floor area. Hence, a decrease in slab in-plane stiffness near the opening area is expected. The stiffness of walls is also decreased. The opening separates the walls into two parts, whereas those near the perimeters are continuous, resisting as a whole.

The response distribution of vertical direction is somewhat different. Unlike the horizontal responses, the scatter plot seems chaotic at a glance. In plan view a pattern is evident. Figure 4-16 shows two exemplary plots of vertical acceleration distributions. Both represent local slab modes where the upper figure is at 10.14 Hz and the lower is at 14.75 Hz. Apparently, slabs at different locations are excited. At the former frequency, the left side especially the northwest and southwest parts were greatly excited. In the case of the latter frequency, the perimeter of the opening area exhibited high spectral accelerations, and the southeast part locally resonated.

Slab thickness is equally set as 0.6 m for the entire elevation. So one

candidate to explain this is the boundary condition. The auxiliary building is divided into a number of diverse rooms for distinctive functions. Although there exist grid lines that form the basis of shear walls, each floor is differently spaced. The floor of widely spaced rooms is expected to be more flexible. However, walls and columns below and above the floor should be considered simultaneously. In Figure 4-16 (a), large spectral accelerations were found at nodes where walls and floors intersect. This was possible because those walls were not continued below the slab. Due to such geometric complexity, slab flexibilities have wide variation. It was inferable from Figure 4-3 (c) that multiple local modes are summing up a substantial portion. This was then indirectly exhibited in Figure 4-14 (c) with numerous peaks within the range between 10 Hz and 20 Hz.

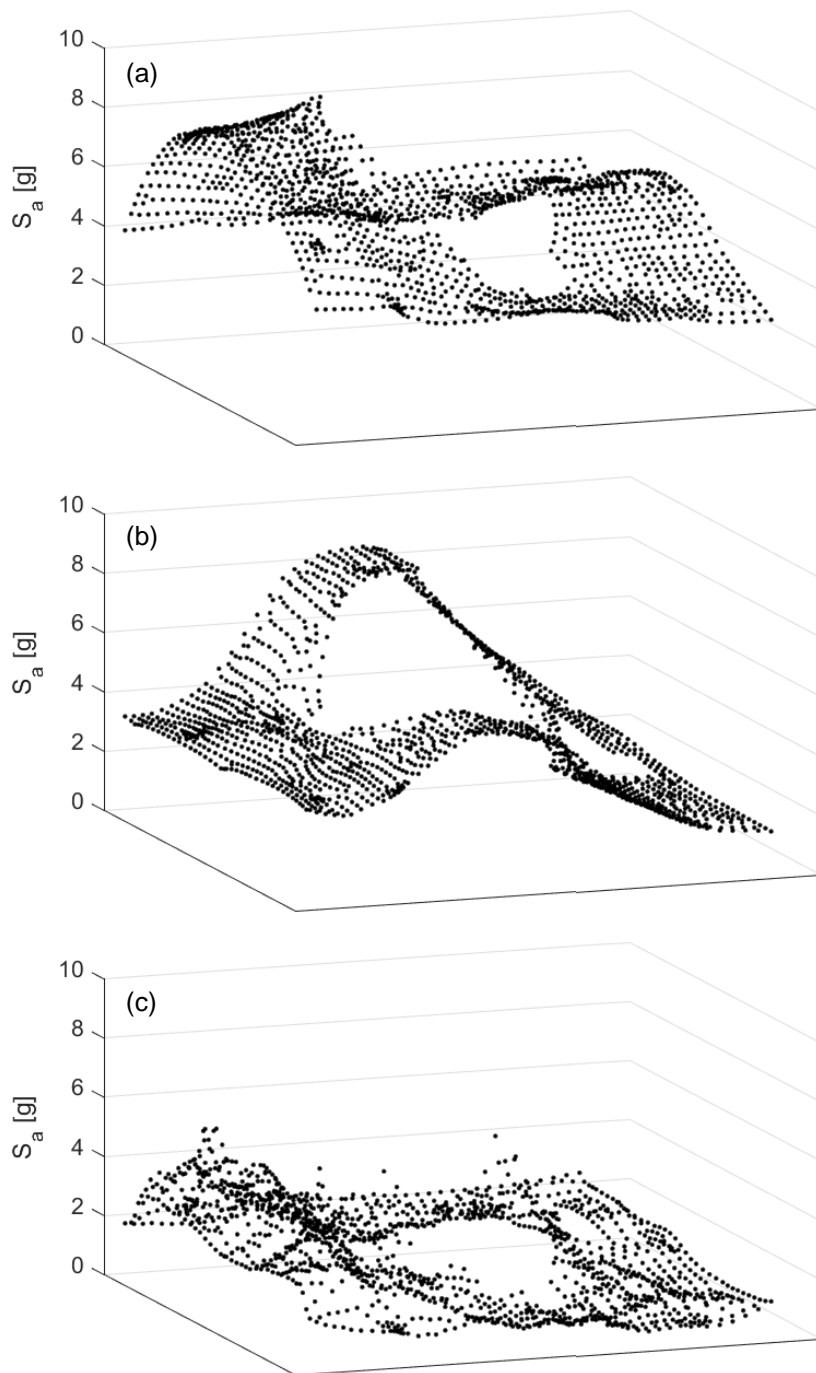


Figure 4-15 Spatial distributions of spectral accelerations: (a) X direction; (b) Y direction; (c) Z direction

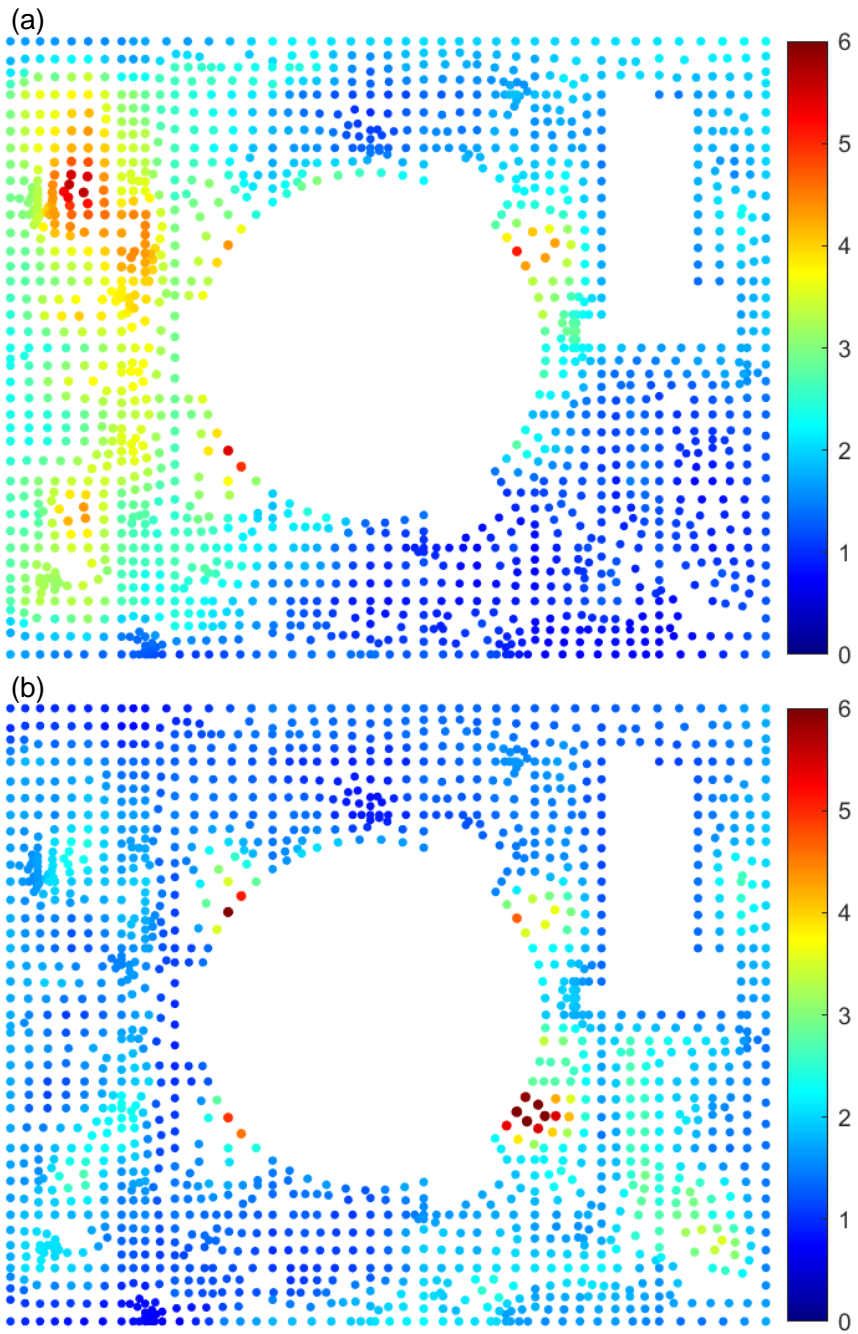


Figure 4-16 Vertical spectral acceleration distributions at: (a) 10.14 Hz; (b)

14.75 Hz

## Chapter 4. Numerical Analysis of Nuclear Power Plant Structures

Based on this result, using the LSM or averaged FRS from the FEM for estimating the seismic demand of the secondary system may lead to unrealistic results.

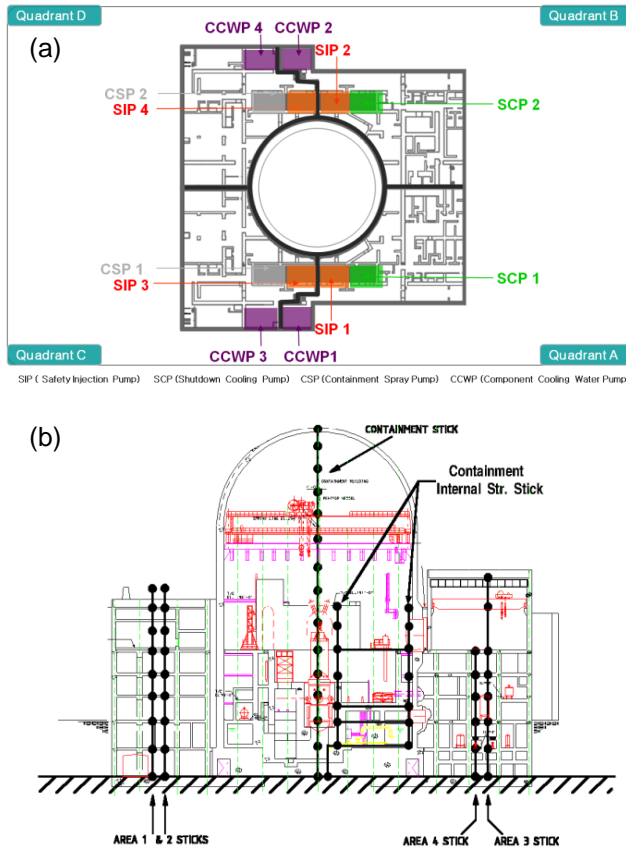


Figure 4-17 Auxiliary building separation: (a) Quadrants; (b) Corresponding LMSMs (KEPCO E&C, 2020, 2010)

The auxiliary building is separated into four quadrants in order to provide a barrier (KEPCO E&C, 2020). As shown in Figure 4-17 (b), four sticks are modeled for each quadrant. This may reduce the variation of responses as the

## Chapter 4 Numerical Analysis of Nuclear Power Plant Structures

area covered by each stick is quartered. Yet Figure 4-15 forecasts that the deviation would still be significant. In the case of the two horizontal directions, the largest accelerations tend to occur near intersections of the quadrants. In the case of the vertical direction, the area where the variation is localized tends to be smaller than the quartered floor area.

This was examined in the following figures: Figure 4-18, Figure 4-19, Figure 4-20.

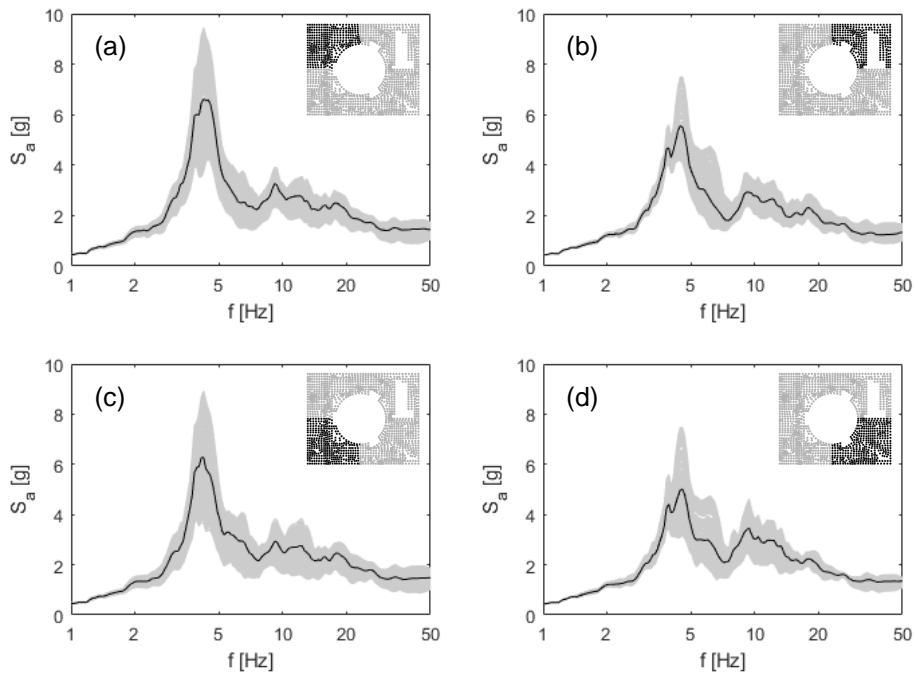


Figure 4-18 X direction FRS at four quadrants

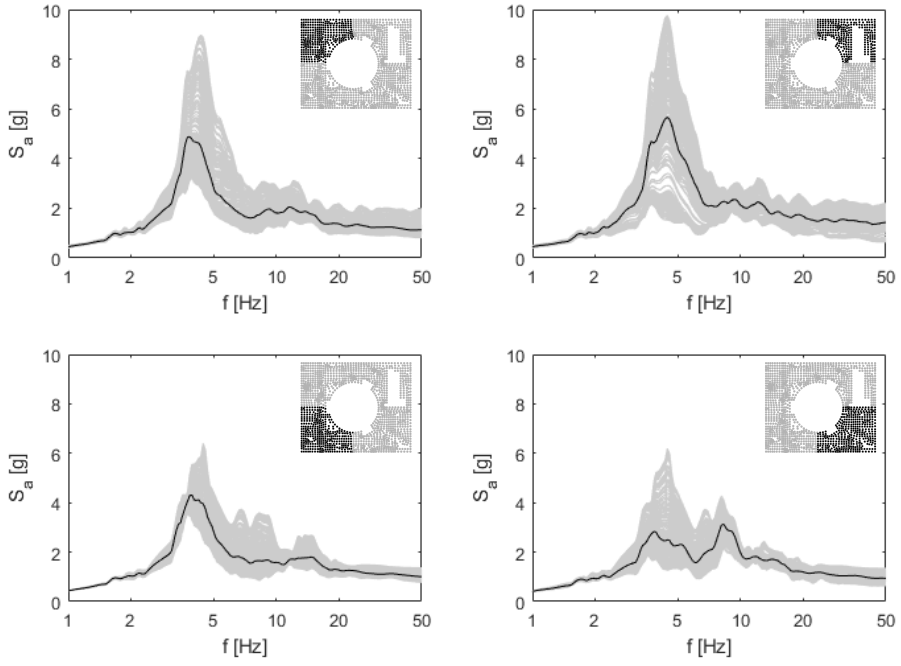


Figure 4-19 Y direction FRS at four quadrants

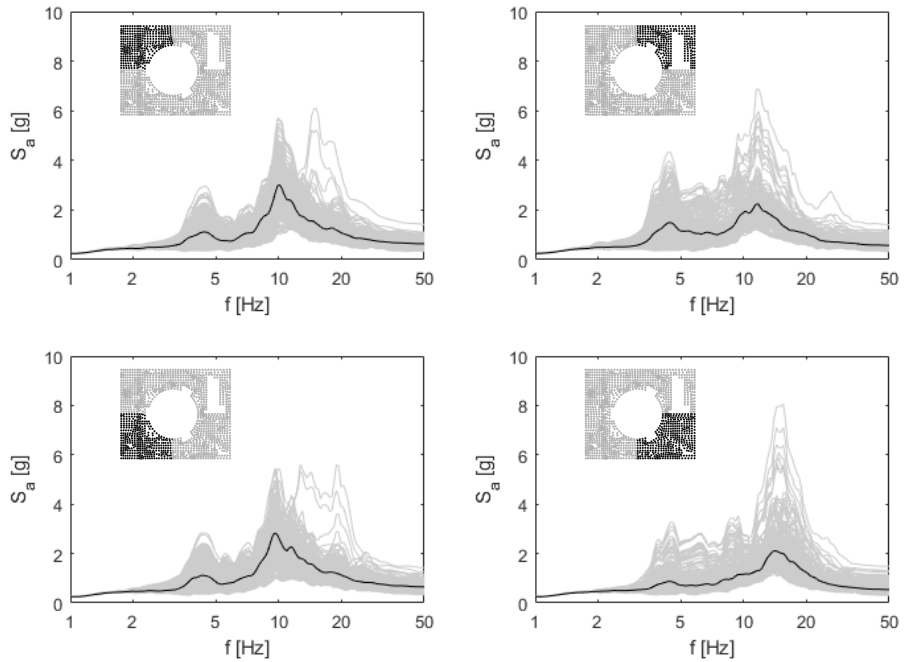


Figure 4-20 Z direction FRS at four quadrants

As expected spectral accelerations at the two governing mode frequencies still showed a substantial range of variation. For X direction (Figure 4-18), this was especially remarkable in Quadrant C and D as defined in Figure 4-17 (a). For Quadrant A and B, spectral accelerations at higher frequencies, between 5 Hz and 10 Hz, are distributed over thick width. In the case of Y-direction (Figure 4-19), Quadrant B and D showed large variance as expected from Figure 4-15 (b).

In the case of the vertical response, each quadrant showed a comparatively wide range of variation. The FRS of Quadrant C and D are similar in shape whereas those of Quadrant A and B are somewhat different. Average FRS plotted in solid black lines, peak at different frequencies implying dynamic characteristics of the slab that differ from each quadrant. Peak amplitudes occurred around 10 Hz at Quadrant C and D, whereas those of Quadrant A and B appeared at a higher frequency range, 11 to 15 Hz. By separating into four quadrants, lumped FRS as in Figure 4-14 (c) were filtered, coarsely though, by major frequencies. Variation between the FRS, yet maintained.

Table 4-5 summarizes statistics - average, standard deviation, COV - of the spectral accelerations for discussed two cases. Firstly 1,551 nodal responses at the entire floor were analyzed. After calculating statistics at the 1<sup>st</sup> mode with respect to each direction, COVs were further computed for three different ranges of frequency: 1) frequency range from 1 Hz to 33 Hz (cut-off frequency); 2) low-frequency region between 1 Hz and 10 Hz where the governing natural frequencies of the auxiliary building are included; 3) high-frequency region

## **Chapter 4. Numerical Analysis of Nuclear Power Plant Structures**

---

beyond 10 Hz, up to 33 Hz where natural frequencies of secondary systems are (Kim, Choi, and Seo, 2012). Within each range, COV values were computed for each frequency than averaged.

COV values at four quadrants are inconsistent. For example, at Quadrant A COVs of X-direction reduce greatly, whereas those of Y-direction remain. It is opposite at Quadrant C and reductions in Z-direction are insignificant in all quadrants.

## Chapter 4 Numerical Analysis of Nuclear Power Plant Structures

Table 4-5 Statistics of spectral accelerations for two cases: total floor and four quadrants

	Total Floor			Four Quadrants												
	$\mu$ [g]	$\sigma$ [g]	COV	Quadrant A			Quadrant B			Quadrant C			Quadrant D			
	$\mu$ [g]	$\sigma$ [g]	COV	$\mu$ [g]	$\sigma$ [g]	COV	$\mu$ [g]	$\sigma$ [g]	COV	$\mu$ [g]	$\sigma$ [g]	COV	$\mu$ [g]	$\sigma$ [g]	COV	
X direction																
1 <sup>st</sup> Mode	5.59	1.63	0.29	4.43	0.95	0.21	4.96	0.65	0.13	6.27	1.60	0.26	6.62	1.75	0.26	
1 - 33 Hz	-	-	0.15	-	-	0.12	-	-	0.12	-	-	0.15	-	-	0.14	
1 - 10 Hz	-	-	0.15	-	-	0.12	-	-	0.11	-	-	0.14	-	-	0.13	
10 - 33 Hz	-	-	0.15	-	-	0.10	-	-	0.13	-	-	0.16	-	-	0.15	
Y direction																
1 <sup>st</sup> Mode	4.02	1.69	0.42	2.64	1.10	0.42	4.94	2.11	0.43	4.12	0.75	0.18	4.68	1.62	0.35	
1 - 33 Hz	-	-	0.24	-	-	0.18	-	-	0.24	-	-	0.17	-	-	0.21	
1 - 10 Hz	-	-	0.26	-	-	0.21	-	-	0.24	-	-	0.18	-	-	0.22	
10 - 33 Hz	-	-	0.22	-	-	0.13	-	-	0.25	-	-	0.15	-	-	0.19	
Z direction																
1 <sup>st</sup> Mode	2.16	1.00	0.46	1.17	0.37	0.31	1.95	0.54	0.28	2.54	0.80	0.31	3.01	0.94	0.31	
1 - 33 Hz	-	-	0.28	-	-	0.26	-	-	0.27	-	-	0.25	-	-	0.23	
1 - 10 Hz	-	-	0.26	-	-	0.24	-	-	0.27	-	-	0.22	-	-	0.21	
10 - 33 Hz	-	-	0.33	-	-	0.31	-	-	0.28	-	-	0.30	-	-	0.27	

## 4.6 Treatment of uncertainty

In this section, two uncertainty treatment methods were compared in terms of FRS and variability. The overall procedure is identical to that in Section 3.4. Input ground motions listed in Table 3-4 were anchored to PGA 0.6 g, two times of SSE PGA, and consequently response level 2 was applied for the model. NUREG/CR-0098 (Newmark and Hall, 1978) median spectrum compatible records, after site response analysis, are shown in Figure 4-21. 30 records and median response spectra of each direction were plotted together.

Four nodal points, indicated by 'X' symbols, in Figure 4-22 were investigated. Each node corresponds to equipment installed locations: Node 10137 (120 ft), Node 22526 (156 ft), Node 22546 (156 ft), Node 10135 (172 ft).

Procedures of two seismic response analyses were discussed in Section 3.4.3 and 3.4.4 in detail. Hence they were not repeated in this chapter, instead, results were compared directly. Several differences to note are tri-directional ground motions were used simultaneously and a 5 percent damping ratio was assumed for equipment. According to ASCE/SEI 4-16 (2017) each component of the ground motions may be separately analyzed and the three resultant responses could be later combined via SRSS or 100-40-40 rule. Alternatively the three components may be used simultaneously under a condition where correlation coefficients between three components are not greater than 0.16. The records listed in Table 3-4 satisfy this condition, hence the latter procedure was used.

Figure 4-23, Figure 4-24 show median FRS of H1, H2, V directions, from top to bottom, about four nodes previously designated. The results resembled

## Chapter 4 Numerical Analysis of Nuclear Power Plant Structures

---

Figure 3-14, where the disparity between the two methods was concentrated at the tuning frequency. Deterministic best estimate FRS (solid line) and deterministic seismic response analysis FRS (dash-dot line) were almost identical except at peaks the latter being smaller five percent at maximum. Probabilistic seismic response analysis FRS (broken line) successfully reduced amplitudes near-resonant frequency, by averaging thirty samples with varying peaks. Generally, the probabilistic FRS were lesser than the deterministic FRS, and this trend diminished at the lower elevations in the structure. For example, peak differences at Node 10135 located at 172 ft were 30.7, 25.7, 39.2 %, whereas those at Node 10137 located at 120 ft were 23.0, 21.6, 24.6 %. This result coincides EPRI technical report (Ostadan, 2017).

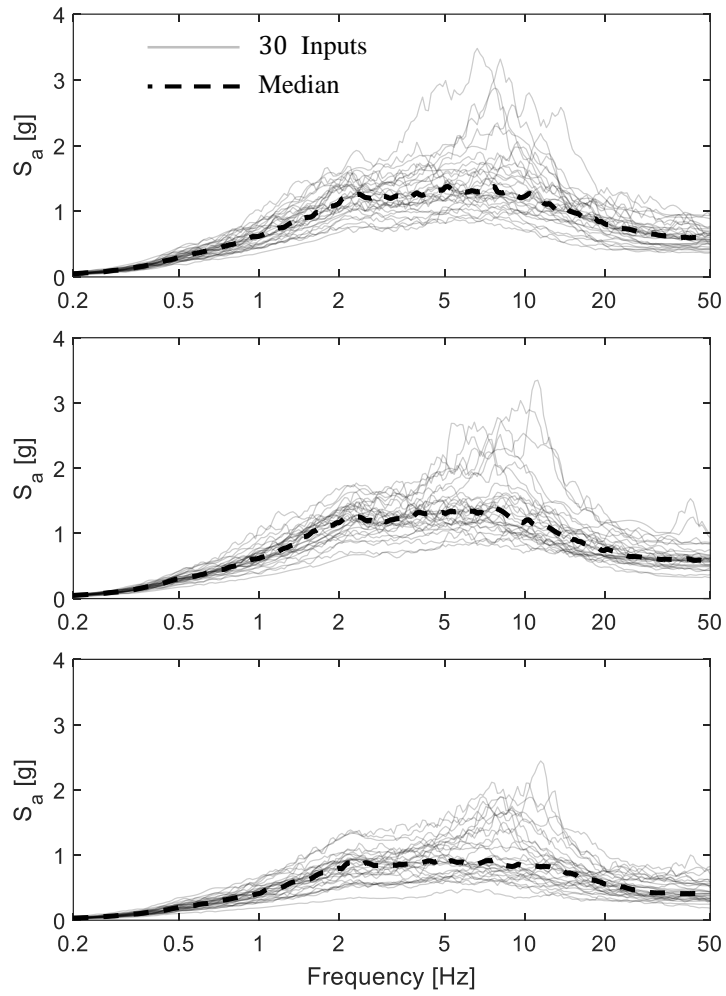


Figure 4-21 Input response spectra: (a) Horizontal 1; (b) Horizontal 2; (c) Vertical

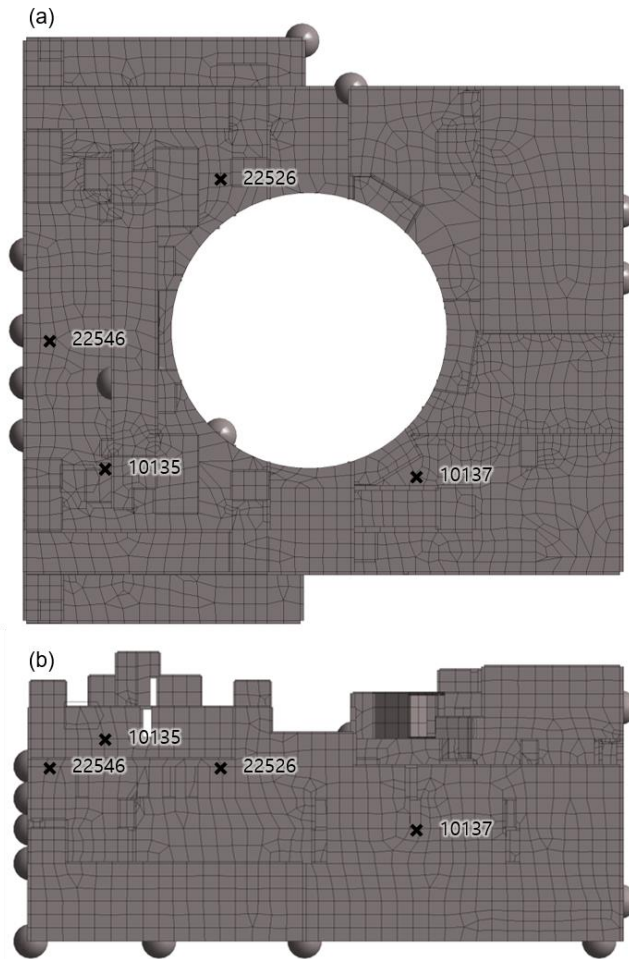


Figure 4-22 Node locations and IDs: (a) plan; (b) elevation

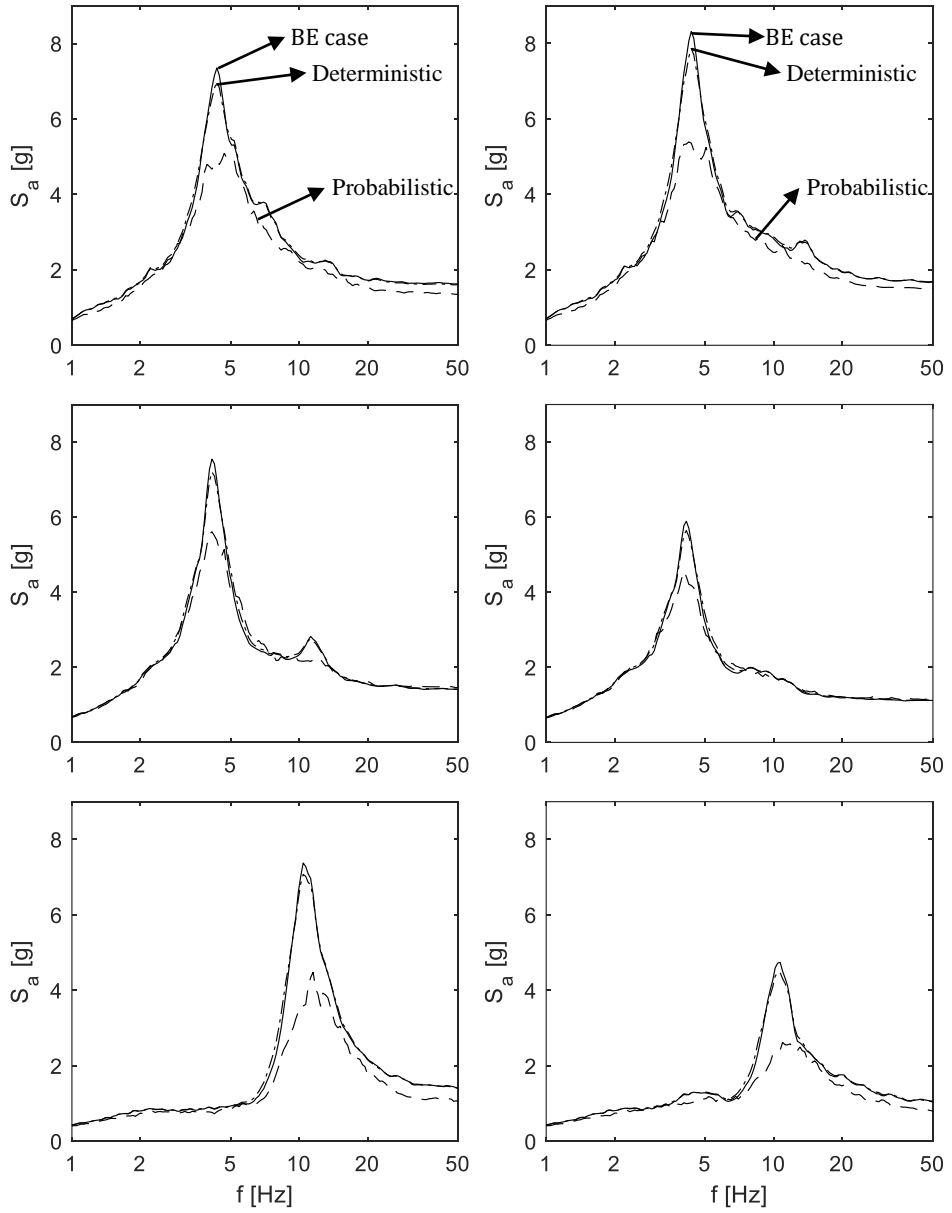


Figure 4-23 Median FRS of Node 10135(left), Node 22546(right)

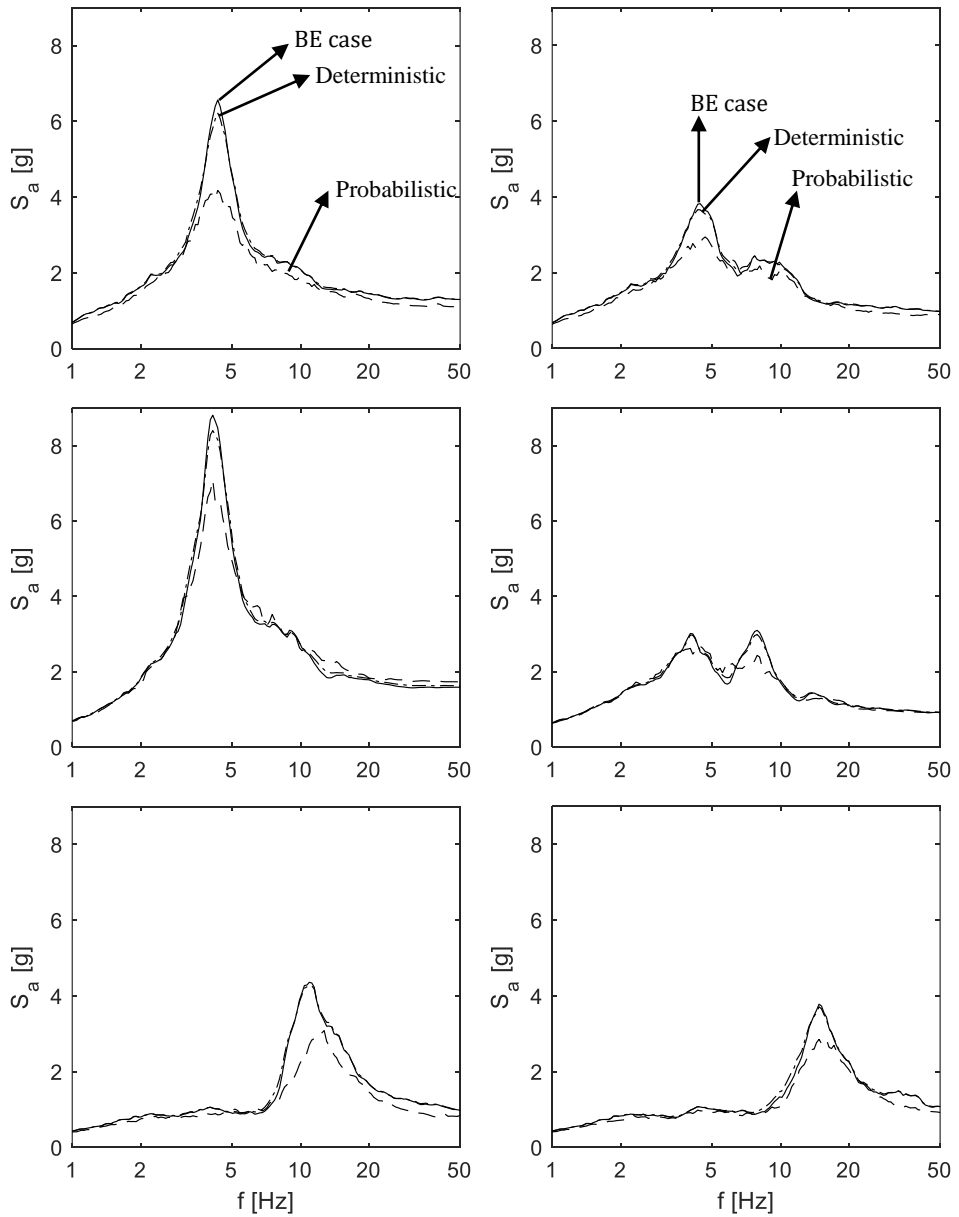


Figure 4-24 Median FRS of Node 22526(left), Node 10137(right)

## Chapter 4. Numerical Analysis of Nuclear Power Plant Structures

---

Deterministic seismic response analysis estimated median FRS close to that of probabilistic seismic response analysis, however, spectral acceleration near tuning frequency range was conservatively computed. As discussed in Section 3.4.5, this arises from the averaging process where the influence of structure frequency diminishes.

Other than its precision, deterministic seismic response analysis was long favored for its simple procedure. In form of sensitivity analysis, uncertainty and randomness of variables are accounted for. This accords with conventional structural analysis practice, as its name suggests. However, computational cost and convenience are not necessarily guaranteed. For each variable three cases, LB, BE, UB, are required and for each case, at least 5 time history analyses should be performed. Three variables give seven combinations as shown in Table 3-5, and eventually, a total of 35 time history analyses were conducted. It is important to note that more analyses are needed if more variables are incorporated. For every additional variable, two more cases composed of LB and UB of the new variable and BE of other variables will be added, in turn, ten more time history analyses.

Probabilistic seismic response analysis, contrarily, required a lesser number of analyses. As it is recently introduced and utilizes unfamiliar LHS, this method may seem cumbersome at a glance. Yet LHS, as reviewed in Section 2.4, is simply a sampling technique and once samples of each variable are prepared, repetitive analyses follow. Moreover, estimating median FRS and variability is straightforward. Median FRS is directly calculated by finding median values from thirty FRSs, whereas it is estimated through multiple steps of averaging in the scheme of deterministic seismic response analysis.

### 4.7 Summary

In this chapter, 3-D finite element analysis of the auxiliary building, part of NPP structures, was performed to examine the influences of the four factors on FRS.

- 1) **Dynamic coupling effect:** ESI was accounted for by frequency domain analysis. Three nodes were investigated to show a consistent decrease in the resonant response with an increase of the mass ratio. However, due to massive modal masses, the dynamic coupling effect could be useful for only the limited number of equipment.
- 2) **Influence of strong-motion duration:** A total of 132 ground motions with different  $D_{5-75}$ , along with the model corresponding to response level 1 were used in this section. Results were extracted from eleven nodes to show the positive correlation between  $D_{5-75}$  and amplification in nonlinear expression. A similar trend was also observed when the ratios of the two parameters were plotted. In general, regression lines predicted a 10 to 20 percent reduction for  $D_{5-75}$  of a ground motion that is one-fifth to another.
- 3) **Spatial variation:** From 1,559 nodes at EL. 137.5 ft floor under a single case of ground motion, tri-directional FRS were generated and compared. Due to the large opening at the center of the auxiliary building, spectral accelerations of two horizontal directions showed significant spatial variation at the first mode frequencies. In the case of the vertical direction, the disparity was observed over a wide range

of frequencies, which was maintained when the floor was quarterly segmented.

- 4) **Treatment of uncertainty:** Two methods deterministic and probabilistic seismic response analysis were compared in terms of median FRS. Spectral shapes of FRS of two methods and that of best estimate were alike, except in the vicinity of tuning frequency, where the significant reduction was observed for probabilistic seismic response analysis.

## **Chapter 5. Seismic Fragility Analysis of Equipment**

### **5.1 Introduction**

In this chapter, seismic fragility analysis of equipment was performed as a case study. As introduced in Chapter 1, FRS is used to analyze secondary systems installed in NPP structures. With the generated FRS, seismic response analysis of equipment must follow, and together with seismic capacity analysis, seismic fragility analysis completes. The purpose of this chapter is to show the aforementioned process with a simple example.

Another objective is to demonstrate how four factors propagate into the fragility curve. In Chapter 3 and Chapter 4, conditional reduction in seismic demand by considering four factors was observed, yet its importance was rather unclear. Therefore change in FRS amplitudes and variabilities, eventually, fragility curve was emphasized in this chapter.

The background of seismic fragility analysis is briefly discussed in the next section. Then equipment seismic response analysis with previously obtained FRS is presented. For equipment seismic capacity analysis, another integral part of seismic fragility analysis is beyond the scope of this thesis, assumptions were made regarding the seismic capacity. Lastly, equipment seismic fragility curves were generated with the seismic demand and capacity.

## **5.2 Seismic fragility analysis**

### *Concept of fragility*

In this section, the background of seismic fragility analysis is briefly introduced. Fragility by definition is a conditional probability of failure. The purpose of the fragility curve is to express the seismic capacity of SSCs in terms of the probability distribution. This is because by nature uncertainties are inherent in variables, including ground motion, structure, equation, analysis method, and others.

In the field of nuclear engineering, a so-called safety-factor method proposed by Kennedy et al. (1980) is well adopted. Among several fragility analysis methods, this is favored for its simplicity. Only three parameters, namely median capacity, variabilities of uncertainty, and randomness, are required to generate the fragility curve. Two variabilities separately account for epistemic uncertainty due to lack of knowledge and aleatory uncertainty, randomness inherent in the median value.

For the fragility curve, the lognormal distribution is used for several advantages: mathematically manageable; easily converted to a composite fragility curve (Kennedy, 1980). The fragility curve can be expressed as below,

$$P'_F = \Phi \left[ \frac{\ln \left( \frac{a}{A_m} \right) + \beta_U \Phi^{-1}(Q)}{\beta_R} \right] \quad (5.1)$$

## Chapter 5 Seismic Fragility Analysis of Equipment

---

where  $a$  is the ground parameter,  $A_m$  is the median capacity,  $\beta_R$  and  $\beta_U$  are the variabilities of randomness and uncertainty,  $\Phi^{-1}$  is the inverse cumulative normal distribution function,  $Q$  is the confidence defined as  $Q = P[P_F < P'_F | a]$ .

Exemplary fragility curves are shown in Figure 5-1. In ordinate the ground parameter is defined in terms of PGA, and abscissa corresponds to the fragility or conditional probability of failure. As shown above, fragility curves are plotted as a cumulative distribution function. The frequency of failure increases for the greater PGA, as expected.

Overall magnitude, whether the curves are located on the left or right, is largely governed by the epistemic uncertainty for the given median capacity. Compared to the median fragility curve, the 95 % confidence curve estimates lesser PGA for a given probability of failure. The slope of the curves is determined by the aleatory uncertainty. Higher the randomness, the more gradual the slope implying greater variance about the median capacity. Depending on the variabilities, two curves with the same median capacity could differ in capacities of other levels of fragility. This is important because the capacity of SSC is often conveyed in terms of High-Confidence of Low-Probability of Failure (HCLPF) capacity. The HCLPF capacity, as its name suggests, is defined as a 5 % probability failure at a 95 % confidence level. The corresponding expression can be written as,

$$\text{HCLPF} = A_m * e^{[-1.65 * (\beta_R + \beta_U)]} \quad (5.2)$$

$$\text{HCLPF} \cong A_{1\%} = A_m * e^{[-2.33 * \beta_C]} \quad (5.3)$$

Alternatively, the HCLPF capacity can be approximated as (5.3) where 1 % NEP capacity is calculated with the composite logarithmic standard deviation,  $\beta_C$ . Owing to characteristic of the lognormal distribution, the composite logarithmic standard deviation can be expressed as,

$$\beta_C = \sqrt{\beta_R^2 + \beta_U^2} \quad (5.4)$$

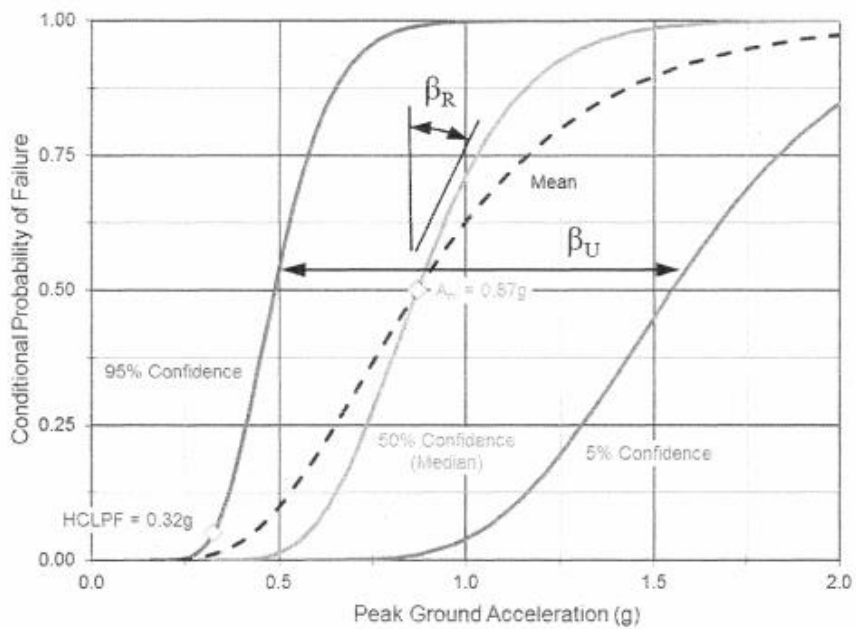


Figure 5-1 Fragility curves example (EPRI, 2018)

Approximate second-moment procedure for calculation

EPRI guidance (Grant, Hardy, and Short, 2018) presents several methods to

## Chapter 5 Seismic Fragility Analysis of Equipment

---

calculate three parameters defining the fragility curves. The approximate second-moment procedure is the easiest of all while producing reasonable results, hence recommended. In the approximate second moment procedure, three parameters are expressed as,

$$A_m = SF_m * PGA_{RE} \quad (5.5)$$

$$\beta = \left[ \sum_i \beta_i^2 \right]^{\frac{1}{2}} \quad (5.6)$$

where  $SF_m$ ,  $PGA_{RE}$  are the median safety factor and PGA of the reference earthquake.  $\beta_i$  stands for the final logarithmic standard deviation as a result of the variability in the i-th variable. The individual  $\beta_i$  values are calculated as,

$$\beta_i = -\frac{1}{Z} * \ln \left[ \frac{SF_{Z\sigma_i}}{SF_m} \right] \quad (5.7)$$

$SF_{Z\sigma_i}$  is the scale factor defined at Z standard deviation from the median of the i-th variable.

In the context of the fragility analysis, the variables refer to factors that may have caused conservatism or unconservatism in design, due to the inherent variabilities. The variables include material properties, static strength equations, input ground motions, seismic response properties, and others.

From the following sections, the aforementioned procedure is illustrated with the load centers. More details, that are not mentioned in this section, necessary for developing the fragility curve are also covered.

### 5.3 Equipment seismic response analysis

#### *Locations of selected nodes*

Six 480 V load centers, typical electrical equipment installed in EL. 137.5 ft floor, were selected for the analysis. The primary reason for the selection is that their support locations are varied on the same floor, which is an ideal condition to account for spatial variation. The equipment locations are shown in Figure 5-2. At each location marked as symbol 'X', the identification name was designated according to its location and configuration, i.e. QA-V stands for the support located at Quadrant A where the long side of the equipment is installed parallel to the north-south direction. Node ID numbers are additionally written in parentheses.

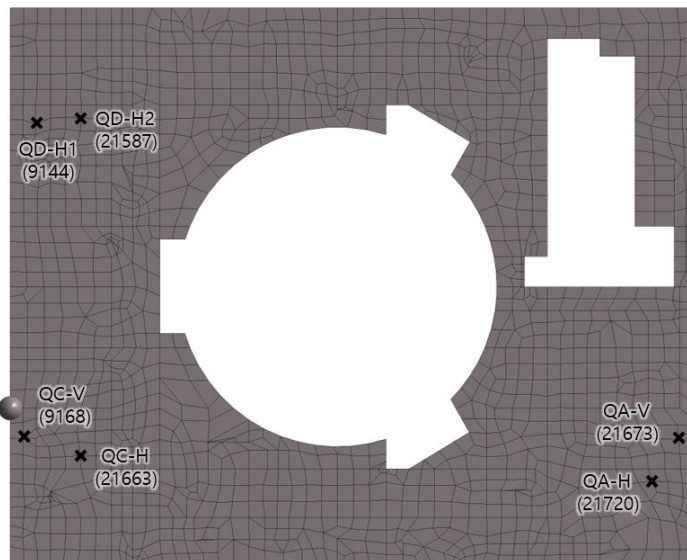


Figure 5-2 Node locations and IDs

### *Failure mode*

Once the target equipment was determined, the seismic response could be computed as simply finding spectral accelerations for fundamental frequencies of the equipment. Equipment frequencies are obtainable through analysis or test. Appendix of EPRI (Grant, Hardy, and Short, 2018) shows a detailed procedure of calculating three different modal frequencies from the physical properties of a heat exchanger. In the case of the test, a shake-table or impact hammer test could be applied. In the thesis, the first mode frequency of 480V load center, installed in operating NPP, presented in a report by KEPCO (1992; as cited by Kim et al., 2011) was adopted. As only one frequency was available it was assigned to the translational mode about a weak axis, and other modes were neglected.

For specific analysis, failure mode should be designated but for several reasons, functional failure evaluated as spectral acceleration exceedance of a certain threshold value is used. One reason is that detailed geometry configurations are missing. Due to the fact that information related to NPP is highly confidential, drawings of equipment were hardly attainable. Another reason is that governing failure mode of electrical equipment is in fact the functional failure. Kim et al. (2012) cited the KEPCO report (1992) where fragility results of electric equipment including 480 V load center were summarized. For all the equipment, median capacities of functional failure were lesser than those of structural failure. Lastly, the function failure was selected for simplicity. Examples of previous documents and technical reports could be borrowed, and structural failure modes then may be analyzed. However as the

thesis is focused on the seismic demand, deviating procedure was replaced by the concise case.

### *Seismic demands experienced by the equipment*

Seismic demands at the six support locations were acquired by probabilistic seismic response analysis. The process described in Section 4.6 was repeated for six nodes, then thirty FRS per node were prepared. The median damping ratio of five percent was used as EPRI guidance (Grant, Hardy, and Short, 2018) suggests the value for electrical cabinets.

In this section, the equipment frequency factor is further accounted for. As summarized in Table 5-1, all the other variables are included in the FRS as illustrated in the previous chapters. Seismic demands exerted on the equipment can be obtained by locating spectral accelerations corresponding to the natural frequency of the equipment on the FRS. Nonetheless, due to the variability in the equipment frequency, variance in the seismic demands is expected.

## Chapter 5 Seismic Fragility Analysis of Equipment

Table 5-1 Summary of the variables considered in the thesis

Variable Symbol	Variable Meaning	F	$\beta_R$	$\beta_U$
<b>Structure</b>				
$F_{HDPR}$	Horizontal direction peak response factor	1.0	0.18	-
$F_V$	Vertical direction peak response factor	1.0	0.25	-
$F_{\delta_s}$	Structure damping ratio factor	1.0	-	0.33
$F_{f_s}$	Structure frequency factor	1.0	-	0.28
<b>Equipment</b>				
$F_s$	Strength factor	1.0	-	
$F_{\delta_e}$	Equipment damping ratio factor	1.0	-	0.29
$F_{f_e}$	Equipment frequency factor	1.0	-	0.10

The equipment frequency factor is included along with the framework of LHS-based response analysis. With the logarithmic standard deviation suggested in EPRI guidance (Grant, Hardy, and Short, 2018), thirty frequencies were sampled to obtain the spectral acceleration distribution.

Figure 5-3 shows the X and Y direction spectral acceleration distributions. Vertical inputs were disregarded for the scope of this section is solely the first translational mode. Black bars represent the histogram of the X-direction

accelerations and white bars display that of the Y direction. Similarly, solid lines and broken lines each correspond to probability density functions of lognormal distributions fitted to the histograms. Two statistics, median and logarithmic standard deviation, were derived from the fitted distributions. One notable observation is that two nodes located at Quadrant A exhibit different trends. The variabilities of the spectral accelerations were smaller, especially for the Y-direction.

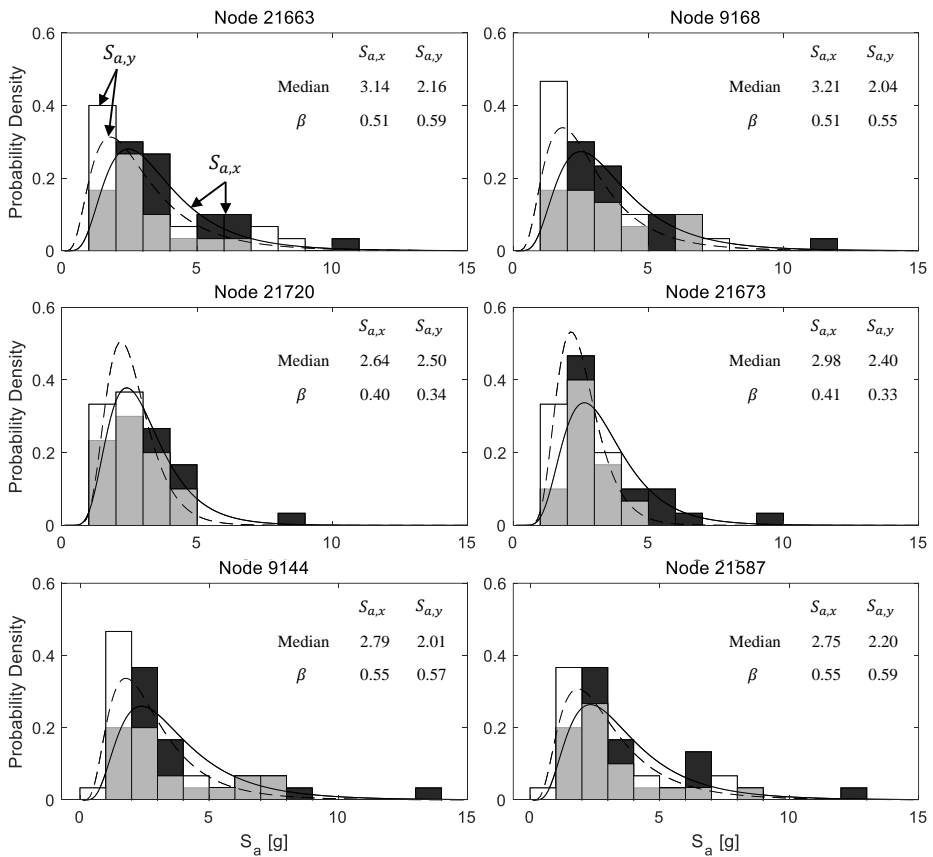


Figure 5-3 Horizontal  $S_a$  distributions

## Chapter 5 Seismic Fragility Analysis of Equipment

---

Differences between the two directions are meaningful as the load centers are rectangular in plan and individually placed. Two load centers, at Node 9168 and 21673 respectively, are installed parallel to the shorter side of the AB or the Y-axis. Meanwhile, four other load centers are arranged along the longitudinal side of the building. Consequently, for the two former  $S_{a,x}$  were applied, whereas  $S_{a,y}$  were used for the rest.

## 5.4 Equipment seismic fragility curve

### *Equipment seismic capacity*

Likewise, seismic capacity was defined in terms of spectral acceleration and it was assumed to be identical for all six equipment. A specific value of the capacity, 5 g, was arbitrarily determined, yet it is insignificant in the overall process. The main interest of this analysis is to investigate the influence of seismic demand on the fragility curve.

Having determined both seismic demand and seismic capacity, the strength factor can be estimated with the following equation,

$$F_S = \frac{C - D_{NS}}{D_S + \Delta C_S} \quad (5.8)$$

where  $C$  is the elastic capacity,  $D_S$  is the elastic demand,  $D_{NS}$  is the non-seismic demand, and  $\Delta C_S$  is the capacity reduction due to the concurrent seismic loading. The last two terms are neglected in this case, hence Equation (5.8) simply reduces to,

$$F_S = \frac{C}{D_S} \quad (5.9)$$

### *Safety factor estimation*

## Chapter 5 Seismic Fragility Analysis of Equipment

---

The final safety factor can be calculated as,

$$SF_m = F_c * F_{ER} * F_{RS} \quad (5.10)$$

where  $F_c$  is the capacity factor composed of the elastic strength factor and inelastic energy absorption factor, which is neglected.  $F_{ER}$  and  $F_{RS}$  are the equipment response factor and structure response factor, the products of the  $F$  values in Table 5-1. Other factors being unity, the safety factor is same as the strength factor.

The safety factor is obtained as the distribution. The variability of the safety factor can be directly estimated from it. Conventionally the total variability may be calculated by the SRSS (Equation (5.6)) of each variable. In the scheme of LHS though, variabilities of every variable are jointly treated and reflected in the final term. Since the strength factor is calculated as the nonvariant seismic capacity over the seismic demand, the variability of the seismic demand is maintained. These values of the composite logarithmic standard deviation, ranging from 0.34 to 0.59, may seem excessively large at a glance. Nonetheless, they are comparable to values reported by several authors (Kennedy et al., 1980; Kennedy et al., 1984; Park et al., 1998).

Kennedy et al. (1980) developed a generic response factor and suggested 0.47 and 0.45 for the logarithmic standard deviations of randomness and uncertainty, when equipment is designed based on dynamic analysis, mounted on low elevation, and has a low natural frequency. Accordingly, the composite logarithmic standard deviation is 0.65 by the SRSS. Kennedy et al. (1984) updated estimation of safety factor and logarithmic standard deviations,

suitable for modern plant designs. Refined values of the randomness and uncertainty variabilities are 0.29–0.44 and 0.34–0.52. Park et al. (1998) collected 450 fragility data for NPPs and summarized variabilities of 35 categories of SSC. Among various equipment, electric cabinets showed the third-largest composite logarithmic standard deviation, 0.66, composed of the random and uncertainty variabilities ranging 0.31–0.43, 0.27–0.82.

### Fragility curve

The median capacity may be calculated with Equation (5.5), multiplication of the safety factor, and the PGA of the reference earthquake which is 0.6 g (refer to Section 4.6). Essential parameters are prepared, the fragility curve can be developed with modified expression of Equation (5.1),

$$P'_F = \Phi \left[ \frac{\ln \left( \frac{a}{A_m} \right)}{\beta_c} \right] \quad (5.11)$$

In lieu of two separated variabilities, the composite logarithmic standard deviation is solely used. This is the mean fragility curve, the average of fragility curve family with a varying confidence level. The fragility curves of the load centers are shown in Figure 5-4.

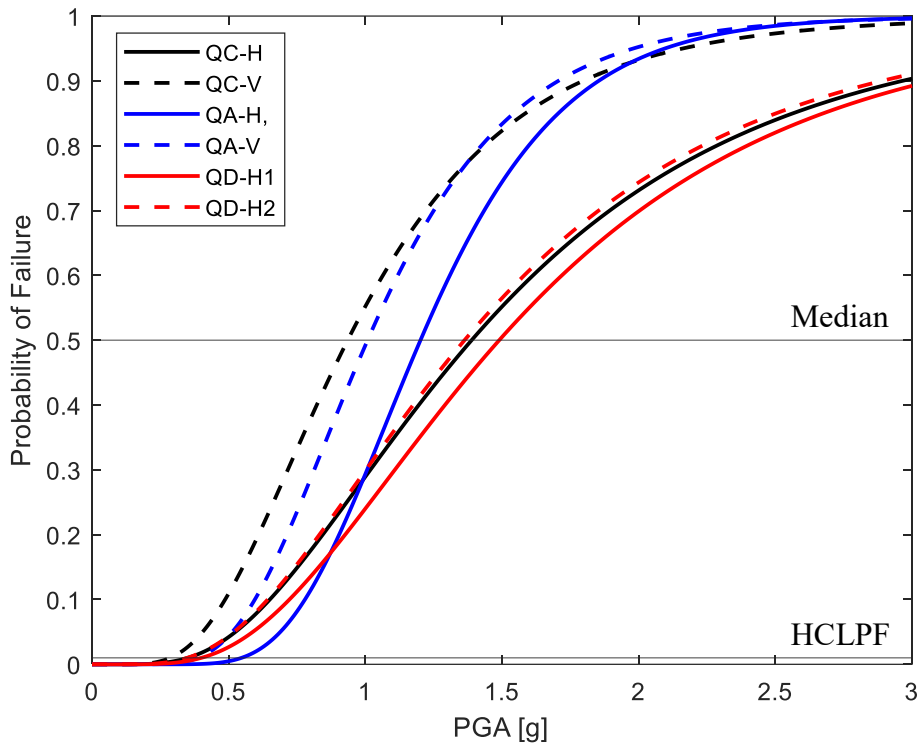


Figure 5-4 Mean fragility curves

Along with the six fragility curves, two horizontal lines are plotted to indicate the median and the HCLPF capacities, corresponding to 50 and 1 percent probability of failure. The capacities and the logarithmic standard deviation are tabulated in Table 5-2 Summary of capacities and variability.

Several observations were made from the fragility curves. One is the difference within the median capacities. They were sorted in the opposite order of magnitude of the seismic demands, as two parameters are inversely proportionate and the seismic capacity is a constant value. In other words, the seismic demands at the given location play a crucial role in defining the fragility curves of the equipment. This is noticeable when individual equipment is

compared to each other. QD-H1 and QD-H2 showed the smallest disparity within the three pairs. In terms of the median capacity, they differed by 8.7 %, whereas those at Quadrant A and C were 18.8 % and 47.9 %. It can be inferred from this examination that for the same response direction, similar capacity is expected for the same equipment. This is in line with what was mentioned in section 4.5 represented by Figure 4-15. On the other hand, significant variation may occur between orthogonal responses of closely spaced equipment. The difference was less distinctive for the distant equipment. QA-V and QC-V, QA-H and QC-H, QC-H, and QD-H2 pairs were compared to show 7.4 %, 15.8 %, 2.2 % differences, as they are axisymmetrically located (Figure 5-2). This is because all six cabinets were located away from intersections of each quadrant where the seismic responses are greater.

The logarithmic standard deviations showed a somewhat contrasting tendency. Quadrant C and D were similar and those of Quadrant A were substantially lesser. This is evident in the slope of the fragility curves. For instance, QA-H where the logarithmic standard deviation is the smallest is represented as the blue solid line that has the steepest slope. This is important in terms of the HCLPF capacity, as it depends not only on the median capacity but also on the variability. Even though the median capacity of QA-H is the fourth-largest, its HCLPF capacity is the greatest owing to the lowest variability. The influence of the slope is prominent when QA-V and QC-V, QA-H, and QC-H are compared. 34.4 % difference occurred between the first pair. In the case of the latter case, more interestingly, QA-H, one with the lesser median capacity, resulted in 57.1 % greater HCLPF capacity.

## Chapter 5 Seismic Fragility Analysis of Equipment

---

Table 5-2 Summary of capacities and variability

Location	Node ID	$A_m$ [g]	HCLPF [g]	$\beta_c$
QC-H	21663	1.39	0.35	0.59
QC-V	9168	0.94	0.29	0.51
QA-H	21720	1.20	0.55	0.34
QA-V	21673	1.01	0.39	0.41
QD-H1	9144	1.49	0.40	0.56
QD-H2	21587	1.36	0.35	0.59

### 5.5 Summary

In Chapter 5, seismic fragility analysis was conducted, as an application, for electric equipment. Propagation of the seismic demand discussed in Chapter 3, Chapter 4, into the seismic fragility was investigated, mainly for the spatial variation. Besides the secondary objective, which was to illustrate the overall process of the equipment seismic fragility analysis, the main findings may be summarized as below,

- 1) The spatial variation is a crucial factor for developing the fragility curve. Three parameters, though two in this section, defining the fragility curve show significant variation depending on the location within the same floor. The median capacities expectedly differ due to the different seismic demands. Moreover, the HCLPF capacities are not proportionate to the median capacities for the location-dependent variance of the logarithmic standard deviation.
- 2) The above finding implies that even for the same equipment, the seismic demand should be obtained individually for each location. It was shown that depending on the location as much as 57 % difference is possible. Hence, a location-specific FRS is recommended for developing a more realistic fragility curve.

### Chapter 6. Conclusions

In this thesis, four factors influencing seismic demand of secondary system were investigated in the first half, and the second half presented seismic fragility analysis of the electric equipment as an application. Major findings from this case study may be summarized as,

- 1) The results from Chapter 3 were consistently reproduced in Chapter 4 where the FEA was conducted. The influences of each factor were most prominent in the resonant frequency range.
- 2) Dynamic coupling effect or ESI, as studied by many researchers, showed as much as a 15 % reduction in the peak spectral acceleration at the mass ratio of 1.0 %. Despite the guaranteed decrease, this may be unobtainable in the actual practice as such a high mass ratio is scarce in NPP structures.
- 3) A positive correlation between strong-motion duration defined as  $D_{5-75}$  and the resonant amplification was observed. Based on 132 ground motion records, non-linear regression lines were fitted. Compared to the minimum strong-motion duration of 6 s required for the design input motion, on average 15 % decrease is expected for the Gyeongju earthquake, representative of the Korean Peninsula geoenvironment.
- 4) Two methods for the treatment of uncertainty as per EPRI guidance (Grant, Hardy, and Short, 2018) were compared. More rigorous probabilistic seismic response analysis yielded a maximum of 39 % lesser spectral acceleration than that of deterministic seismic response

analysis.

- 5) The principal contribution of this thesis is the consideration of the spatial variation in full scale of the NPP building. Entire seismic responses from one of the major floors were investigated to show significant variance within the floor, for the presence of a large opening at the center. Collective reduction for FRS at every location is impossible though, the necessity to generate equipment location-specific FRS was raised.
- 6) The aforementioned observation continued in the seismic fragility analysis, where six co-planar electric devices were analyzed. LHS-based probabilistic seismic response analysis was performed to show a location-dependent disparity in terms of the variability. The median and HCLPF capacities varied up to 48 and 57 % for the very same equipment supported at different locations. Therefore, considering the location of the equipment may lead to more realistic fragility.

## References

ACI 318-19, 2019, "Building Code Requirements for Structural Concrete", American Concrete Institute.

Ansys® Mechanical, 2020, Release 20.2, ANSYS, Inc.

ASCE/SEI 4-16, 2017, "Seismic Analysis of Safety-Related Nuclear Structures", American Society of Civil Engineers.

ASCE/SEI 43-19, 2019, "Seismic Design Criteria for Structures, Systems, and Components in Nuclear Facilities", American Society of Civil Engineers.

Cappa, R., Appelbaum, A.C., Grant, F.F., 2019, "Case Study Investigating Probabilistic and Deterministic Sampling Methods for developing In-structure response spectra: Phase II", Transactions of SMiRT-25, Charlotte, NC, USA, Division V.

Cappa, R., Grant, F.F., Nakaki, D.K., 2017, "Case Study Investigating Probabilistic and Deterministic Sampling Methods for developing In-structure response spectra: Phase II", Transactions of SMiRT-24, Busan, Korea, Division V.

Center for Engineering Strong Motion Data,  
[www.strongmotioncenter.org](http://www.strongmotioncenter.org).

Chandramohan, R., Baker, J.W., Deierlein, G.G., 2016, "Quantifying the influence of ground motion duration on structural collapse capacity using spectrally equivalent records", Earthquake Spectra, 32(2), pp. 927-950.

Choi, D.-H., Lee, S.-H., 2005, "Generation of Floor Response Spectra including Equipment-Structure Interaction in Frequency Domain", *Journal of the Earthquake Engineering Society of Korea*, 9(6), pp. 13-19.

Choi, I.-K., 2017, "Review and Proposal for Seismic Safety Assessment of Nuclear Power Plants against Beyond Design Basis Earthquake", *Transactions of the Korean Society of Pressure Vessels and Piping*, 13(1), pp. 1-15.

Chopra, A.K., 2014, "Dynamics of Structures: Theory and Applications to Earthquake Engineering", Pearson, 4th Ed.

Damolini, S., El-Bahey, S., Oikonomou, K., 2019, "Seismic SSI Analysis Comparison Between Detailed and Discretized Modeling of an Auxilary / Control Building", *Transactions of SMiRT-25, Charlotte, NC, USA, Division III*.

Darendeli, M. B., 2001, "Development of a new family of normalized modulus reduction and matierla damping curves", Austin, Texas: The University of Texas.

Der Kiureghian, A., Sackman, J., Nour-Omid, B., 1983, "Dynamic Analysis of Light Equipment in Structures: Response to Stochastic Input", *Journal of Engineering Mechanics*, 109(1), pp.90-110.

Drake, R.M., Bachman, R.E., 1996, "NEHRP Provisions for 1994 for Nonstructural Components", *Journal of Architectural Engineering*, 2(1), pp. 26-31.

## References

---

Eggers, D.W., Bolourchi, S., Ostadan, F., 2011, "Probabilistic and Deterministic Seismic Soil Structure Interaction Analyses for the Lotung Quarter-Scale Containment Model.", Structures Congress 2011, pp. 864-875.

Foschaar, J.C., Baker, J.W., Deierlein, G.G., 2012, "Preliminary Assessment of Ground Motion Duration Effects on Structural Collapse", 15th World Conference on Earthquake Engineering, Lisbon, Portugal.

Fujita, S., Nakamura, I., Furuya, O., Watanabe, T., Minagawa, K., Morishita, M., Kamada, T., Takahashi, Y., 2012, "Seismic damage of mechanical structures by the 2011 Great East Japan Earthquake", 15th World Conference on Earthquake Engineering, Lisbon, Portugal.

Grant, F., Hardy, G., Short, S., 2018, "Seismic Fragility and Seismic Margin Guidance for Seismic Probabilistic Risk Assessments", Electric Power Research Institute, EPRI - 3002012994.

Gupta, A., 1984, "Seismic Response of Multiply Connected MDOF Primary and MDOF Secondary Systems", Nuclear Engineering and Design, 81(3), pp. 385-394.

Gupta, A., Jaw, J.W., 1986a, "Seismic Response of Nonclassically Damped Systems", Nuclear Engineering and Design, 91(2), pp. 153-159.

Gupta, A., Jaw, J.W., 1986b, "Response Spectrum Method for Nonclassically Damped Systems", Nuclear Engineering and Design,

91(2), pp. 161-169.

Ha, J., Kim, M.R., and Kim, M.K., 2021, "Spatial Variation Characteristics of Seismic Motions through Analysis of Earthquake Records at Fukushima Nuclear Power Plant", *Journal of Earthquake Engineering Society of Korea*, 25(5), pp.223-232. (in Korean).

Hancock, J., Bommer, J., 2006, "A state-of-knowledge review of the influence of strong-motion duration on structural damage", *Earthquake Spectra*, 22(3), pp. 827-845.

Isbiliroglu, Y., Ozkan, M.K., Rathod, Y., Vaidya, N., Cinkilic, C., 2019, "Effects of Structural Rigidity Reduction Due to Concrete Cracking Under Seismic Loads For Nuclear Structures", *Transactions of SMiRT-25*, Charlotte, NC, USA.

Jiang, W., 2016, "Direct Method of Generating Floor Response Spectra", University of Waterloo, Ph.D Dissertation.

Jung, J.W., Ha, J.G., Hahm, D., Kim, M.K., 2021, "In-structure Response Evaluation of Shear Wall Structure via Shaking Table Tests", *Journal of Earthquake Engineering Society of Korea*, 25(3), pp. 129-135. (in Korean).

Kaneko, K., 2019, "Effect of Strong Ground Motion Duration on the Expected Peak Values of Floor Response Spectra in Elastic Buildings", *Japan Architectural Review*, 4(2), pp. 440-450.

Kennedy, R.P., Cornell, C.A., Campbell, R.D., Kaplan, S., Perla, H.F., 1980, "Probabilistic seismic safety study on an existing nuclear power plant", *Nuclear Engineering and Design*, 59(2), pp.

## References

---

315-338.

Kennedy, R.P., Ravindra, M.K., 1984, "Seismic fragilities for nuclear power plant risk studies", Nuclear Engineering and Design, 79, pp. 47-68.

Kim, M.K., Choi, I.-K., 2011, "A Shaking Table Test for a Re-evaluation of Seismic Fragility of Electrical Cabinet in NPP", Journal of the Computational Structural Engineering Institute of Korea, 24(3), pp. 295-305. (in Korean).

Kim, M.K., Choi, I.-K., Seo, J.-M., 2012, "A Shaking Table Test for an Evaluation of Seismic Behavior of 480V MCC", Nuclear Engineering and Design, 243, pp. 341-355.

Korea Electric Power Corporation & Nuclear Power Co., Ltd., 2013, "Finite Element Seismic Models for SSI Analyses of the NI Buildings of The APR1400 Standard Plant", ML13304A931.

Korea Electric Power Corporation & Nuclear Power Co., Ltd., 2013, "Finite Element Seismic Models for SSI Analyses of the NI Buildings of The APR1400 Standard Plant", ML13304A935.

Korea Electric Power Corporation & Nuclear Power Co., Ltd., 2012, "Pre-Application Review Meeting: Seismic Analysis of APR1400-E-S-EC-120002-NP", ML12167A331.

Korea Electric Power Corporation & Nuclear Power Co., Ltd., 2010, "Pre-Application Review Meeting", ML102530217.

Korea Electric Power Corporation & Nuclear Power Co., Ltd., 2020, "Status Report - APR1400 (KEPCO E&C/KHNP),

[aris.iaea.org/PDF/APR1400\\_2020May.pdf](https://aris.iaea.org/PDF/APR1400_2020May.pdf).

Kottke, A.R., Rathje, E.M., 2008, "Technical manual for Strata", Pacific Earthquake Engineering Research Center, University of California, Berkeley, Report No.:2008/10.

MATLAB, 2021, Version 2021b, The Math Works, Inc.

McGuire, R.K., Silva, W.J., Constantino, C.J., 2001, "Technical Basis for Revision of Regulatory Guidance on Design Ground Motions: Hazard-and Risk-consistent Ground Motion Spectra Guidelines", U.S. Nuclear Regulatory Commission, NUREG/CR-6728.

McNeel, R., others, 2010, Rhinoceros 3D, Version 6.0., Robert McNeel & Associates, Seattle, WA.

National Research Institute for Earthquake Science and Disaster Prevention, [www.kyoshin.bosai.go.jp](http://www.kyoshin.bosai.go.jp).

Newmark, N. M., Hall, W. J., 1978, "Development of Criteria for Seismic Review of Selected Nuclear Power Plants", U.S. Nuclear Regulatory Commission, NUREG/CR-0098.

NUREG-0800, 2014, Standard Review Plan, U.S. Nuclear Regulatory Commission.

Ostadan, F., 2017, "Advanced Nuclear Technology: High-Frequency Seismic Loading Evaluation for Standard Nuclear Power Plants", Electric Power Research Institute, EPRI - 3002009429.

Park, Y.J., Hofmayer, C.H., Chokshi, N.C., 1998, "Survey of

## References

---

Seismic Fragilities used in PRA Studies of Nuclear Power Plants”, *Reliability Engineering and System Safety*, 62(3), pp. 185-195.

PEER Ground Motion Database, [peer.berkeley.edu/peer-strong-ground-motion-databases](http://peer.berkeley.edu/peer-strong-ground-motion-databases).

Regulatory Guide 1.61, 2007, "Damping Values For Seismic Design of Nuclear Power Plants", U.S. Nuclear Regulatory Commission.

Sackman, J., Der Kiureghian, A., Nour-Omid, B., 1983, "Dynamic Analysis of Light Equipment in Structures: Modal Properties of the Combined System", *Journal of Engineering Mechanics*, 109(1), pp.73-89.

Suarez, L.E., Singh, M.P., 1987, "Floor Response Spectra with Structure-Equipment Interaction Effects by a Mode Synthesis Approach", *Earthquake Engineering and Structural Dynamics*, 15(2), pp. 141-158.

Takeru, I., Der Kiureghian, A., 1985a, "Dynamic Characterization of Two-Degree-of-Freedom Equipment-Structure Systems", *Journal of Engineering Mechanics*, 111(1), pp. 1-19.

Takeru, I., Der Kiureghian, A., 1985b, "Dynamic Response of Multiply Supported Secondary Systems", *Journal of Engineering Mechanics*, 111(1), pp. 20-41.

Takeru, I., Der Kiureghian, A., 1985c, "Generation of Floor Response Spectra Including Oscillator-Structure Interaction", *Earthquake Engineering and Structural Dynamics*, 13(5), pp. 661-

676.

Tokyo Electric Power Company, 2011, "Strong motion data - the 2011 Great East Japan Earthquake - Fukushima Daiichi & Daini (Nos. 1&2) Nuclear Power Plants", Japan Association for Earthquake Engineering.

Toro, G. R., 1995, "Probabilistic models of site velocity profiles for generic and site-specific ground-motion amplification studies", Upton, New York: Brookhaven National Laboratory.

Tseng, W.S., 1989, "Equipment Response Spectra Including Equipment-Structure Interaction Effects," Proceedings of the 1989 ASME Pressure Vessels and Piping Conference, Honolulu, Hawaii, July 23-27, 1989, ASME, PVP-Vol. 155, pp. 21-29.

Villaverde, R., 1997, "Seismic Design of Secondary Structures: State of the Art", Journal of Structural Engineering, 123(8), pp.1011-1019.

Villaverde, R., Newmark, N.M., 1980, "Seismic Response of Light Attachments to Buildings", UIUC, SRS-469.

Xu, J., DeGrassi, G., Chokshi, N., 2004, "A NRC-BNL Benchmark Evaluation of Seismic Analysis Methods For Non-classically Damped Coupled Systems", Nuclear Engineering and Design, 228, pp. 345-366.

Zinn, R., Borgerhoff, M., Bumann, U., Schneeberger, C., Szczesiak, T., 2015, "Probabilistic and Deterministic Seismic In-structure response spectra of reactor buildings KKB and KKG",

## References

---

Transactions of SMiRT-23, Manchester, United Kingdom, Division VII.

## Appendix A: Spectrally Equivalent Earthquake Triads

No.	Dur.	Eearthquake Name	Year	Station	Magnitude	PGA [g]	D <sub>5-75%</sub> [s]	Scale Factor
1	< 6 s	Chi-Chi_Taiwan-06	1999	CHY047	6.3	0.23	5.56	1.39
	6-20s	Kocaeli_Turkey	1999	Izmit	7.5	0.23	6.38	1.00
	>20s	Tohoku, Japan	2011	Tendou	9.0	0.19	63.95	1.05
2	<6s	Bolinas Earthquake	1999	San Rafael - 2nd & Lincoln	5.0	0.21	0.40	5.00
	6-20s	Duzce_Turkey	1999	IRIGM 496	7.1	1.03	10.33	1.00
	>20s	Maule, Chile	2010	Angol	8.8	0.92	23.02	1.18
3	<6s	Gyeongju	2016	DKJ	5.8	0.10	1.34	1.47
	6-20s	Tottori_Japan	2000	OKYH07	6.6	0.18	8.53	1.00
	>20s	Tohoku, Japan	2011	Fukushima	9.0	0.58	73.98	0.2
4	<6s	Coyote Lake Earthquake	1979	Gilroy #3 - Sewer Farm A	5.7	0.26	2.40	0.90
	6-20s	Iwate_Japan	2008	IWT010	6.9	0.29	7.81	1.00
	>20s	Tohoku, Japan	2011	Tendou	9.0	0.17	96.61	1.34
5	<6s	Northridge Earthquake	1994	Featherly Park - Maint. Bldg.	6.4	0.10	5.76	1.40
	6-20s	Ridgecrest Earthquake	2019	Death Valley - Shoshone	7.1	0.12	15.58	1.00
	>20s	Tohoku, Japan	2011	Aiduwakamatsu	9.0	0.42	56.63	0.20
6	<6s	Chino Hills Earthquake	2008	Hollywood - Franklin & Bronson [aband]	5.4	0.12	2.45	0.83
	6-20s	Calexico Earthquake	2010	La Quinta - Bermudas & Durango	7.2	0.10	6.65	1.00
	>20s	Tohoku, Japan	2011	Sakunami	9.0	0.49	66.66	0.2
7	<6s	Kocaeli_Turkey	1999	Gebze	7.5	0.26	5.83	0.80
	6-20s	Hector Mine Earthquake	1999	Amboy	7.1	0.18	12.56	1.00
	>20s	El Mayor-Cucapah	2010	Ejido Saltillo	7.2	0.15	33.22	1.01

## Appendix A: Spectrally Equivalent Earthquake Triads

8	<6s	ChalfantValley Earthquake	1986	Chalfant - Zack Ranch	5.9	0.27	2.98	0.85
	6-20s	Northridge Earthquake	1994	Point Mugu - Naval Air Station	6.4	0.18	7.72	1.00
	>20s	Tohoku, Japan	2011	Higashine	9.0	0.20	84.22	1.13
9	<6s	Loma Prieta Earthquake	1989	Gilroy #1 - Gavilan College Tank Grnds	7.0	0.44	1.44	0.20
	6-20s	Northridge Earthquake	1994	San Pedro - Palos Verdes Fire Station	6.4	0.10	6.84	1.00
	>20s	Tohoku, Japan	2011	Sakunami	9.0	0.41	64.06	0.20
10	<6s	La Habra Earthquake	2014	Brea - Central Av Caltrans Yard	5.1	0.70	0.62	0.20
	6-20s	Big Bear Earthquake	1992	Snow Creek	6.5	0.16	6.66	1.00
	>20s	Maule, Chile	2010	Curico	8.8	0.47	39.37	0.20
11	<6s	Petrolia Aftershock 1	1992	Fortuna - 701 S. Fortuna Blvd.	6.5	0.19	4.16	0.89
	6-20s	Landers Earthquake	1992	Big Bear Lake - Civic Center Grounds	7.3	0.19	17.73	1.00
	>20s	Tohoku, Japan	2011	Kohriyama	9.0	1.04	66.55	0.20
12	<6s	Petrolia Earthquake	1992	Petrolia [replaced]	7.1	0.66	2.88	0.20
	6-20s	Landers Earthquake	1992	Barstow - Vineyard & H St.	7.3	0.14	12.78	1.00
	>20s	Landers	1992	Thousand Palms Post O-ce	7.3	0.11	25.51	0.86
13	<6s	Brawley Area Earthquake	2012	Westmorland - Fire Station	5.5	0.16	2.27	0.99
	6-20s	Landers Earthquake	1992	Amboy	7.3	0.15	18.54	1.00
	>20s	Maule, Chile	2010	Santiago La Florida	8.8	0.18	23.80	1.05
14	<6s	Chino Hills Earthquake	2008	Chino Hills - Hwy 71 & Eucalyptus	5.4	0.12	1.87	0.95
	6-20s	Landers Earthquake	1992	Wrightwood - Swarthout Valley	7.3	0.11	16.69	1.00
	>20s	Maule, Chile	2010	Curico	8.8	0.41	38.20	0.20
15	<6s	Parkfield Earthquake	2004	Parkfield - Fault Zone 1	6.0	0.82	1.68	0.20
	6-20s	Petrolia Earthquake	1992	Fortuna - 701 S. Fortuna Blvd.	7.1	0.12	11.40	1.00
	>20s	Landers	1992	Thousand Palms Post O-ce	7.3	0.10	26.39	0.92
16	<6s	Chino Hills Earthquake	2008	Olinda - Carbon Canyon Rd [abandoned]	5.4	0.11	1.89	5.00
	6-20s	Calexico Earthquake	2010	El Centro - Imperial & Ross	7.2	0.38	14.88	1.00
	>20s	Maule, Chile	2010	Hualane	8.8	0.37	41.94	1.00
	<6s	Parkfield Earthquake	2004	Parkfield - Temblor	6.0	0.10	3.34	1.33

**Appendix A: Spectrally Equivalent Earthquake Triads**

17	6-20s	Calexico Earthquake	2010	Salton City	7.2	0.20	6.41	1.00
	>20s	Tohoku, Japan	2011	Kohriyama	9.0	0.77	67.51	0.20
18	<6s	South Napa Earthquake	2014	Pinole - Adobe & Pinole Valley Rd	6.0	0.20	3.36	1.17
	6-20s	Hector Mine Earthquake	1999	Big Bear Lake - Fire Station	7.1	0.17	7.95	1.00
	>20s	Kocaeli, Turkey	1999	Fatih	7.5	0.15	27.79	1.26
19	<6s	Morgan Hill Earthquake	1984	Corralitos - Eureka Canyon Road	6.2	0.11	3.5	1.10
	6-20s	Hector Mine Earthquake	1999	Fort Irwin [abandoned]	7.1	0.13	7.88	1.00
	>20s	Landers	1992	Indio - Coachella Canal	7.5	0.10	29.44	0.96
20	<6s	Coalinga Earthquake	1983	Coalinga - Slack Canyon	6.5	0.17	4.68	0.58
	6-20s	Hector Mine Earthquake	1999	Mecca - CVWD Yard	7.1	0.10	6.80	1.00
	>20s	Kocaeli, Turkey	1999	Bursa Tofas	7.3	0.10	20.51	1.11
21	<6s	Canyondam Earthquake	2013	Lake Almanor - Fire Staiaion	5.7	0.38	1.65	5.00
	6-20s	Northridge Earthquake	1994	Tarzana - Cedar Hill Nursery A [rplcd]	6.4	1.78	6.54	1.00
	>20s	Tohoku, Japan	2011	Kawamata	7.5	0.30	61.56	5.00
22	<6s	Tottori, Japan	2000	SMNH10	6.6	0.23	2.06	0.95
	6-20s	Northridge Earthquake	1994	Moorpark - Fire Station [demol]	6.4	0.29	7.70	1.00
	>20s	Tohoku, Japan	2011	Higashine	9.0	0.19	69.05	1.45
23	<6s	Petrolia Earthquake	1992	Cape Mendocino	7.1	1.50	2.66	0.20
	6-20s	Northridge Earthquake	1994	Los Angeles - Baldwin Hills	6.4	0.24	8.34	1.00
	>20s	Tohoku, Japan	2011	Fukushima	9.0	0.32	73.38	0.79
24	<6s	ChalfantValley Earthquake	1986	Chalfant - Zack Ranch	6.4	0.44	2.24	0.20
	6-20s	Northridge Earthquake	1994	San Bernardino - E & Hospitality	6.4	0.10	9.29	1.00
	>20s	Tohoku, Japan	2011	Miharu	9.0	0.50	72.01	0.20
25	<6s	Coalinga Earthquake	1983	Parkfield - Fault Zone 3	6.5	0.16	5.72	1.30
	6-20s	Landers Earthquake	1992	Yermo - Fire Station	7.3	0.24	7.82	1.00
	>20s	El Mayor-Cucapah	2010	Chihuahua	7.2	0.24	30.12	0.97
26	<6s	Petrolia Aftershock 1	1992	Petrolia [replaced]	6.5	0.60	2.94	0.20
	6-20s	Landers Earthquake	1992	Boron - Fire Station	7.3	0.12	7.74	1.00

## Appendix A: Spectrally Equivalent Earthquake Triads

	>20s	Tohoku, Japan	2011	Shiroishi	9.0	0.39	68.3	0.20
	<6s	La Habra Earthquake	2014	Diamond Bar - Grand & Diamond Bar Blvd	5.1	0.18	0.90	0.77
27	6-20s	Landers Earthquake	1992	Fort Irwin [abandoned]	7.3	0.12	7.86	1.00
	>20s	Maule, Chile	2010	Constitucion	8.8	0.53	92.43	0.20
	<6s	Parkfield Earthquake	2004	Parkfield - Vineyard Canyon 6W	6.0	0.11	4.80	0.68
28	6-20s	Landers Earthquake	1992	Baker - Fire Station	7.3	0.11	12.26	1.00
	>20s	Maule, Chile	2010	Talca	8.8	0.41	51.69	0.20
	<6s	Mt. Lewis Earthquake	1986	Halls Valley - Grant Park	5.8	0.15	0.98	0.96
29	6-20s	Petrolia Earthquake	1992	Eureka - 5th & H Federal Bldg [aband]	7.1	0.16	7.84	1.00
	>20s	Michoacan, Mexico	1985	Villita	8.1	0.13	32.43	1.27
	<6s	Parkfield Earthquake	2004	Parkfield - Fault Zone 15	6.0	0.23	3.20	1.33
30	6-20s	Superstition Hills Earthquake	1987	El Centro - Imperial Co. Center Grounds	6.6	0.34	7.06	1.00
	>20s	Tohoku, Japan	2011	Shiroishi	9.0	0.33	60.92	0.92
	<6s	Coalinga Earthquake	1983	Parkfield - Vineyard Canyon 1E	6.5	0.23	3.64	1.41
31	6-20s	Superstition Hills Earthquake	1987	Westmorland - Fire Station	6.6	0.21	10.00	1.00
	>20s	El Mayor-Cucapah	2010	Tamaulipas	7.2	0.20	24.60	1.07
	<6s	Coyote Lake Earthquake	1979	Gilroy #6 - San Ysidro Microwave Site	5.7	0.42	0.90	0.72
32	6-20s	Morgan Hill Earthquake	1984	Halls Valley - Grant Park	6.2	0.31	8.88	1.00
	>20s	Valparaiso, Chile	1985	Vina Del Mar	8.0	0.23	29.49	1.25
	<6s	Coalinga Earthquake	1983	Parkfield - Gold Hill 3W	6.5	0.14	2.82	0.57
33	6-20s	Imperial Valley Earthquake	1979	Niland - Fire Station	6.6	0.11	9.06	1.00
	>20s	Tohoku, Japan	2011	Aiduwakamatsu	9.0	0.43	69.41	0.20
	<6s	Coalinga Earthquake	1983	Parkfield - Fault Zone 16	6.5	0.18	5.98	0.49
34	6-20s	Chi-Chi_Taiwan-04	1999	CHY047	6.2	0.14	6.30	1.00
	>20s	Maule, Chile	2010	Santiago La Florida	8.8	0.13	27.58	0.63
	<6s	Chino Hills Earthquake	2008	Garden Grove - Chapman & Gilbert	5.4	0.18	0.49	1.06
35	6-20s	Niigata_Japan	2004	NIG014	6.6	0.12	16.14	1.00
	>20s	Tohoku, Japan	2011	Yamagata	9.0	0.14	84.83	0.81

**Appendix A: Spectrally Equivalent Earthquake Triads**

36	<6s	Mammoth Lakes Earthquake	1983	Mammoth Lakes - Convict Creek	5.2	0.16	2.90	1.59
	6-20s	Niigata_ Japan	2004	NIG025	6.6	0.20	7.03	1.00
	>20s	Hokkaido, Japan	2003	Hayakita	8.0	0.13	65.80	1.03
37	<6s	Loma Prieta Earthquake	1989	San Francisco - Presidio	7.0	0.20	3.08	0.64
	6-20s	Chuetsu-oki_ Japan	2007	NIG013	6.8	0.14	11.67	1.00
	>20s	Maule, Chile	2010	Constitucion	8.8	0.61	32.41	0.20
38	<6s	Whittier Earthquake	1989	Downey - County Maint. Bldg.	6.1	0.20	1.46	0.98
	6-20s	Chuetsu-oki_ Japan	2007	NIG025	6.8	0.23	7.26	1.00
	>20s	Hokkaido, Japan	2003	Hayakita	8.0	0.19	25.27	1.33
39	<6s	ChalfantValley Earthquake	1986	Bishop - South Street	6.4	0.25	3.70	0.76
	6-20s	El Mayor-Cucapah_ Mexico	2010	El Centro Array #3	7.2	0.18	15.43	1.00
	>20s	Tohoku, Japan	2011	Fukushima	9.0	0.20	76.66	0.97
40	<6s	Ferndale Area Earthquake	2010	Eureka - Myrtle & West Avenue	6.5	0.25	2.62	1.09
	6-20s	Kocaeli_ Turkey	1999	Ambarli	7.5	0.25	9.75	1.00
	>20s	Tohoku, Japan	2011	Takahata	9.0	0.20	61.67	1.07
41	<6s	Chino Hills Earthquake	2008	Riverside - Hole & La Sierra	5.4	0.19	1.33	1.34
	6-20s	Chi-Chi_ Taiwan-05	1999	CHY047	6.2	0.24	6.45	1.00
	>20s	Tohoku, Japan	2011	Miyakoji	9.0	0.90	65.27	0.20
42	<6s	Parkfield Earthquake	2004	Coalinga - Slack Canyon	6.0	0.35	2.26	0.20
	6-20s	Iwate_ Japan	2008	MYG017	6.9	0.10	9.65	1.00
	>20s	Tohoku, Japan	2011	Kakuda	9.0	0.35	72.67	0.20
43	<6s	Coalinga Earthquake	1983	Parkfield - Fault Zone 15	6.5	0.19	5.74	0.71
	6-20s	Chi-Chi_ Taiwan	1999	TAP005	7.6	0.13	10.81	1.00
	>20s	Tohoku, Japan	2011	Kaminoyama	9.0	0.12	97.55	1.04
44	<6s	Coalinga Earthquake	1983	Parkfield - Cholame 4W	6.5	0.13	5.44	0.85
	6-20s	Coalinga Earthquake	1983	Parkfield - Cholame 2W [Sta 2]	6.5	0.11	6.14	1.00
	>20s	Tohoku, Japan	2011	Miharu	7.5	0.56	75.73	0.20

## 초 록

# 원자력 발전소 내 부구조물 지진요구에 영향을 끼치는 요소: 사례연구

이 유 상

서울대학교 건축학과 대학원

2011년 후쿠시마 원자력 발전소 사고 이후 미 원자력규제위원회는 가동원전에 대한 전국적인 재평가를 요구하였다. 국내에서도 최근 경주와 포항에서 두 차례 관측 이래 최대 규모로 지진이 발생함에 따라 원전 지진안전성 평가에 대한 필요성이 주목받았다.

원전에서는 구조물뿐만 아니라 기기와 계통도 안전성 평가의 대상이 되는데, 그 중요성이 구조물 못지 않기 때문이다. 원전은 일반 건물과 달리 구조물에는 손상이 없더라도, 기기의 오작동 등으로 정상적인 운전이 문제를 초래할 수 있다. 이에 본 논문은 원전 내 부구조물인 기기의 지진요구를 분석하였다.

지진안전성 평가의 일환인 지진취약도 평가를 위해서는 정확한 지진 요구 계산이 필요하다. 현행에서 기기의 지진 요구는

층응답스펙트럼법으로 산정하는데, 이 과정에는 보수성 또는 비보수성이 포함되어있다. 따라서, 본 사례연구에서는 가동 원전 구조물의 유한요소해석을 통해 다음의 네 가지 요소들이 층응답스펙트럼에 미치는 영향을 살펴보았다: 1) 동적연계효과; 2) 강진지속시간; 3) 공간적 변동성; 4) 불확실성.

동적 연계 효과의 경우 많은 선행 연구에서 보고된 바와 같이, 구조물의 고유 진동수 부근에서, 부구조물의 질량이 클수록 그 응답이 작아지는 현상이 재현되었다. 강진지속시간은 공진 시에 부구조물 응답의 증폭과 상관관계가 있었고, 평가 시 사용하는 지반운동 대비 국내 지진환경에서는 부구조물 응답이 감소할 것으로 판단되었다. 한편, 동일 층내라도 위치에 따라 층응답스펙트럼의 편차는 크게 발생하였다. 특히 수직 응답의 경우 그 정도가 두드러졌는데, 이는 한 층을 사분면으로 구획하여도 유지되었다. 마지막으로 취약도 평가를 위해 불확실성과 무작위성을 고려하였을 때, 층응답스펙트럼은 특히 확률론적 지진응답해석으로 산정하였을 때 고유 진동수에서 스펙트럴 가속도가 저감되는 효과를 확인하였다.

산정한 층응답스펙트럼을 바탕으로 기기의 취약도 해석을 예시로서 수행하였다. 확률론적 지진 응답 해석을 사용하여 라틴하이퍼큐브 시뮬레이션 적용 절차를 소개하였다. 기기에 가해지는 지진 요구가 취약도 곡선 상에 나타나는 영향을 확인하고자, 특히 공간적 변동성 요소의 효과를 검토하였다. 해석

결과 위치에 따라 중앙 성능값 뿐만 아니라 변동성의 차이로 고신뢰도저확률과괴 성능값에도 유의미한 편차가 나타남을 확인하였다. 이에 따라 실질적인 중앙값 기준 성능을 평가하기 위해서는 기기 고유의 층응답스펙트럼 산정이 필요함을 시사하였다.

주요어 : 취약도 해석, 층응답스펙트럼, 유한요소해석, 원자력 발전소

학 번 : 2020-28248